

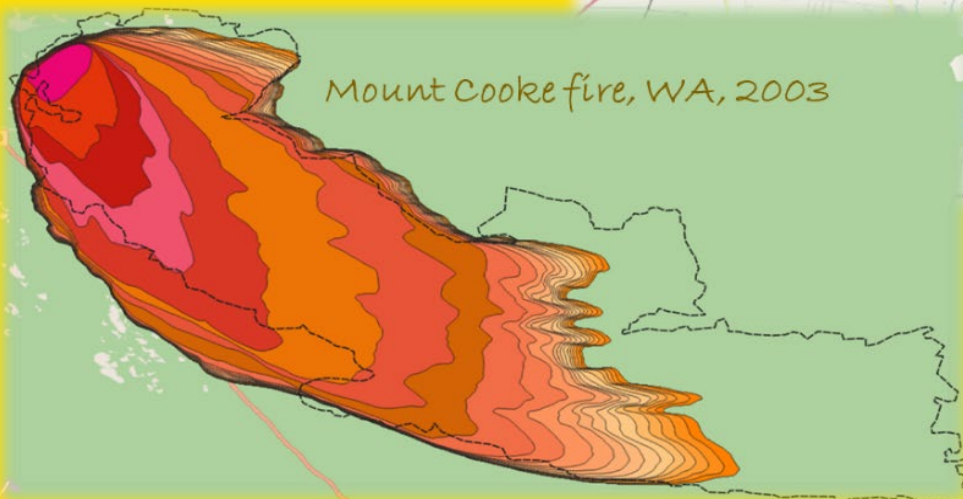
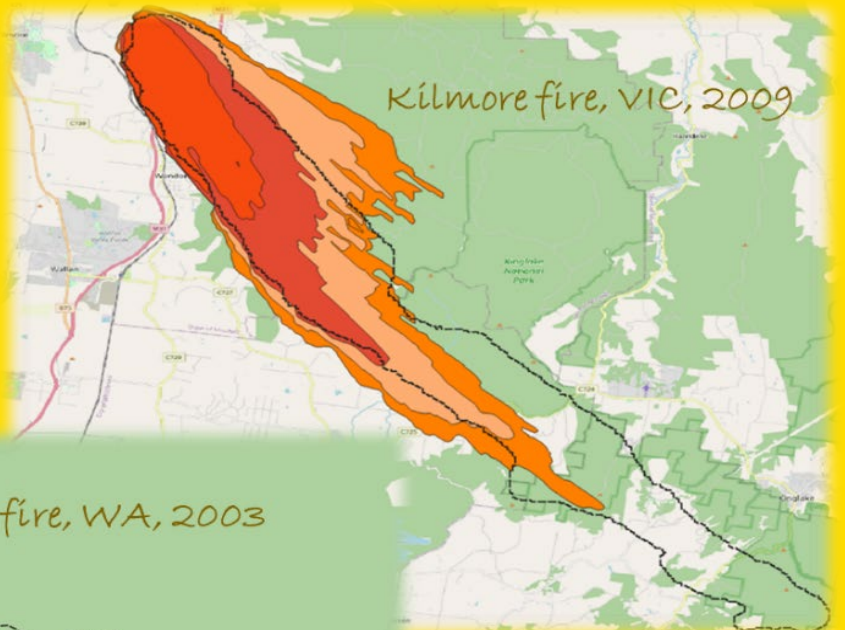
**FINAL PROJECT REPORT**

[bnhcrc.com.au](http://bnhcrc.com.au)

# **FIRE SPREAD ACROSS DIFFERENT FUEL TYPES – RESEARCH AND UTILISATION**

**Final project report**

**Nazmul Khan, Amila Wickramasinghe, Mahmood Rashid & Khalid Moinuddin**  
Victoria University





Version	Release history	Date
1.0	Initial release of document	11/05/2021



Australian Government  
Department of Industry, Science,  
Energy and Resources

**AusIndustry**  
Cooperative Research  
Centres Program

© Bushfire and Natural Hazards CRC 2021

All material in this document, except as identified below, is licensed under the Creative Commons Attribution-Non-Commercial 4.0 International Licence.

Material not licensed under the Creative Commons licence:

- Department of Industry, Science, Energy and Resources logo
- Cooperative Research Centres Program logo
- Bushfire and Natural Hazards CRC logo
- Any other logos
- All photographs, graphics and figures

All content not licenced under the Creative Commons licence is all rights reserved. Permission must be sought from the copyright owner to use this material.



**Disclaimer:**

Victoria University and the Bushfire and Natural Hazards CRC advise that the information contained in this publication comprises general statements based on scientific research. The reader is advised and needs to be aware that such information may be incomplete or unable to be used in any specific situation. No reliance or actions must therefore be made on that information without seeking prior expert professional, scientific and technical advice. To the extent permitted by law, Victoria University and the Bushfire and Natural Hazards CRC (including its employees and consultants) exclude all liability to any person for any consequences, including but not limited to all losses, damages, costs, expenses and any other compensation, arising directly or indirectly from using this publication (in part or in whole) and any information or material contained in it.

**Publisher:**

Bushfire and Natural Hazards CRC

May 2021

Citation: Khan N, Wickramasinghe A, Rashid M & Moinuddin K (2021) Fire spread across different fuel types: research and utilisation – final project report, Bushfire and Natural Hazards CRC, Melbourne.

Cover: Mount Cook fire and Kilmore fire maps.



## TABLE OF CONTENTS

<b>ACKNOWLEDGMENTS</b>	<b>4</b>
<b>EXECUTIVE SUMMARY</b>	<b>5</b>
<b>END-USER PROJECT IMPACT STATEMENT</b>	<b>7</b>
<b>PRODUCT USER TESTIMONIAL</b>	<b>8</b>
<b>INTRODUCTION</b>	<b>9</b>
<b>FIREBRAND MODELLING</b>	<b>12</b>
Background	12
Research approach	13
Findings	16
<b>FLOW THROUGH FOREST CANOPIES</b>	<b>24</b>
Background	24
Research approach	29
Findings	32
<b>GRASS AND FOREST FIRE MODELLING</b>	<b>41</b>
Background	41
Research approach	46
Findings	48
<b>KEY MILESTONES</b>	<b>61</b>
Sub-canopy wind profile modelling	61
Firebrand modelling	61
Tree and grassfire modelling	61
<b>UTILISATION AND IMPACT</b>	<b>62</b>
Background	62
Implementation	63
<b>CONCLUSION</b>	<b>76</b>
Summary	76
Next steps	77
<b>PUBLICATIONS LIST</b>	<b>79</b>
Peer-reviewed journal articles	79
Conference papers	79
Technical reports	79
<b>TEAM MEMBERS</b>	<b>81</b>
Research team	81
PhD students	81
Masters by Research students	81
End-users	81
<b>REFERENCES</b>	<b>83</b>



## ACKNOWLEDGMENTS

We acknowledge the Ancestors, Elders and families of the Boonwurrung, Waddawurrung and Woiwurrung language group of the Kulin who are the traditional owners of University land. As we share our own knowledge practices within the University, may we pay respect to the deep knowledge embedded within the Aboriginal community and their ownership of Country.

We acknowledge that the land on which we meet is a place of age-old ceremonies of celebration, initiation and renewal and that the Kulin people's living culture has a unique role in the life of this region.



## EXECUTIVE SUMMARY

It is crucial for emergency and disaster management organisations to predict of the rate of spread and intensity of bushfires for operational planning, community warnings and the deployment of their resources. Currently, this is achieved by simulation using simplified operational models that have the useful attribute of providing results on time scales commensurate with those required by emergency managers. However, when Cruz & Alexander [1] reviewed the performance of the operational fire models used by fire and emergency service analysts on seven vegetation types found in Australia, they found that on an average most of the fire models have an error of 20–80% in estimating the rate of fire spread. These differences in prediction are due to the assumptions and limitations of these models. Therefore, it is essential that these simplified operational tools be refined so that they can better predict fire behaviour. Additionally, a more physically based firebrand model needs to be included in operational models to predict firebrand distribution and subsequent spotting, which lead to an increased rate of fire spread (ROS). Currently, no such model exists. With an increased population in the rural–urban interface (or wildland–urban interface, WUI), it is also important to understand the vulnerability of houses from radiant heat and firebrand flux in order to minimise such vulnerability.

In this project, we tested two established reliable physics-based models: Fire Dynamics Simulator (FDS) and FIRESTAR3D to simulate bushfire scenarios in three broad areas:

- (1) sub-canopy wind flow,
- (2) firebrand transport, and
- (3) propagation of grass and forest fires.

We have made significant inroads into providing usable outputs as well understanding various aspects of bushfire behaviour. The following are particular highlights:

- **Modelling of wind flow through tree canopies.** We found that a simple mathematical model gives a similar wind profile to that given by the FDS in a homogeneous tree canopy on flat ground under neutral atmospheric conditions. We went on to implement this simple model (known as the Harman and Finnigan model) to generate a dynamic<sup>1</sup> wind reduction factor (WRF) in the fire spread model SPARK (developed by CSIRO Data61). Using six real-fire case studies, we demonstrated that a dynamic WRF generally provides better fire propagation prediction than a fixed WRF. Some flow simulations in heterogeneous tree canopies show interesting flow features that not only affect fire propagation but can also affect firebrand transport.
- **Modelling of transport of firebrands** (cubical, cylindrical and disc-shaped particles, representing idealised firebrands) and their landing distribution with view to developing models of ember attack for use in future iterations of Australian Standard AS3959. We extended the simulation work to study the transport of ember particles across realistic forest edges. The results

---

<sup>1</sup> Meaning WRF will vary for the geographical location and driving wind velocity and direction



show that a lower sphericity of the firebrand can increase lateral dispersion.

- **Simulations of rate of grassfire propagation** as functions of wind, grass height, slope, initial wind field with a view to improving Australian Standard AS3959. The foundations of rigorous simulation have been laid in a number of our journal publications [2, 3] and we are now exploring various parametric studies. In one such study, we evaluated heat load from incoming grassfire on structures in relation to AS3959.

This project was also established to create a capability and capacity in Australia to conduct research and understand physical-based wildfire modelling approaches. There are several international groups developing these models, and it is imperative that Australia can interact and work alongside these researchers to translate the findings to the Australian context.

Overall, we have achieved our goal of obtaining greater insight into bushfire physics and we are now utilising those insights to parameterise various phenomena for operational models.

This report explains these issues in more detail.



## END-USER PROJECT IMPACT STATEMENT

**Dr Stuart Matthews**, *Rural Fire Services, NSW*

The *Fire Spread Across Different Fuel Types* project has used detailed physical modelling and experimentation to investigate several fire spread processes and developed tools that will support operational fire prediction in the future.

Wind is one of the most important factors driving fire spread and the interaction of wind with vegetation is complex, particularly in areas with non-homogeneous vegetation and topography. The high-resolution fluid dynamics modelling completed by the project has produced valuable insights about flow in and around vegetation, as well as practical tools for modelling the wind reduction factor (WRF) used in operational spread modelling. The testing of the WRF models in the SPARK modelling framework demonstrates the path from detailed physical research to operational application, a key aim of the BNHCRC.

Modelling fire spread using physical simulations is a challenging area that has the potential to offer insight into aspects of fire behavior that are difficult to measure experimentally, either because of the difficulty of measuring fire characteristics inside a fire, or because some experiments are too dangerous or difficult to conduct at field scale. The team have done valuable work implementing and applying the WFDS and FIRESTAR3D systems to test cases in Australian fuels including exploration of the effects of fuels and slope of fires.

Understanding the aerodynamics and dispersion of firebrands is very relevant both for including their contribution to fire spread in forests as well as predicting (and preventing) the impact of embers on buildings. The team have developed a new experimental capability with the 'firebrand dragon' and derived a better understanding of ember dynamics by combining experimental results with numerical simulation. Combined with more realistic modelling of flame radiation, this area of work shows promise for application in the area of building design and building standards that reflect the real-world conditions that houses and other structures are exposed to during ember attack.



## PRODUCT USER TESTIMONIAL

**Dr James Hilton**, *Principal Research Scientist, CSIRO Data-61*

The wind-reduction factor (WRF) model can be implemented in SPARK as a pre-processing step. This acts as a refinement for the wind speed experienced by the fire front based on the local vegetation conditions. In recent tests, this refinement has shown remarkable results in predicting historical fires, aspects of which were previously difficult to simulate. The model can be applied at a local scale based on remotely sensed data, allowing very fine-scale correction of the wind speed and the potential for more accurate large-scale simulations.





## INTRODUCTION

Bushfire is a significant threat to countries like Australia, the USA, Canada and Portugal [4] that causes loss of properties worth billions of dollars and lives of humans and other living species. In the summer 2019–2020 bushfires, as of 9 March 2020 in Australia, fires had burnt 18.6 million hectares, destroyed over 5900 buildings and killed at least 64 people [5-8]. In the past, the Black Saturday bushfire of 2009 alone resulted in economic costs of AUD 4.4 billion and destroyed ~3500 structures [4, 9]. Previously, the 2003 Canberra fire [10] destroyed ~390 houses, costing AUD 0.35 billion in losses. Over the past decade, the frequency of bushfires around the world has increased [11]. Ronchi *et al.* [4] reported some of the economic costs of wildfire in North America to be between USD 0.4 and 7 billion in the last decade. The effect of these bushfires is not limited to economic damage; they also cause massive evacuation of communities and present challenges to emergency personnel. The Black Saturday fire in Australia caused ~7500 people to evacuate [9]. Many people who did not evacuate early died during their attempted late evacuation, and the high number (173) of fatalities in the 2009 Black Saturday fire is one bushfire case where late evacuation resulted in the loss of life [9, 12].

To mitigate the bushfire threat and to apply appropriate suppression strategies, the operational agencies rely on the prediction of the fire forward rate of spread, flame characteristics and possibilities of firebrands being thrown ahead of the fire front to start new fires. However, the prediction of fire spread is a highly complex task owing to the many factors affecting the rate of spread (ROS) of fires, such as wind speed and turbulence, vegetation types and densities, ages of vegetation, fuel moisture content, atmospheric stability conditions, conditions of terrains and firebrand generation and transport. The formation of plumes and firebrand transport add extra uncertainties that are also modified by each parameter listed above affecting the ROS. The question may arise whether wildland fire can really be predictable. The minute-by-minute exact movement of a fire will probably never be predictable with weather forecast some hours before the actual fire [13]. However, an advanced science-based knowledge and prediction tool can explore complex fire spread scenarios more effectively, thereby helping to save lives and properties through an appropriate suppression plan.

It is essential that emergency and disaster management organisations be able to predict the ROS and intensity of bushfires with reasonable accuracies. Currently, this is achieved by implementing simplified operational models that have the useful attribute of providing results on time scales commensurate with those required by emergency managers. However, Cruz & Alexander [1] reviewed the performance of the operational fire models used by fire and emergency service analysts on seven vegetation types found in Australia, and found that on an average, most of the fire models have a mean absolute error of 20–80% in estimating the predictive rate of fire spread. The above differences in prediction are due to the assumptions and limitations of these models. Therefore, it is essential that these simplified operational tools be refined so that they can predict fire behaviour under a wide range of localised topographic and weather conditions; they also need to be able to account for a range of inhomogeneity, slope and thermal instability within vegetation and terrain.



To help ensure that operational wildfire models are accurate and flexible, in Stage 1 of this project (2014–2016), we established and numerically tested a reliable physics-based model that is based on fundamental fire dynamics and the corresponding differential equations to simulate bushfire scenarios. The end goal of our work is to improve bushfire modelling so that risks and losses associated with bushfires can be reduced.

Operational wildfire models, such as the McArthur model [14], give the ROS as a function of various fuel parameters, ambient weather conditions, the slope of the terrain and the average wind speed measured over open ground at a height of 10 m. Because of the drag caused by the vegetation, the average wind speed within a tree canopy will be less than the open wind speed. This reduction in wind speed is modelled by a wind reduction factor (WRF). As the wind speed within a canopy varies as the measurement point moves away from the surface, WRF can be a function of height. With the physics-based model, we investigated the effect of a tree canopy on near-surface wind speed and found that the sub-canopy winds vary at all spatial locations. The shape of the centreline streamwise velocity profile is determined by the drag exerted by trunks and large branches. As the leaf area density (LAD) varies, so the sub-canopy velocity profile varies. The predicted WRF was found to be consistent with the observations of Moon *et al.* [15]. A simple model, Harman and Finnigan [16], of the sub-canopy wind profile was tested. The predicted profile from physics-based modelling was found to be quantitatively correct for the most developed sub-canopy wind. The simple model can be applied with very little information, namely the wind velocity far above the canopy, the vegetation height and the leaf area index (LAI) (considering the LAD does not vary with vegetation height). The result can be used to provide an estimate of the sub-canopy wind speed and hence construct an estimate of the WRF. In the utilisation stage of the project (2017–2020), we aimed to implement the Harman and Finnigan [16] model into an operational model to estimate dynamic<sup>2</sup> WRF based on instantaneous wind velocity, vegetation height and LAI at different locations (in a 1 x 1 km grid). This can be found in the *Utilisation and Impact* section starting on p. 72 of this report. In addition, to explore the fundamental behaviour of sub-canopy wind, we intended to study

- flow through heterogeneous tree canopies
- the effect of wind downstream of a canopy edge on surface fire propagation
- flow over canopies on terrain slope

The second stream of research we pursued in Stage 1 (2014–2016) was grassfire propagation. Fires in grasslands are prevalent in Australia and are relatively simple to model computationally owing to the uniform fuel and flat simple terrain. We used CSIRO grassland experiments as validation cases for the physics-based simulations. A parametric study was conducted where the background wind speed and the grass height were varied independently. The ROS was found to be linear with wind speed in the parameter range considered. We also observed two modes of fire propagation, namely wind-driven and plume-driven. In this

---

<sup>2</sup> Meaning WRF will vary for the geographical location and driving wind velocity and direction



utilisation stage (2017–2020), we aimed to study the effects of terrain slope in detail.

The third stream we investigated in Stage 1 (2014–2016) was short-range spotting and establishing capability of the physics based model in reliably modelling short-range firebrand transport. In the utilisation stage (2017–2020), we aimed to use the physics-based model's grassfire and short-range firebrand sub-model for mapping radiation, flame and ember attack load on structures in wildland–urban interface (WUI) areas and to improve Australian Standard AS3959 [17].

It is worth mentioning that in the current stage (2017–2020), which is primarily focused on utilisation, we have extended our fundamental research. In relation to utilisation, WRF implementation has been successful, and modelling firebrand transport and heat flux on buildings as well as parametric study of grassfires are ongoing; these are discussed in the *Utilisation and Impact* section.



## FIREBRAND MODELLING

### BACKGROUND

Firebrands, commonly called embers in Australia, are the burning pieces of twig, leaf, nut and bark material that travel with the wind and ignite vegetation ahead of the fire front. The ignition caused by the transport of firebrands is called spotting, which can be classified based on the distance travelled by firebrands as: (1) short-range (<750 m); (2) medium-range (1000–5000 m); and (3) long-range (>5 km) spotting [18]. In short-range spotting, the firebrands travel along with the wind with no lofting up to 750 m. Most short-range firebrands are flaming (as opposed to smouldering) and are just material broken from trees. In medium-range spotting, firebrands lofted with the convective air column may travel more than 1 km. These firebrands are typically burned off and usually in the glowing (smouldering combustion) state [19–21].

Most of the research in the last decade [19–23] has focused on long-range spotting, which causes significant losses in bushfires. In the Black Saturday fire of 2009 in Victoria, long-range firebrands travelled up to 30 km [9, 19]. Short-range firebrands contribute to increasing the ROS by causing spot fires, which coalesce with the primary fire front, as described by Huygens' wavelet principle [24]. There has been no significant research carried out in understanding the phenomena of short-range spotting and its coalescence with the primary fire front [18]. It has been argued that poor prediction of firebrand transport and spotting is a major reason for the under-prediction by fire models used by emergency services [18, 24-26].

Fire dynamics simulator (FDS), developed by the National Institute of Standards and Technology (NIST) [27], is one of most-used open-source software for physics computational fluid dynamics (CFD)-based modelling [26]. FDS is widely used in building fires. However, Mell *et al.* [28, 29] extended the capability of FDS for wildfires to develop the Wildland–urban interface Fire Dynamic Simulator (WFDS). FDS/WFDS solves the thermally driven Navier–Stokes equation to simulate the propagation of fire. A Lagrangian particle model, one of the sub-models of FDS, is used to simulate the transport of particles in the flow field. The model is extensively verified and validated for liquid particles like droplets and mist [30, 31]. However, the verification and validation for solid particles are very limited. We attempted to validate [32] the applicability of the inbuilt Lagrangian particle model of FDS [33] for the transport of non-burning and burning firebrands. We observed that the FDS inbuilt model under-predicts the spatial distribution of cubiform and cylindrical firebrand particles. It was suspected that the simulation was not accounting for the secondary motion of particles like tumbling and rolling thus providing a higher drag force on the particles [33]. The FDS Lagrangian particle model [27, 33] treats particles as point particles; hence, the secondary motion of the particle is not incorporated.

The present work focuses on answering the issues identified in our work above; in particular, we modified the inbuilt drag model for the Lagrangian particles to account for the effect of tumbling while retaining a fundamental point particle model. We limited ourselves to point particles owing to two main reasons. Firstly, the physics-based fire models are computationally expensive and are not



applicable at scale for more than a plot of a few hundred square metres in area [4]. Secondly, the application of fire models like PHOENIX, SPARK and FARSITE is operated at a square grid size of 15–30 m<sup>2</sup> [4]. Hence, various commonly used drag laws in the literature were tested to improve the spatial distribution of cubiform, cylindrical and square disc particles without making major changes in FDS that might reduce its computation speed. The drag models tested in the present work are: Haider & Levenspiel [34], Ganser [35], Hölzer & Sommerfeld [36], Bagheri & Bonadonna [37]. The improvement in FDS was carried out by modifying the FDS source code to improve the accuracy of the spatial distribution of non-burning and burning firebrands.

## RESEARCH APPROACH

To be credible, physics-based models must be validated against the experimental data. Hence, a firebrand generator was designed and constructed so that the distribution of firebrands and its associated parameters could be measured. Previously, NIST has developed a firebrand generator [38], dubbed a 'fire dragon', to study the interaction of firebrands with buildings, but the NIST generator suffers a serious deficiency. The problem was: the outlet from which the burning firebrands disgorge resembles a dragon's mouth set atop a long vertical neck. As a result, the firebrands are conveyed around a 90° bend immediately before they are projected outwards horizontally. Hence, the distributions of the firebrands and air velocity at the dragon's mouth are highly non-uniform. We designed a new firebrand generator eliminating the bend and involving two co-axial pipes that produce uniform air velocity at the mouth [32]. Figure 1 shows the firebrand dragon at our facility.



FIGURE 1: FIREBRAND DRAGON CONSTRUCTED AT OUR FACILITY TO GENERATE REPEATABLE UNIFORM FIREBRAND SHOWERS.

Figure 2 shows a still image of a glowing firebrand coming from the firebrand dragon. Owing to the very fast movement of firebrand particles, it is very hard to observe their trajectory. The experimental scenario was used to validate the Lagrangian sub-model for burning particles. A preliminary result of the trajectories



by naked eye and scattering distribution of burning firebrands is shown in Figure 3.



FIGURE 2: ONE OF THE FIREBRANDS COMING FROM THE FIREBRAND DRAGON. OWING TO VERY FAST MOVEMENT OF THE FIREBRAND, ATTEMPTING TO CAPTURE A STILL IMAGE WAS VERY HARD.

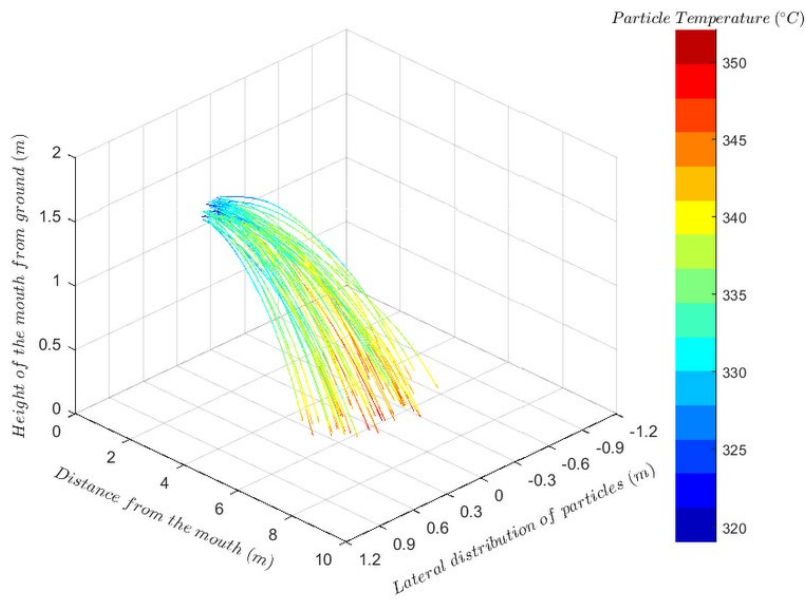


FIGURE 3: TRAJECTORY OF BURNING CUBIFORM PARTICLES FROM THE FIREBRAND GENERATOR MOUTH. THE VARIATION IN STREAMLINE COLOUR DENOTES VARIATION IN THE PARTICLE TEMPERATURE.

The drag model is the key component of particle transport in a physics-based model. The drag models implemented and tested in the physics-based model are listed in Table 1.



TABLE 1: LIST OF DRAG MODELS TESTED IN THIS WORK.

Serial No.	Drag model	Drag correlation
1	FDS Spherical drag model [33]	$C_{D,sph} = \begin{cases} \frac{24}{Re_D} & , Re_D < 1 \\ \frac{24(0.85+0.15Re_D^{0.687})}{Re_D} & , 1 < Re_D < 1000 \\ 1 & , Re_D > 1000 \end{cases}$
2	FDS Cylindrical drag model [33]	$C_{D,cyl} = \begin{cases} \frac{10}{Re_D^{0.8}} & , Re_D < 1 \\ \frac{10(0.6+0.4Re_D^{0.8})}{Re_D} & , 1 < Re_D < 1000 \\ 1 & , Re_D > 1000 \end{cases}$
3	Haider & Levenspiel [34]	$C_{D,Ha} = \frac{24}{Re_D} (1 + ARe_D^B) + \frac{C}{1 + \frac{D}{Re_D}} \quad , \quad Re_D < 2 \times 10^5$ <p>where</p> <p><math>A = \exp(2.3288 - 6.4581\psi + 2.4486\psi^2)</math>  <math>B = 0.0964 + 0.5565\psi</math>  <math>C = \exp(4.905 - 13.8944\psi + 18.4222\psi^2 - 10.2599\psi^3)</math>  <math>D = \exp(1.4681 + 12.2584\psi - 20.7322\psi^2 + 15.8855\psi^3)</math></p>
4	Ganser [35]	$\frac{C_{D,Ga}}{K_2} = \frac{24}{Re_D K_1 K_2} (1 + 0.1118(Re_D K_1 K_2)^{0.6567}) + \frac{0.4305}{1 + \frac{3305}{Re_D K_1 K_2}} \quad ,$ <p><math>Re_D K_1 K_2 \leq 10^5</math>          where  <math>K_1</math> &amp; <math>K_2</math> is the shape factor in Stokes and Newton regimes          For isometric particles, <math>K_1 = [0.3333 + 0.6667\psi^{-0.5}]^{-1}</math> and  <math>K_2 = 10^{1.8148(-\log\psi)^{0.5743}}</math></p>
5	Hölzer & Sommerfeld [36]	$C_{D,Ho} = \frac{8}{Re_D \sqrt{\psi_\perp}} + \frac{16}{Re_D \sqrt{\psi}} + \frac{3}{\sqrt{Re_D} \psi^{0.75}} + 0.42 \cdot 10^{0.4(-\log\psi)^{0.2}} \frac{1}{\psi_\perp} \quad , \quad Re_D \leq 10^7$ <p>where <math>\psi_\perp</math> is called crosswise sphericity</p>
6	Bagheri & Bonadonna [37]	$C_{D,Ba} = \frac{24k_S}{Re_D} \left( 1 + 0.125 \left( Re_D \frac{k_N}{k_S} \right)^{2/3} \right) + \frac{0.46k_S}{1 + \frac{5330}{Re_D \frac{k_N}{k_S}}} \quad , \quad Re_D < 3 \times 10^5$ <p>where</p> <p><math>k_S = \frac{(F_S^{1/3} + F_S^{-1/3})}{2}</math>, <math>k_N = 10^{\alpha_2[-\log(F_N)]\beta_2}</math>,  <math>\alpha_2 = 0.45 + \frac{10}{\exp(2.5 \log(\rho') + 30)}</math>, <math>\beta_2 = 1 - \frac{37}{\exp(3 \log(\rho') + 100)}</math>          apparent density(<math>\rho'</math>) = <math>\frac{\rho_{solid, particle}}{\rho_{fluid, air}}</math>, <math>F_S = fe^{1.3} \frac{d_{eq}^3}{LIS}</math>  <math>F_N = f^2 e \frac{d_{eq}^3}{LIS}</math>, fatness(<math>f</math>) = <math>S/l</math>, elongation (<math>e</math>) = <math>l/L</math></p>

The particles tested are (i) cubiform: average length 12.45 mm, and mass 0.83 g (0.12 g std. dev.); (ii) cylindrical: average length 11.6 mm, diameter 6.2 mm, and mass 0.17 g (0.01 g std. dev.); and (iii) square disc: average length 10.18 mm, thickness 2.22 mm and mass 0.12 g (0.01 g std. dev.). The spatial distributions of particles are measured using particle imaging, and their first impact location is noted (Figure 4). The final distribution of particles is ignored owing to the collision



between particles and surface being complicated to account for the simulation. The spatial distribution is measured on a surface grid of 20-cm spacing.

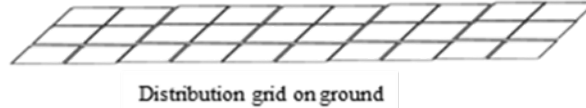


FIGURE 4: EXPERIMENTAL RIG TO STUDY THE SPATIAL DISTRIBUTION OF PARTICLES FROM THE PROTOTYPE [32].

Simulations of experimental scenarios are carried out using FDS 6.2.0. The domain of the simulation is 7 m long, 1.2 m wide and 2 m high respectively in the x-, y-, and z-directions. The simulation domain is sub-divided into four sections (Figure 5),  $x = 0-0.5$ ,  $0.5-1.5$ ,  $1.5-2.5$ , and  $2.5-7$ -m with uniform grid sizes ( $\Delta x = \Delta y = \Delta z$ ) 5, 10, 20 and 40 mm respectively. Grids near the dragon mouth are the finest and as the distance from the mouth increases, coarser grids are used. Domain discretising by appropriate grid (cell) size is significant in quantitative numerical analysis and results should be grid-converged. Therefore, a grid sensitivity analysis was carried out and demonstrated that the adopted grid setting gives grid-converged solutions.

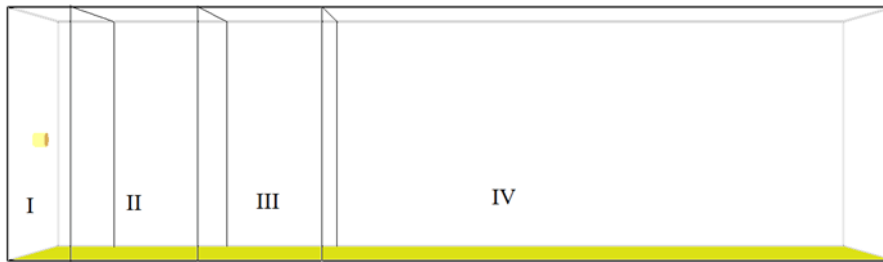


FIGURE 5: FDS SIMULATION DOMAINS TO SIMULATE PARTICLE DISTRIBUTION DIVIDED INTO FOUR SECTIONS WITH DIFFERENT GRIDS [32]; 5, 10, 20 AND 40MM GRIDS ARE USED FOR SECTIONS I, II, III AND IV, RESPECTIVELY.

To represent experimental work accurately, six simulation particles densities ( $\bar{\mu} \pm \sigma/4$ ,  $\bar{\mu} \pm 3\sigma/4$  and  $\bar{\mu} \pm 3\sigma/2$ ; where  $\bar{\mu}$ ,  $\sigma$  are the mean density and the standard deviation of particle densities respectively) are used to represent the particles in the experiment. The mean (and standard deviation) of cubiform, cylindrical and square disc particle densities are 428.3 (48.9), 492.9 (44.3) and 512.5 (35.9)  $\text{kg/m}^3$ .

## FINDINGS

### Model variation with firebrand generator experiment

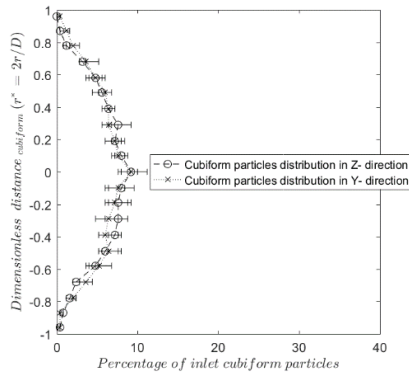
The particles' distribution and their component velocities were measured using a 720-pixel camera at 120 fps. The experimental distribution of the cubiform, cylindrical and square disc particles in two orthogonal directions of the flow is shown in Figure 6.

The distribution is almost uniform at the mouth of the prototype (Figure 6), although the distribution is slightly skewed in the z direction for cubiform particles owing to the weight of the individual particles. The distribution is approximately a normal distribution due to very low loading rate of the particles. The components of particle velocity ( $u$ ,  $v$  and  $w$ ) are measured by displacement of the centroid of the particle streak using particle image velocimetry (PIV) [39].

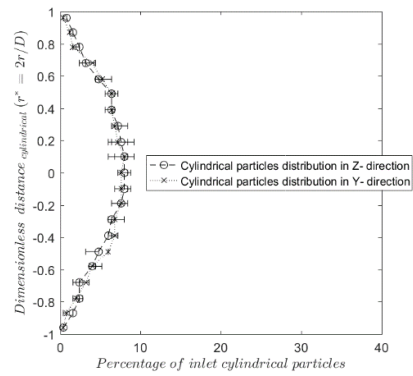




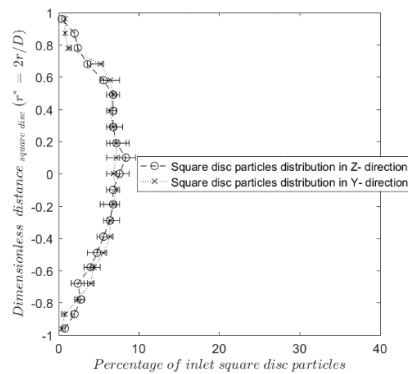
The measured components of particle velocities for cubiform particles are 12.5, 0.0, 0.0 m/s with std. dev. of 0.8, 0.6 and 0.6 m/s respectively. Similarly, for cylindrical particles, they are 13.4, 0.2, 0.2 m/s with std. dev. of 0.9, 0.7 and 0.8 m/s, respectively. For square disc particles, they are 13.2, 0.0, 0.0 m/s with std. dev. 1.1, 0.9, 1.1 m/s, respectively.



(a) Cubiform particles [32]



(b) Cylindrical particles [32]



(c) Square disc particles

FIGURE 6: DISTRIBUTION OF THE PARTICLES AT THE MOUTH OF THE PROTOTYPE GENERATOR.

Figure 7 shows the trajectory of all three shapes of particles from the prototype mouth. It can readily be seen that square disc particles spread more in a lateral direction compared with the cubiform and cylindrical particles. This effect can be seen in the contour plots of the landing distribution of all three types of particles below.

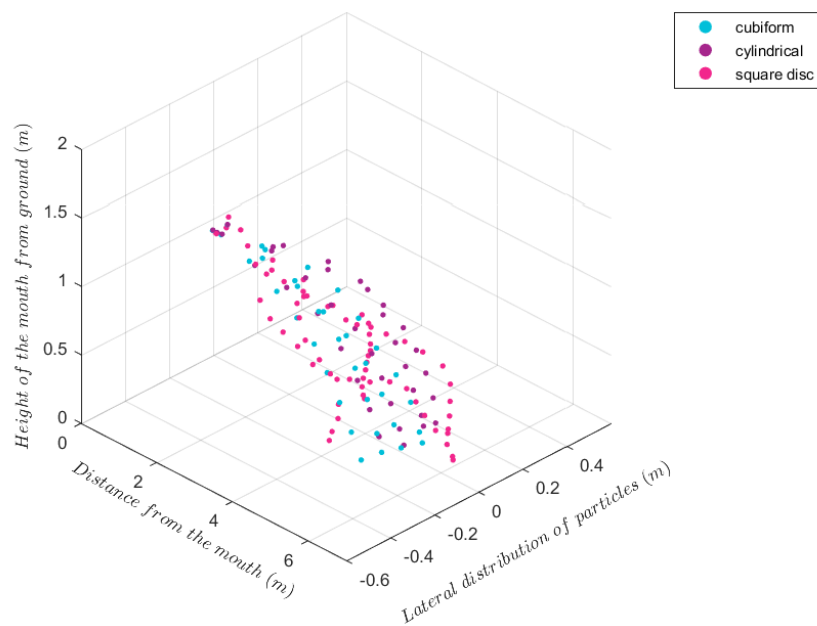
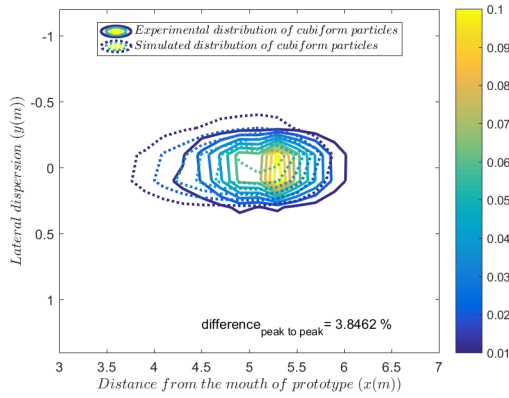


FIGURE 7: TRAJECTORY OF ALL THREE SHAPES OF PARTICLES FROM PROTOTYPE MOUTH.

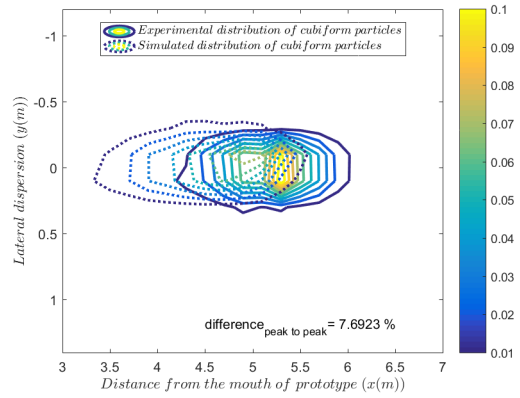
Figure 8 shows the comparative contours of simulated and experimental spatial distributions for cubiform particles with different drag models. From Figure 8(a), we see that for cubiform particles, the default FDS drag model for spherical particles provides the best fit with the experimental observations. The cubiform particle suffers a much smaller tumbling effect due to its regular shape in all three directions and hence tumbling has much less impact on the drag coefficient. Moreover, the literature model used for cubiform particles tends to underpredict the spherical drag model, which may be due to over-estimation of drag coefficients. The reported mean errors in estimating the drag coefficient by the Haider & Levenspiel, Ganser, and Hölzer & Sommerfeld models in predicting the drag coefficients are: 42.3 %, 38.4 % and 27.2 % [36] respectively.

For particles shapes like the cylindrical and square disc, tumbling and secondary motion play a crucial role. It can be seen for cylindrical particles in Figure 8 that the default drag model of FDS under-predicts the peak of first impact location of the particles. The tested literature drag models improve the under-prediction between the experimental and simulated observations. The Haider and Levenspiel drag model showed the best improved result among the tested drag models (Figure 8).

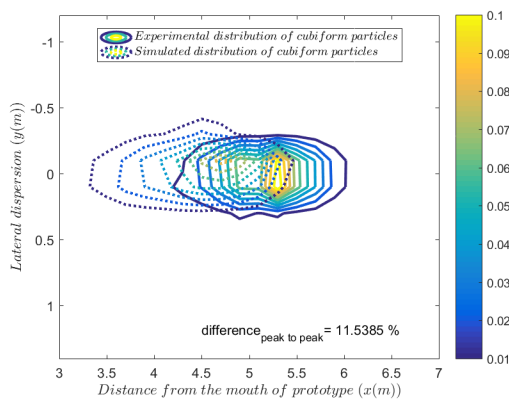
For square disc particles, only the literature drag models are tested (Figure 9). Owing to the computational domain limit, the lateral spread of the particles is limited from  $-0.6$  to  $0.6$  m. Square disc particles are observed to spread significantly more than the cubiform and cylindrical particles. The Bagheri & Bonnadonna drag model shows the best fit among the models tested as it is derived from the Hölzer & Sommerfeld drag model. The Hölzer & Sommerfeld drag model shows good improvement in the mean error for estimating the drag coefficient from  $\sim 2000\%$  (Haider & Levenspiel, and Ganser drag models) to  $\sim 17\%$ .



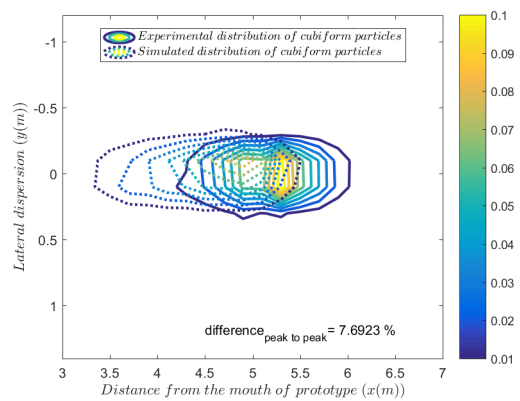
(a) FDS default drag model [32]



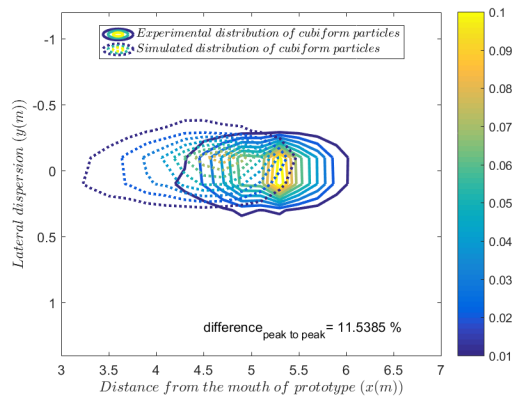
(b) Haider & Levenspiel drag model



(c) Ganser drag model



(d) Hölzer & Sommerfeld drag model



(e) Bagheri & Bonnadonna drag model

FIGURE 8: SPATIAL DISTRIBUTION OF CUBIFORM PARTICLES WITH DIFFERENT DRAG MODELS.

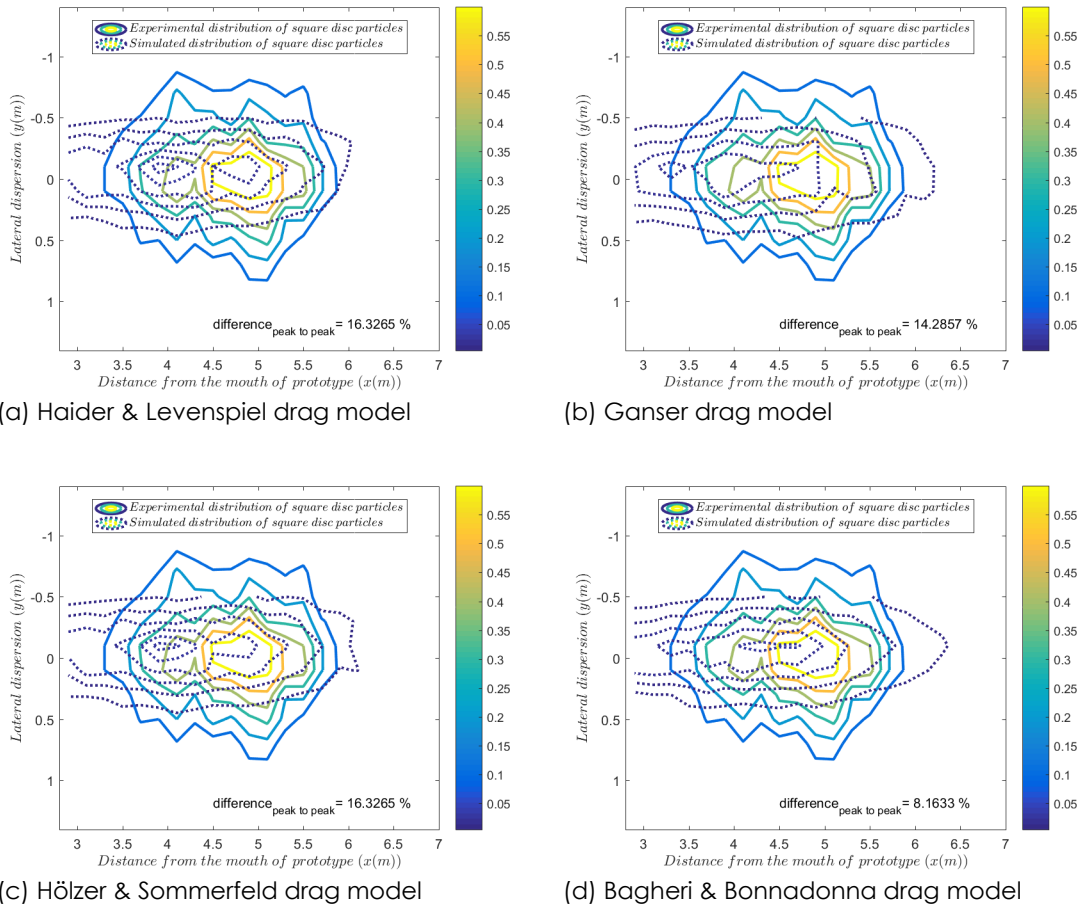


FIGURE 9: SPATIAL DISTRIBUTION OF SQUARE DISC PARTICLES WITH DIFFERENT DRAG MODELS.

### Validation of a burning tree and inverse analysis for firebrand generation

After validation with firebrand generator experiments, we aimed to find what firebrand numbers, masses and sizes are generated at what velocity and in which direction from a burning Douglas fir tree. This is because modelling mechanisms of firebrand production/tear-off and firebrands burning is extremely difficult and beyond the capability of the FDS model; thus, we wished to obtain firebrand generation parameters from a single Douglas fir tree (essentially leading to per MW forest fire or kg mass consumed) through inverse analysis and use them as the source terms for firebrand transport modelling in the WUI.

The burnable mass of the tree consists of needles, and two different types of twigs. The 2.6-m-high tree is modelled as shown in Figure 11 (a). The tree geometry is taken as a cone having a height of 2.6 m and girth of 1.5 m, as for the original tree in Manzello *et al.* [40]. A domain of  $8 \times 8 \times 10$  m size was used for the simulations to capture all flames (represented by heat release rate per unit volume iso-surfaces) and cover the area of firebrand collection. Figure 10(a) shows a snapshot of Smokeview with x and z domain sizes and the tree is located at (0, 0, 0) coordinates of the xyz plane. The base height of the tree is 0.15 m relative to the bottom plane.

Collected firebrand mass and size (length and diameter) data from a burning tree is available from the laboratory experiment conducted at NIST [40]. Firebrand data (mass and size) collected in pans as shown in Figure 10(b) were



categorised into 30 mass classes. These classes range from 0.005 to 2.000 g. Firebrands are released throughout the volume of the model tree. Tree burning was almost complete after 30 s in the laboratory experiment [40]. Therefore, the firebrand generation time is maintained for 30 s. Total simulation time is kept at 45 s to provide sufficient time for firebrands to land on the ground surface. There is no wind flow and firebrands move and settle under fire-induced buoyancy and gravity. The default ‘cylinder’ drag law of FDS is used for firebrands to replicate the drag force on their movement. A firebrand insertion time interval for each mass class is set to ensure that the desired number of firebrands are inserted over the burning period. Pans are represented by rectangular-shaped devices in FDS to measure accumulated firebrand landing mass.

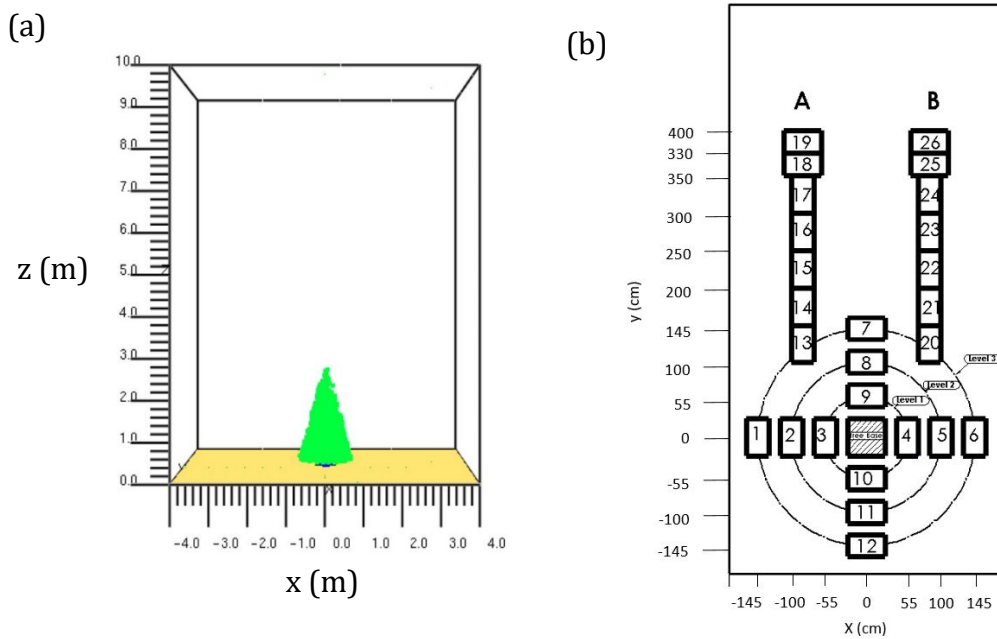
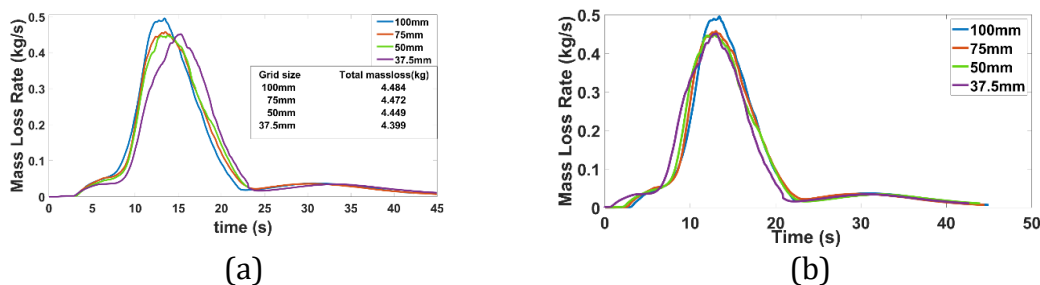


FIGURE 10: (A) SMOKEVIEW REPRESENTATION OF MODEL TREE (AT 0 S) WITH X, Y DOMAIN SIZES. THE PLAN VIEW OF THE FIREBRAND COLLECTION PAN ARRANGEMENT IS SHOWN IN (B). THE PANS ARE NUMBERED 1 TO 26 AND THE TREE BASE IS AT THE MIDDLE OF THE 1–6 AND 7–12 PAN SERIES. A, B ARE IN PARALLEL ARRANGEMENT. PANS IN WHICH FIREBRANDS LANDED ARE IN CIRCULAR LEVELS 1, 2 AND 3.

First, the tree burning was validated. For physics-based modelling, thermo-physical parameters were taken from previous studies [29, 41] of individual Douglas fir trees burning. A grid convergence analysis was carried out using 100-, 75-, 50- and 37.5-mm grid cells in terms of mass loss rate (MLR) and heat release rate (HRR). The simulation results with each grid size are presented in Figure 11. The results with 50- and 37.5-mm grids closely match. Further, a Grid Convergence Index (GCI) was calculated for 100- to 37.5-mm grid sizes. A minimum GCI of 4% was found in 75-mm/50-mm grid sizes. Therefore, the 50-mm grid size can be considered reasonable to use in this tree burning simulation.



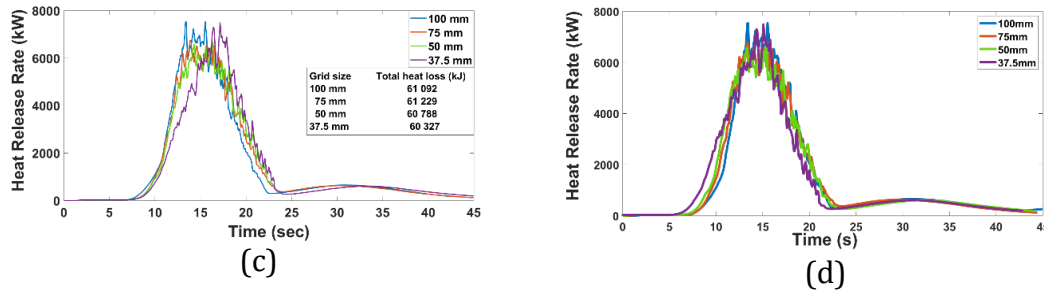


FIGURE 11: (A) COMPARISON OF MASS LOSS RATE (MLR) RESULTS FOR 2.6-M DOUGLAS FIR TREE SIMULATION FOR GRID SIZES 100, 75, 50 AND, 37.5 MM. (B) MLR RESULTS AFTER PEAK SHIFTING. (C) COMPARISON OF HEAT RELEASE RATE (HRR) FOR GRID SIZES 100, 75, 50 AND, 37.5 MM. (D) HRR RESULTS AFTER PEAK SHIFTING.

Figure 12 shows the comparison of experiment and simulation results obtained using a 50-mm grid. Simulation is reasonably close to the experiment and the difference in total mass loss is about 8.5%. The peak mass loss rate of the experiment is 0.417 kg/s whereas the simulation shows it as 0.447 kg/s, a 6.7% difference. The shapes of the two curves are qualitatively similar. Here, the experimental MLR profile was shifted to align with the simulation for better comparison.

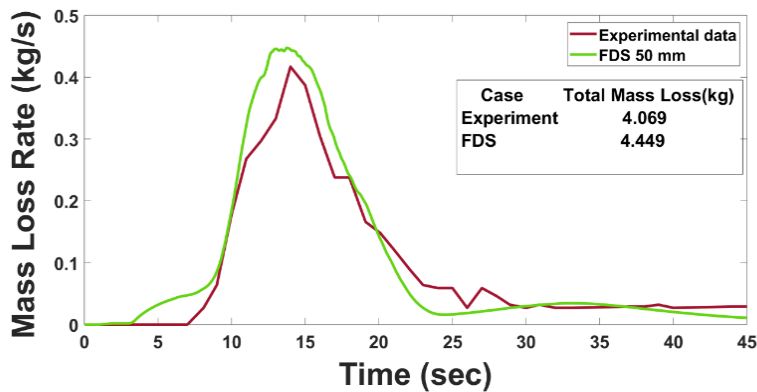


FIGURE 12: MLR COMPARISON OF EXPERIMENT AND 50-MM GRID SIZE FDS. THE SHAPES OF THE TWO CURVES ARE IN REASONABLE AGREEMENT. SIMULATION RESULTS SHOW HIGHER TOTAL MASS LOSS DURING THE SIMULATION TIME OF 45 S.

Then, an inverse analysis was carried out to find the initial firebrand velocity and direction (as model inputs) required to reach collection pans subject to the influence of fire-induced buoyancy and gravity forces. With this analysis, vertical and horizontal velocity components of 70 and 210 cm/s were taken as the initial velocities of firebrands generated by the burning tree. The firebrand generation number was examined by inputting different multiplication factors (4, 5, 6, etc.) of experimental firebrands collected (70). Table 2 shows the input and collected firebrand mass for different multiples of collected firebrands. The total mass of firebrands collected in the laboratory experiment was  $18 \pm 4$  g. Inputting  $5 \times 70$  firebrands in the simulation produced 18.9 g, which agrees well with the experiment. The sensitivity of the FDS particle model was examined by comparing the total mass of firebrands received by the collection pans using different grid sizes. It was found that the firebrand mass distribution difference was  $-6\%$  to  $+5\%$  for 100 mm to 37.5 mm grids relative to the 50-mm grid.



TABLE 2: MASS RECEIVED BY PANS WITH DIFFERENT INPUT OF NUMBERS OF FIREBRANDS

Case	Number of firebrands	Mass (g)	
		Inserted	Collected
1	70 x 4	66.80	16.45
2	70 x 5	86.92	18.90
3	70 x 6	99.40	26.36

Overall, through inverse analysis, from a 2.6-m-high single Douglas fir tree burning in the absence of wind, we estimate that 350 particles in 30 mass classes are generated with 70 cm/s vertical velocity and 210 cm/s horizontal velocity. This can be used as a source term of the model in field-scale modelling to assess risks to structures.

## FLOW THROUGH FOREST CANOPIES

### BACKGROUND

Numerical simulation of fluid flows and in particular atmospheric flow has been established since the pioneering work of Deardorf [42]. In recent years, large-eddy simulation (LES) has become the preferred tool for studying many aspects of atmospheric flows and it underpins the numerical weather prediction models used today. Some modelling work has been conducted using the Reynolds-averaged Navier–Stokes equations (RANS) approach.

In LES, the equations describing conservation of mass and momentum in a fluid (the continuity and Navier–Stokes equations respectively) are spatially filtered, retaining the dynamically important large-scale structures of the flow. The effect of the smaller scales on the resolved large scales is then modelled. In the code we used, this filtering is performed implicitly at the grid scale. The LES equations are

$$\frac{\partial u_i}{\partial t} + u_j \left( \frac{\partial u_i}{\partial x_j} - \frac{\partial u_j}{\partial x_i} \right) = -\frac{1}{\rho} \frac{\partial p}{\partial x_j} + \frac{\partial \tau_{ij}}{\partial x_j} + F_{D,i} , \quad (1)$$

$$\frac{\partial u_i}{\partial x_i} = 0, \quad (2)$$

where  $u_i$  is the resolved part of the velocities,  $p$  is the (modified) pressure,  $\tau$  is the deviatoric part of the subgrid-scale stress tensor, which can be modelled using different LES models such as the constant Smagorinsky (see for example Pope [43]), and  $i, j = x, y, z$  are the coordinates.  $F_{D,i}$  can represent external forces such as gravity, aerodynamic drag, etc.

The literature on LES for atmospheric and canopy simulations is extensive. In particular, studies by Bou-Zied [44, 45] and Porté-Agel *et al.* [46] show that LES can reproduce experimentally observed velocity profiles and higher-order turbulence statistics. Therefore, this simulation approach is appropriate for the present study. For a more complete discussion of LES methods, see Pope [43]. The set of simulations is conducted in a large domain with a rectangular canopy, and a neutral atmosphere, that is one without buoyant effects, is considered in the interests of controlled numerical experiments assessing the effect of varying only the canopy parameters. The canopy itself is modelled as an aerodynamic drag term [47]. That is,

$$F_{D,i} = -\chi(x, y, z) \frac{\rho}{2} c_D \alpha(z) u_i u_i, \quad (3)$$

where  $\chi(x, y, z)$  is one if  $(x, y, z)$  is inside the rectangular canopy region and zero otherwise. The fluid density is denoted  $\rho$  and the drag coefficient is  $c_D$ . The drag coefficient was found to be fairly constant across forest types at around  $c_D = 0.15$  by Amiro [48].  $\alpha(z)$  is the leaf area density (LAD) of the canopy, which is assumed to only vary with height. We choose the LAD to follow a Gaussian profile following the literature (see for example Cassiani *et al.* [49]).





Operational models such as the McArthur [14] and Rothermel [50] models use wind reduction factors (WRFs) to predict fire spread. Such models were derived from experimental studies. The WRF is used to compensate for additional drag from the tree canopy when the model is applied to a forest type that is different to the forest type in the original model.

The WRF values are currently unscientific, with agencies using broad, experienced-based 'rules of thumb' to estimate them. Essentially, to estimate the WRF, one estimates both the sub-canopy wind speed at some height within the canopy and the unobstructed, or open, wind speed at some height far from the canopy (S. Heemstra, RFS, NSW). Typically, the sub-canopy wind speed is measured at 2 m and the open wind speed is measured at 10 m [15]. The WRF is then the open wind speed divided by the sub-canopy wind speed. A related definition is the wind adjustment factor (WAF), which is simply the inverse of the WRF.

It is desirable to predict sub-canopy winds a priori with a simple formula. Indeed, this would be sufficient to construct a model of the WRF because the open wind speed may be either forecast by some numerical weather prediction, or measured in the field. Sub-canopy winds under neutral atmospheric conditions have been successfully simulated using physics-based models for a considerable time. Recently, LES has emerged as the preferred tool for simulating the lower atmospheric boundary layer over rough surfaces [51], canopies [52] and urban areas [45]. The simulation data has been validated against experimental and field observations; simulations of complicated flows have satisfactorily reproduced the observed data [53].

In addition to its use in field and wind-tunnel experiments, LES has been found a useful technique to reproduce in detail many observed features of turbulent flow over homogeneous vegetation on flat terrain [54–58]. Cassiani *et al.* [49] applied an LES approach to the study of the effects of canopy leaf area index on airflow across forest edges. With increasing forest leaf area index (LAI – a measure of forest density), Cassiani *et al.* found that the mean flow properties change in two ways: a recirculation zone develops near the forest edge and into the clearing and another recirculation zone develops deep inside the forest canopy. They also found the frequency and size of intermittent motion increase with increasing LAI. However, there is a minor impact on this intermittent motion for LAI > 6. The study of Cassiani *et al.* agrees well with the RANS model calculations reported in Flesch and Wilson [59]. LES was also applied by Patton and Katul [60] to study the effect of LAI variation on second-order statistics of turbulent velocity and pressure induced over gentle hills covered with sparse and dense canopies. They found a recirculation zone for dense canopies (large LAI values, ~10) and no recirculation for sparse canopies (small LAI values, ~1) which is consistent with the theoretical study of Finnigan and Belcher [61] and the flume experiments done by Poggi and Katul [62].

The transport of scalars such as temperature, humidity and trace gases was studied by Kanani-Sühring and Raasch [63] in their first work in 2015 where they found enhanced scalar concentration and fluxes above a forest patch downstream of a clearing–forest transition. This study was further extended by Kanani-Sühring and Raasch [64] who found enhanced scalar concentrations and scalar fluxes in the forest lee for a wide range LAI values and wind speeds.

For dense forest, mean streamwise transport of scalars is responsible for local scalar enhancement, whereas for sparser forest, mean and turbulent transports are equally responsible for the accumulation of scalars. The strength of the recirculation flow in the lee side of the forest has been found in both LES [49] and experimental studies [59] to increase with forest density.

In Stage 1 of our project (2014–2016), we used FDS to understand how sub-canopy wind profile develops in forests of different leaf area density (LAD). It should be noted that LAI is the integral of LAD. We also investigated the effect of the depth of the forest.

To test the model, we plot the centreline velocity profiles at all  $x$ -locations within the canopy region, and compare them with the Harman and Finnigan [16] model (Figure 13). The Harman and Finnigan [16] model is a simpler (compared to LES) ordinary differential equation that uses LAI rather than LAD. The average velocity profile over the whole canopy, and the average velocity profile over the last 400 m of the canopy are also plotted for comparison. The average profile over the whole canopy shows a prominent trunk-space maximum (shown in Figure 13), which, as expected, is not captured by the simple model. However, the Harman and Finnigan [16] model compares qualitatively well inside the canopy with the average over the last 400 m of the canopy where the profile is most developed. There is a significant discrepancy in the profile above the canopy. In the above-canopy region, there is a growing internal boundary layer that does not fully develop and hence the model is poor in this region.

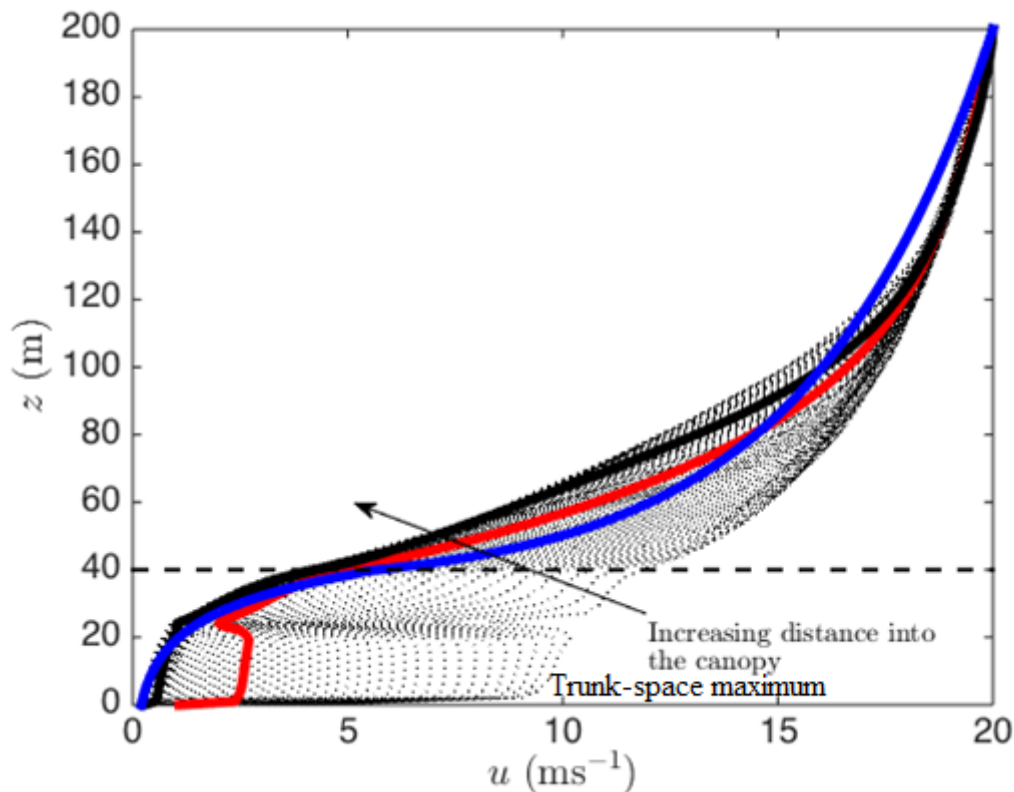


FIGURE 13: CENTRELINE VELOCITY PROFILES WITHIN THE CANOPY (BLACK DOTTED LINES). THE RED LINE IS THE AVERAGE OF ALL THE CENTRELINE VELOCITY PROFILES, THE BLACK SOLID LINE IS THE AVERAGE CENTRELINE VELOCITY IN THE MOST DEVELOPED PART OF THE CANOPY FLOW, AND THE BLUE LINE IS FROM THE MODEL OF HARMAN AND FINNIGAN [16]. THE THICK BLACK DASHED LINE INDICATES THE TOP OF THE CANOPY.

To compute a WRF from the Harman and Finnigan [16] model is straightforward. We adopt a  $p = 1/7$  power law to model the wind profile far from the canopy because it does not require estimation of roughness and displacement lengths like a logarithmic model. The relative wind speed (RWS) in the canopy is then

$$RWS(z) = \frac{u_r(z/z_r)^{\frac{1}{7}}}{\bar{u}_c} \quad (4)$$

where  $z_r$  is the reference height far above the canopy,  $z$  is a height within canopy,  $u_r$  is the observed wind velocity at  $z_r$  and  $\bar{u}_c$  is the sub-canopy wind velocity at  $z$ . In practice,  $u_r$  can be estimated from Numerical Weather Prediction (NWP) models, or from power-law, or logarithmic wind models (e.g. [65]). A range of WRFs can then be estimated by considering the inverse of this ratio. The model gives a range of WRFs, from  $\sim 2$  at the top of the canopy to WRF  $\sim 19$  at the bottom of the canopy. This is consistent with Moon *et al.* [15] who found the WRF varied between 2.3 and 14.4 across the canopies studied. The slight discrepancy may be due to the choice of  $p = 1/7$ . This value is chosen because it provides a good model of the wind speed over bare soil [66]. However,  $p$  varies depending on atmospheric stability and the nature of the surface [67] and a different choice of  $p$  may be appropriate to match the modelled WRF with the data of Moon *et al.* [15]. Therefore  $p$  should be considered a model parameter, along with LAI,  $u_r$  and  $z_r$ .

### Flow through canopies with non-uniform terrain

The study of wind flow over forested hills is of great interest for many applications, such as forest management, wind energy monitoring for potential location of wind turbines, forest-atmosphere scalar exchange of pollutant, pollen, greenhouse gases, energy or momentum and forest fire propagation [55]. Rough and hilly surfaces can change pressure fields significantly within the atmospheric boundary layer (ABL), which exerts a drag force on atmospheric flow [68].

Schematics of forested hills are shown in Figure 14. The pressure gradient induces a distortion of the mean flow and generates specific turbulent eddies in the flow field. The distorted mean flow and its perturbation can cause turbulent stresses to be affected, which can be calculated based on rapid distortion theory [69]. The flows on the upwind side and on the summit of the hill are divided into inner and outer layers respectively based on their interaction time scale between eddies. In the inner layer, the turbulence reaches local equilibrium, and the Reynolds stresses are larger and the time scale of interaction between eddies are higher compared with the outer layer. There are many interesting flow characteristic in the lee (downstream) side of the hill, such as a wake region development with a reduced wind speed, a strong elevated shear layer downstream of the summit and higher turbulence levels, and an intermittent separated region if the hill is sufficiently steep or the canopy is sufficiently dense [55]. Some of these were modelled using FDS and results are presented later in this report.

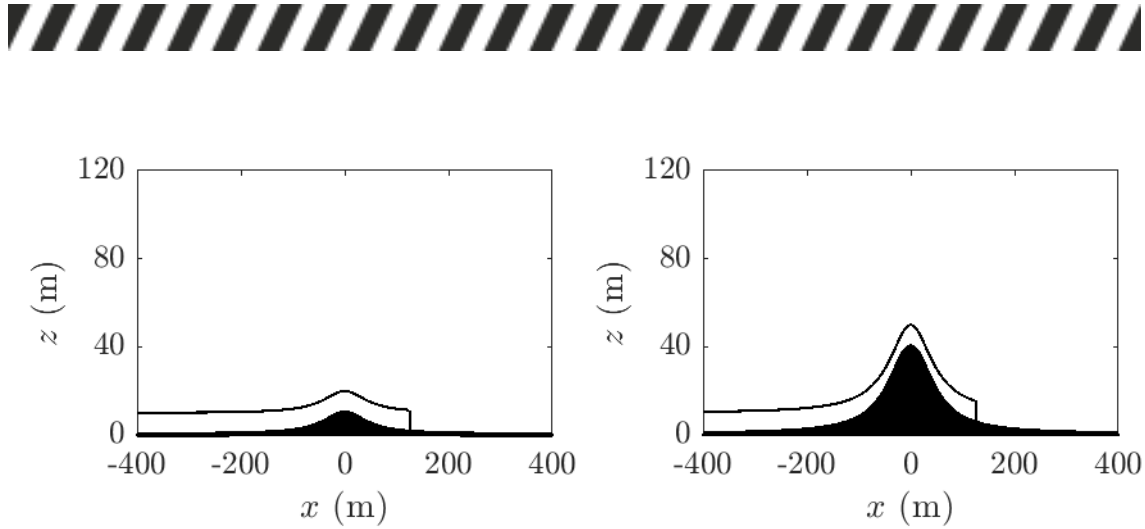


FIGURE 14: DOMAIN WITH SHALLOW HILL OF 10M HEIGHT (LEFT) AND HIGH HILL OF 40M (RIGHT) WITH 525M SPARSE AND DENSE CANOPY, RESPECTIVELY.

It is also important to note that the near-surface local wind speed may increase significantly owing to topographic features even in a low-lying topography, which may cause extreme weather such as cyclones and hurricanes [70]. Moreover, hills affect local wind direction, resulting in directional variation of the wind climate [71]. Jackson and Hunt [72] were some of the first to derive an analytical solution to describe flow over shallow hills and compared it successfully with wind-tunnel measurements and observations. They showed how the size and shape of a shallow hill and roughness affect wind speed and shear stress. Here, a hill is considered shallow when the hill is no more than 10 m high while a high hill is assumed to be more than 10 m high.

Later, similar numerical and theoretical studies were conducted by Bowen [73], Teunissen [74] and Hunt *et al.* [75], where the equations of motion were linearised [68] and asymptotic matching techniques were applied to the flow over hills. However, linear theories are inapplicable for the study of flow over steep hills. For these, numerical models are required using full non-linear equations to investigate the flow separation and other significant changes in flow characteristics [68]. Although the non-linear model of Hewer [76], which is based on Wood and Mason [77], predicts lee-slope wind speed better than linearised models, the model of Wood and Mason overestimates wind speed compared with the observed data.

To determine the critical slope of hills where flow separation occurs, Wood [78] studied two-dimensional and three-dimensional hills using a linear approach. Good agreement was achieved with other numerical and experimental results using this simple approach and the critical non-dimensional slopes for two-dimensional and three-dimensional hills were found to be 0.31 and 0.63, respectively. A similar study was conducted by Kim and Patel [79] for two-dimensional single and continuous hills with slopes of 0.3 and 0.5, where the authors concluded that flow separation was found at a slope of 0.5 for a single hill. Carpenter and Locke [80] conducted extensive wind-tunnel measurement over different hill geometries, including shallow sinusoidal, steep sinusoidal, consecutive and irregular hills.

In this study, we aimed to develop a physics-based LES model in FDS for flow through forested hills to identify hill- and canopy-induced perturbations and their



effect on flow fields. The details of flow fields are qualitatively compared with the literature to assess the applicability of FDS in such simulations. Our ultimate aim was to apply this model for more complicated cases where there is a possibility of firebrand transport and spotfire ignition due to recirculation.

## RESEARCH APPROACH

### Wind flow through horizontally heterogeneous canopies

A good understanding of the effect of heterogeneous canopies will extend our knowledge gained through previous WRF studies (in Stage 1, 2014–2016) in relation to homogeneous canopies and eventually improve fire spread prediction. A canopy region with some heterogeneity in the direction shown can be seen in the aerial photograph (Figure 15(a)) taken near Ararat in Victoria, Australia. Large-eddy simulation of a neutral atmospheric surface layer (ASL) flow was performed over a modelled tree canopy with heterogeneous LAD. The canopy is arranged as a series of equally sized stripes of different LAD, emulating the study of Bou-Zeid *et al.* [81] over heterogeneous rough surfaces, as shown in Figure 15(b).

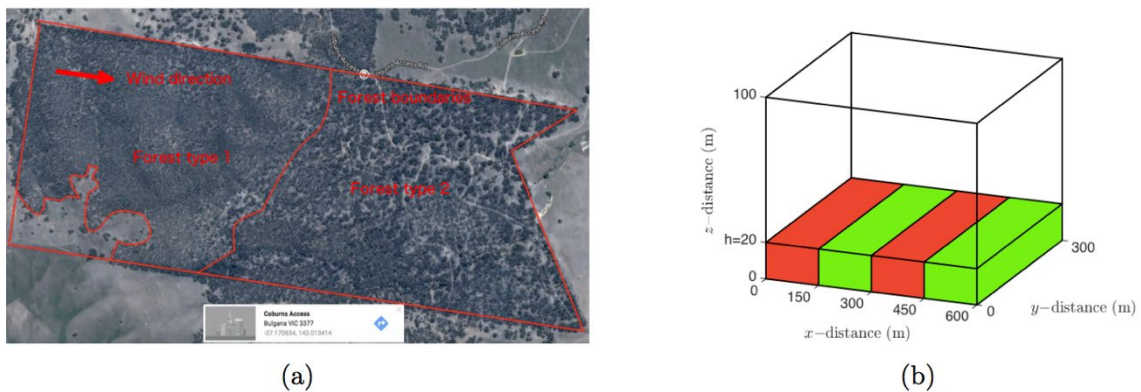


FIGURE 15: (A) AERIAL PHOTOGRAPH TAKEN NEAR ARARAT IN VICTORIA SHOWING A FOREST CANOPY WITH STEP-LIKE VARIATION IN LEAF AREA DENSITY BETWEEN FOREST TYPE 1 AND FOREST TYPE 2. THE WIND DIRECTION ALIGNED WITH THIS STEP CHANGE IN FOREST TYPE IS SHOWN BY THE ARROW. (B) SIMULATION DOMAIN FOR THE FOUR-CANOPY CASE. RED: LAD = 0.2, GREEN: LAD = 3. THE  $x$  AND  $y$  BOUNDARY CONDITIONS ARE PERIODIC.

The canopy height ( $h$ ) is chosen as 20 m. The overall domain size is  $600 \times 300 \times 300$  m ( $30h \times 15h \times 5h$ ). The boundary conditions employed follow Bou-Zeid *et al.* [81]. Different LAD variations are shown with colour schemes. The size of the exterior domain above the canopy height is chosen so that the largest relevant structures are captured. This study will allow, in the future, the identification of the equivalent roughness length, displacement length and blending height that parameterise the flow above a heterogeneous canopy. In the present work, we restrict our attention to the characterisation of the four-canopy case, the blending height and  $\beta$  parameter, which is the ratio of shear stress to the velocity at the canopy top. The general characteristics of the four-canopy case are representative of the other cases.

### Wind flow through vertically heterogeneous canopies

In nature, there is strong variation of LAD in all three spatial directions; the variation is most prominent in the vertical direction because trees typically have more vegetation at the top of the canopy than at the bottom. As shown in Figure



13, an analytic model exists for large, uniform canopies. That is, the occupied volume fraction, or LAD, of the canopy is constant over the whole canopy. The model of Inoue [82] is based on a balance between turbulent stresses and the drag force of the canopy. Harman and Finnigan [16] significantly extended the Inoue model to include above-canopy flow and non-neutral atmospheric conditions. Similarly to Inoue, their model assumes a very large forest, free of any forest edges or inhomogeneity in the forest canopy. The model has two empirical parameters that are straightforward to measure. It requires only the canopy top velocity and the LAI of the forest to predict the sub-canopy profile in neutral atmospheric conditions. However, no analytical solution exists for canopies where there is a variation in LAD in the vertical direction.

Recently, Moon *et al.* [15] performed field measurements of sub-canopy wind speeds in Australian vegetation. The measurements of LAD by Moon *et al.* and similar measurements made by Amiro [83] show considerable variability in the LAD profiles for different forest types around the world. Some of the measured profiles obtained by Moon are shown in Figure 16. These can be expressed with a mathematical expression (given below), which is shown with blue lines.

$$\text{LAD} = A \exp\left(-\frac{(z - \mu)^2}{\sigma^2}\right) + B \tag{5}$$

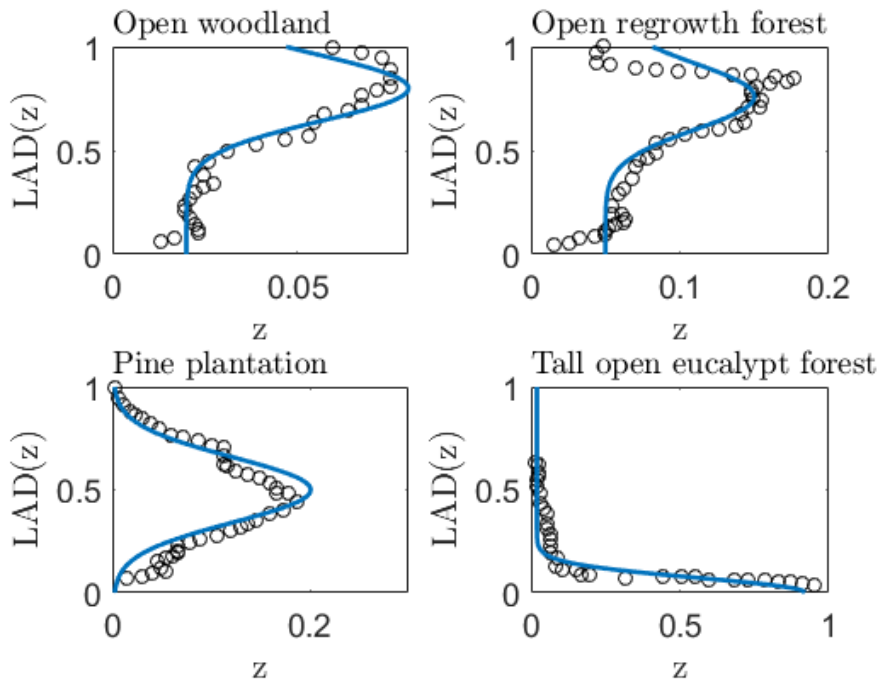


FIGURE 16: PROFILES OF LAD MEASURED BY MOON ET AL. [15] FOR FOUR DIFFERENT FOREST TYPES. BLUE LINES REPRESENT MATHEMATICAL EXPRESSIONS.

In Eqn (5), the LAD is assumed to be Gaussian with some specified geometric mean  $\mu$  and some variance  $\sigma$ . Physically,  $\mu$  corresponds to the height at which the canopy is most dense;  $\sigma$  roughly measures the width of the leafiest part of the tree crowns,  $z$  is the vertical height from the ground and  $A$  and  $B$  are model constants.



We intended to conduct LES simulation of a vertically heterogeneous canopy with the aim of developing a potential model for operational use. For the simulations, the height of the canopy is taken as  $h = 20$  m and  $h$  is a natural length scale of the flow. Some example profiles of LAD are shown in Figure 17. The profiles in Figure 17(a) were obtained by setting the variance  $\sigma^2$  (the width of the leafiest part of the tree crowns) to its minimum value and then varying  $\mu$ . The profiles in Figure 17(b) were obtained by setting  $\mu$  (the height at which the canopy is most dense) to its maximum value and varying  $\sigma^2$ . The solid black line is the same in both plots. The vertical dashed line in Figure 17(a) represents a fixed  $\sigma^2$  value and, similarly, the horizontal dashed line represents the  $\mu$  value in Figure 17(b). The red profile in Figure 17(a) is an exception as owing to setting a fixed  $\sigma^2$  at near ground, the profile took a skewed shape.

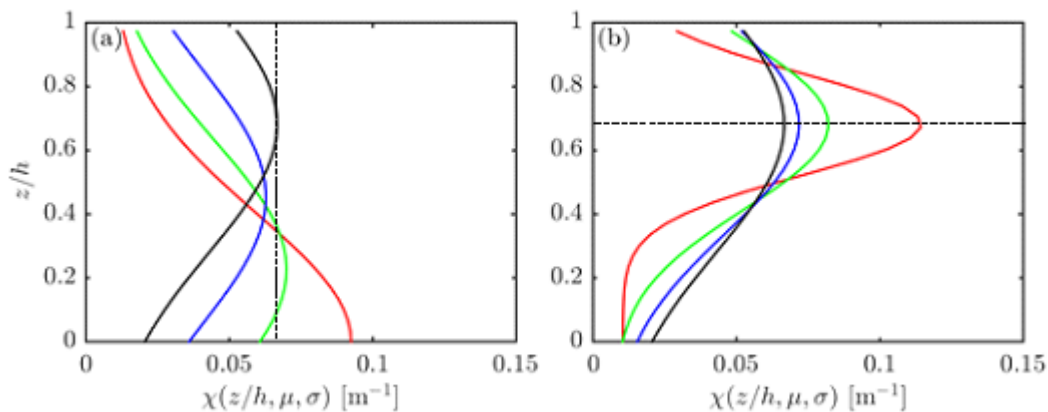


FIGURE 17: SAMPLE OF LAD PROFILES USED IN THIS STUDY. IN (A),  $\sigma^2 = 0.325$  IS HELD CONSTANT AND  $\mu = 0.00$  (RED), 0.233 (GREEN), 0.467 (BLUE), AND 0.700 (BLACK). IN (B),  $\mu = 0.70$  IS CONSTANT AND  $\sigma^2 = 0.325$  (BLACK – THE SAME CURVE AS IN (A)), 0.233 (BLUE), 0.142 (GREEN), AND 0.050 (RED).

### Flow through canopy over forested hills

This study seeks to identify how a hill disturbs the canopy recirculation region (see *Background* section). We choose two hill heights as shown in Figure 14. We choose two canopy LAIs (integral of LAD) as shown in Figure 18 to obtain both flow with no downstream recirculation and flow with downstream recirculation on flat ground. The canopy edge is considered to be at the bottom of the hill on the right side of the hill. Along with no-canopy and no-hill cases, there are eight cases in total, as shown in Table 4. The different parameters used in the simulation are shown in Table 4.

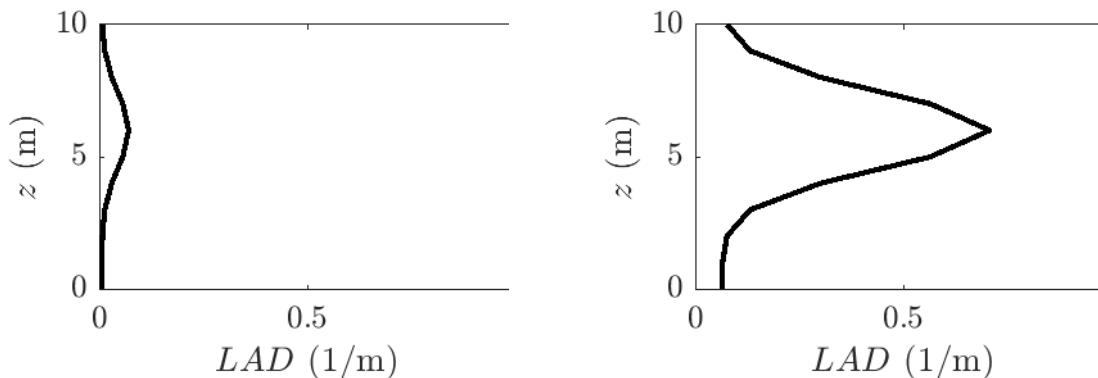




FIGURE 18: LAD PROFILE OF SPARSE (LEFT) CANOPY WITH LAI OF 1.0, AND DENSE (RIGHT) CANOPY WITH LAI OF 10.0'

TABLE 3: SIMULATED CASES FOR FLOW THROUGH CANOPY OVER FORESTED HILLS.

	Sparse canopy	Dense canopy	No canopy
Shallow hill (10 m)	LAI = 1	LAI = 10	Hill only
High hill (40 m)	LAI = 1	LAI = 10	Hill only
No hill	Canopy only, LAI = 1	Canopy only, LAI = 10	

TABLE 4: PARAMETERS USED IN THE SIMULATION FOR FLOW THROUGH CANOPY OVER FORESTED HILLS.

Parameter	Value
L_h (longitudinal length of the hill)	50 m
L_c (canopy cover length)	525 m
h_h (height of the shallow/high hill)	10 or 40 m
x_0 (centre of the hill)	0 m
$\mu$ (geometric mean)	0.85
$\sigma$ (variance)	0.3
B (constant)	0.02

The domain size is chosen following the work of Mason and Thomson [84] and Dupont *et al.* [55]. However, we use uniform mesh in the whole domain, whereas Dupont *et al.* used fine mesh for the hill part only. The high hill height is expected to be around 30–40 m and the low hill height around 10 m. Because we wish to study the effect of an isolated canopy edge, without interaction effects from other hills, periodic boundaries may be unsuitable in the streamwise direction. Therefore, we choose a longer domain of 800 m so the effect of the periodic interaction is negligible. We choose eight nested meshes with a domain size of 800 x 240 x 120 m with a grid resolution of 4 x 2 x 1 m.

## FINDINGS

### Wind flow through horizontally heterogeneous canopies

The results of the four-canopy case (sparse, dense, sparse, dense) are presented here. The vertical profiles of streamwise velocity averaged over time and lateral variation are shown at a range of locations along the four-canopy case in Figure 19(a). When the flow moves from a sparse canopy to a dense canopy, it slows in the streamwise direction, causing regions of strong upward vertical velocity above the dense canopies (see Figure 19(b)). Correspondingly, there is a strong downward vertical velocity above the sparse canopies. This means vertical velocity couplets exist on the vertical interface between two canopies. This implies the presence of sub-canopy recirculation zones at canopy interfaces, which can be confirmed by visualisation of the fluid streamlines.



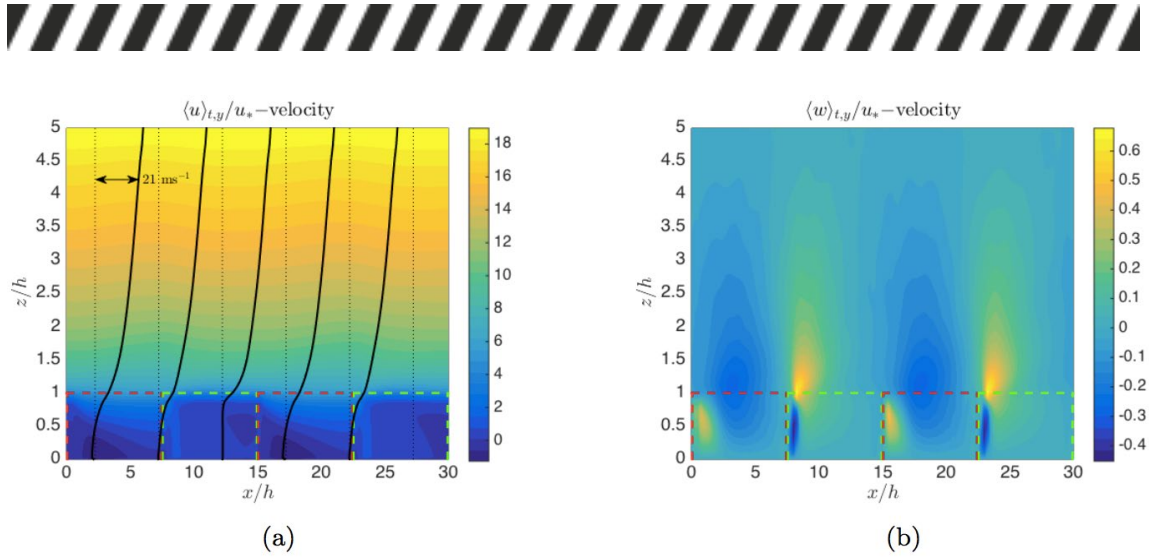


FIGURE 19: CONTOURS OF NON-DIMENSIONAL AVERAGE  $U$  VELOCITY WITH SUPERIMPOSED PROFILES OF AVERAGE  $U$  VELOCITY AT A RANGE OF LOCATIONS ALONG THE CANOPY. NOTE THE CONTOURS (COLOURS) ARE NON-DIMENSIONAL BUT THE PROFILES HAVE AN APPROXIMATE DIMENSIONAL SCALE AS INDICATED. (B) VERTICAL VELOCITY IN THE WHOLE DOMAIN SHOWING THE STRONG UPDRAFTS (YELLOW) AND DOWDRAFTS (BLUE) ABOVE AND WITHIN THE CANOPIES. THE CANOPY STRIPES ARE SHOWN AS DOTTED OUTLINES.

The recirculation regions are visualised by plotting the streamlines of the mean flow in Figure 20(a) over each individual stripe of canopy that affects the downstream flow. The plumes, mixed layer and blending height above the canopy can then be visualised as shown in Figure 20(b). The critical height where this well-mixed layer commences is called the blending height. In a blended layer, there will be no localised deviations from the mean flow throughout the domain. Above the canopy, internal boundary layers form over each canopy stripe and exhibit similar features to the characteristic upstream plumes of flow over a rough surface.

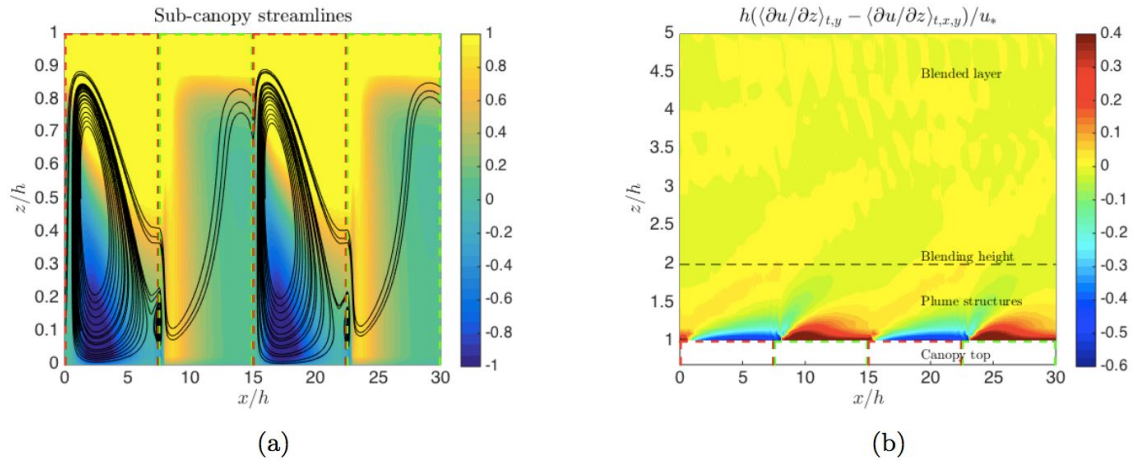


FIGURE 20: (A) STREAMLINES HIGHLIGHTING TWO RECIRCULATION VORTICES WITHIN THE CANOPY, SUPERIMPOSED ON THE NON-DIMENSIONAL AVERAGE  $U$  VELOCITY. (B) CONTOURS OF AVERAGED VELOCITY GRADIENT DIFFERENCE ABOVE THE CANOPY, CLEARLY SHOWING THE PLUME STRUCTURE IMMEDIATELY ABOVE THE CANOPY. ABOVE THE BLENDING HEIGHT IS A WELL-MIXED BOUNDARY LAYER CHARACTERISED BY NEGLIGIBLE FLUCTUATIONS IN THE VELOCITY GRADIENTS. THE CANOPY STRIPES ARE SHOWN AS DOTTED OUTLINES.

A homogeneous sub-canopy flow is parameterised by  $\beta = u_*/u_h$ , the ratio of canopy top friction velocity to canopy top velocity (Harman and Finnigan [16]). In that study,  $\beta$  was found to be approximately constant with LAD in neutral atmospheric stability conditions; the value proposed for neutral conditions is  $\beta = 0.3$ . In Figure 21,  $\beta$  as a function of  $x/h$  is plotted for all canopy cases. We also find that the mean value of  $\beta$  is approximately constant across the heterogeneous canopies, with a value of  $\beta \approx 0.2$ , as observed in Figure 21.

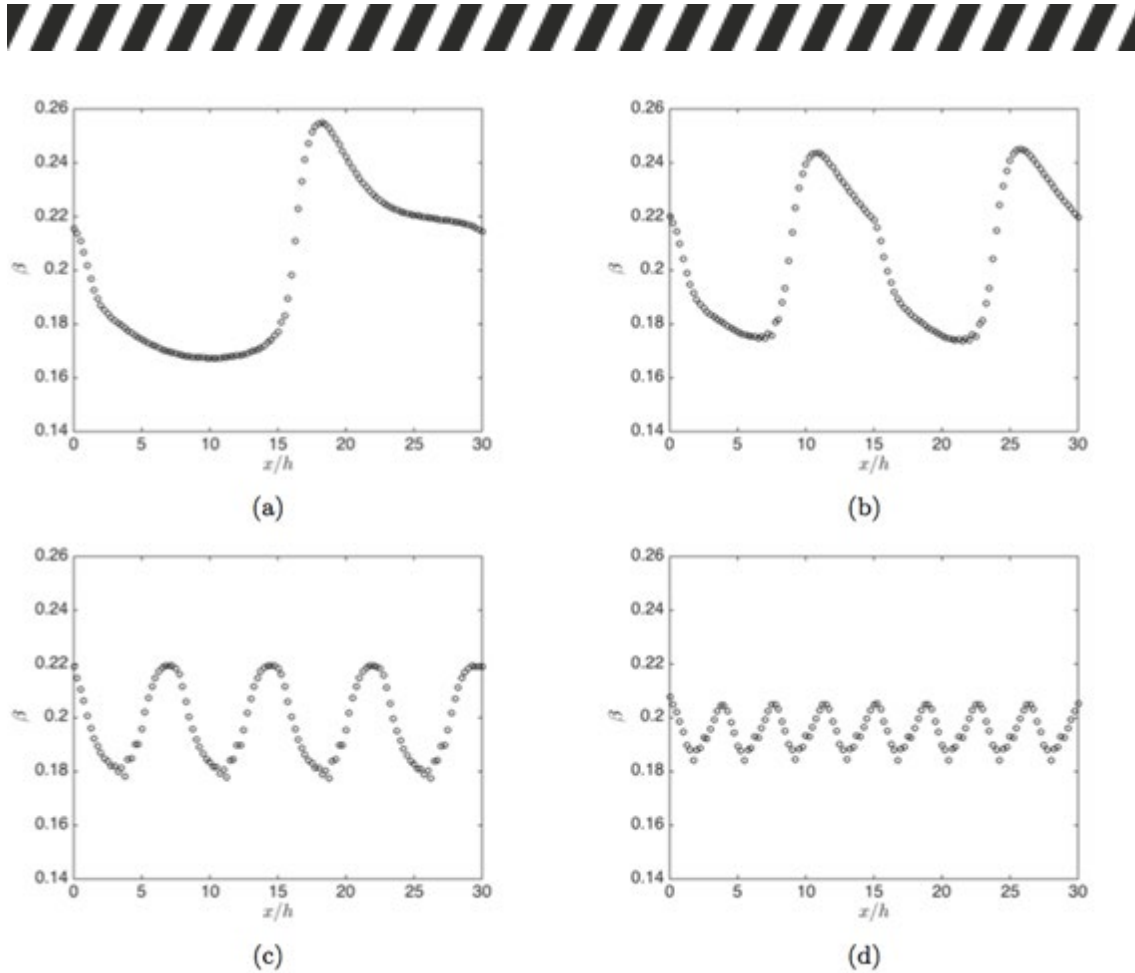


FIGURE 21: VARIATION OF THE PARAMETER  $\beta$  FOR (A) TWO, (B) FOUR, (C) EIGHT, AND (D) SIXTEEN CANOPY CASES. THE MEAN VALUE IS APPROXIMATELY  $\beta = 0.2$  IN ALL CASES.

Further work is required to investigate the dependence of  $\beta$  on the canopy LAD. It is not possible to immediately extend the sub-canopy flow model of Harman and Finnigan [16] (shown in Figure 13) because the recirculation regions that exist at the canopy interfaces will not be captured. The data set presented here will be used to develop a parameterisation of the boundary layer above a heterogeneous tree canopy and it will also be used to model the sub-canopy flow. The determination of an equivalent blending height, displacement length and surface roughness length in terms of the canopy parameters can be used in surface schemes of numerical weather prediction models, which will improve overall wind forecast accuracy.

The development of a reduced model of sub-canopy winds in heterogeneous forests will be useful to wildfire management agencies that require estimates of sub-canopy wind speeds for operational fire models such as the McArthur model or the Rothermel model [85]. Extending this work will contribute to understanding the effect of forest heterogeneities on firebrand and smoke transport.

### Wind flow through vertically heterogeneous canopies

The simulation results of flow through vertically varied canopies given in Figure 17 are presented here. The simulated mean wind profiles are shown in Figure 22, where the dashed lines represent canopy heights. The profiles are all normalised by the value of the wind speed at the top of the canopy at  $z/h = 1$ . The pressure gradient and LAI are held constant during these simulations. The variation of the



LAD profile leads to variation in the drag force exerted by the canopy upon the air flow.

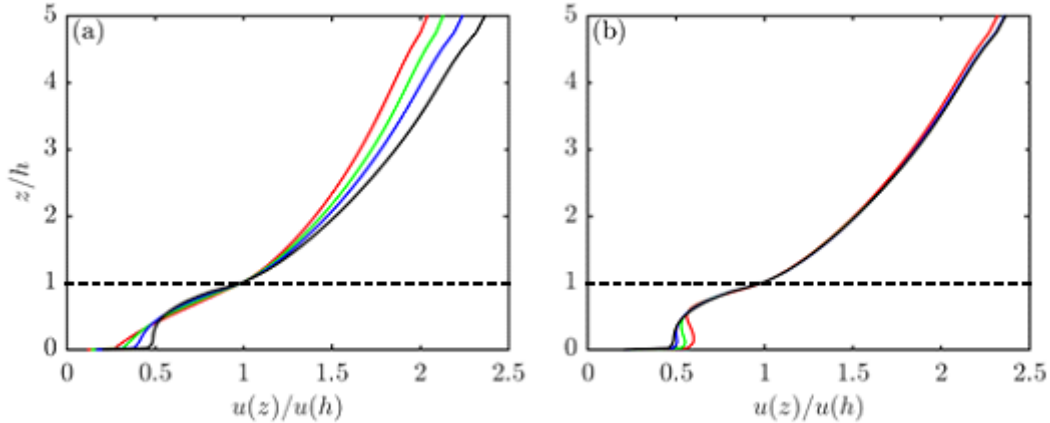


FIGURE 22: MEAN  $U$  VELOCITY PROFILES NORMALISED BY THE CANOPY TOP VALUE. THE CANOPY LAD PROFILES ARE THE SAME AS SHOWN IN FIGURE 17, THAT IS, IN (A)  $\sigma^2 = 0.325$  IS HELD CONSTANT AND  $\mu = 0.00$  (RED), 0.233 (GREEN), 0.467 (BLUE), AND 0.700 (BLACK). IN (B)  $\mu = 0.70$  IS CONSTANT AND  $\sigma^2 = 0.325$  (BLACK – THE SAME CURVE AS IN (A)), 0.233 (BLUE), 0.142 (GREEN), AND 0.050 (RED).

Because the LAD profile is known and the average sub-canopy wind velocity is simulated, the LAD profile that gives the maximum drag force can be measured. In these simulations, the canopy that exerts maximum drag force is  $\mu = 0.7$ ,  $\sigma^2 = 0.233$ . That is the profile with maximum mean and variance. As mentioned earlier,  $\mu$  corresponds to the height at which the canopy is most dense and  $\sigma$  roughly measures the width of the leafiest part of the tree crowns.

### Potential model development for operational use

Inoue [82] developed a momentum-balance model to determine the sub-canopy wind profiles deep within a canopy. Harman and Finnigan [16] extended Inoue's original model to blend smoothly with a roughness sub-layer and logarithmic layer above the canopy (a profile presented in Figure 13) and incorporate the effects of atmospheric stability. The discussion here will follow Harman and Finnigan. The Navier–Stokes equations may be averaged in time and in space for a LAD that is constant in the  $x$ ,  $y$  and  $z$  directions. For convenience, the canopy top is located at  $z = 0$ . At the end of the derivation, we will apply a coordinate transform to recover the canopy top at  $z = h$ . The canopy is thought of as infinitely deep.

The averaging process removes the time derivative and the advection terms from the Navier–Stokes equations. The pressure gradient term is also assumed to be negligible relative to the turbulent stress term ( $\tau_{x,z}$ ) and the drag term ( $F_{D,x}$ ). The momentum balance is then

$$\frac{\partial \tau_{x,z}}{\partial z} + F_{D,x} = 0, \tag{6}$$

where we have written the coordinates explicitly instead of  $i, j, k$ . The turbulent stress term may then be modelled using the mixing length approximation. The drag term is modelled as before; however, we assume that the canopy has a uniform LAI. This gives the following ordinary differential equation:



$$\frac{\partial}{\partial z} l^2 \frac{\partial}{\partial z} u + c_d \text{LAI} u^2 = 0, \quad (7)$$

where  $c_d$  is the drag coefficient. Boundary conditions are that the velocity derivative vanishes as  $z \rightarrow \infty$  and the canopy top velocity  $U_h$  is known. The equation has a solution:

$$u = U_h \exp\left(\frac{\beta z}{l}\right), \quad (8)$$

Scaling arguments that depend on a constant profile show that the mixing length is  $l = 2\beta^3/c_d \text{LAI}$ . Harman and Finnigan [16] showed that the exponential profile agrees sufficiently well with observed subcanopy profiles. The most commonly violated assumption of the Inoue model is the canopy has finite depth. In practical terms, the Inoue model works for the top part of the canopy and its predictions become poorer near the ground. In these simulations, there is the presence of a driving pressure gradient and LAD is not constant in the  $z$  direction. Hence, we expect that Inoue's model [82] will give poor agreement through the canopy.

The resulting sub-canopy model is tested by comparing the simulated sub-canopy velocity profiles with the modelled profiles using firstly the simulated values of  $\beta$  (the ratio of shear stress to  $u$  velocity at the canopy top) and the value  $\beta = 0.3$  observed by Harman and Finnigan [16]. The comparison between the simulated and modelled profiles is shown in Figure 23(a) and (b). The modelled profiles with the simulated value of  $\beta$  do not agree well with the simulated profiles. However, using the value of  $\beta = 0.3$  observed by Harman and Finnigan improves the agreement in the top half of the canopy. Nonetheless,  $\beta$  must be considered a parameter of the model rather than some universal constant.

To reduce the discrepancy between the modelled and simulated profiles, we attempt to address the assumption of a constant LAD profile. Because the displacement length is the only quantity that varies significantly with the canopy parameters, it is hypothesised that  $d$  (the displacement height of the canopy) is a more relevant length scale than the constant canopy height  $h$ . Therefore, we define the displacement length LAI,  $d\text{LAI}$  as

$$d\text{LAI} = \int_0^d A \exp\left(-\frac{(z - \mu)^2}{\sigma^2}\right) + B dz, \quad (9)$$

that is, the leaf area index computed from  $z = 0$  to  $z = d$  instead of  $z = h$ . Then  $d\text{LAI}$  is used in place of LAI in the Inoue model. The modified model predictions using the simulated values of  $\beta$  are compared with the simulated profiles in Figure 23(c) and (d). Agreement between the modelled and simulated profiles in the top half of the canopy is significant but far from perfect. The modelled profiles do not agree with the simulated ones in the bottom half of the canopy and further work is required to improve the Inoue model in the near-ground region.

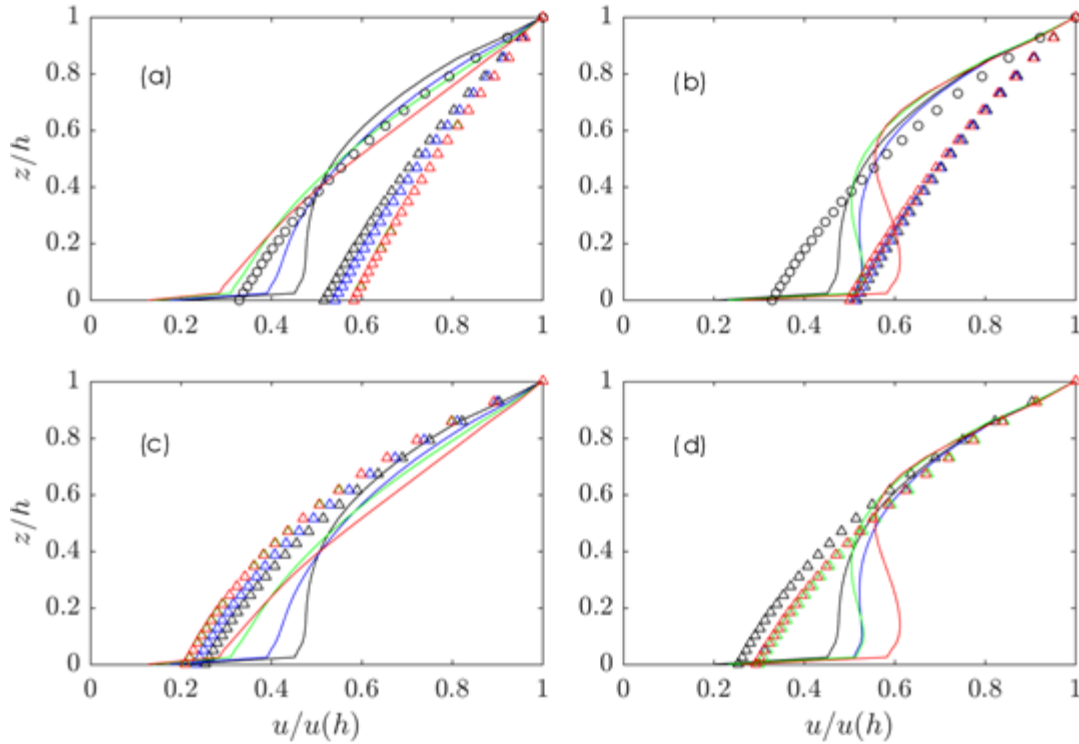
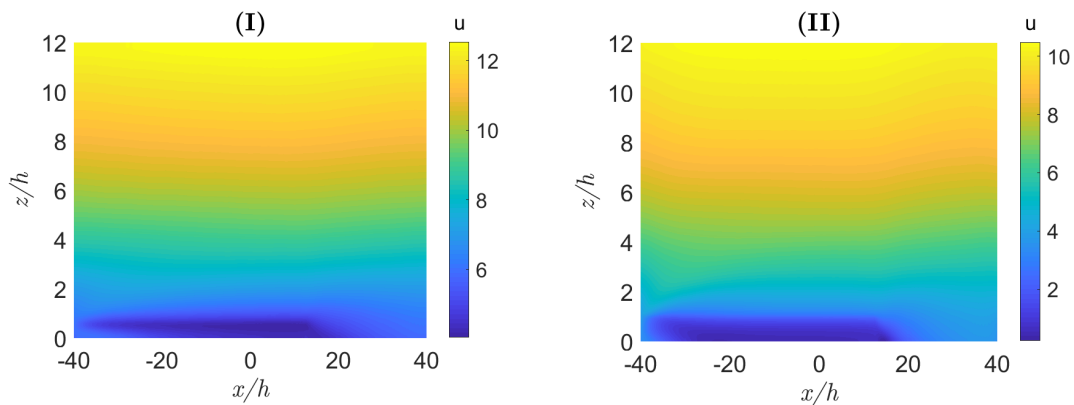


FIGURE 23: MODELLED AND SIMULATED SUB-CANOPY  $u$  VELOCITY PROFILES. (A) AND (B) CONTAIN THE MODELLED PROFILES USING THE SIMULATED  $\beta$  (TRIANGLES) AND THE OBSERVED  $\beta$  (CIRCLES) OF HARMAN AND FINNIGAN [16] AND A CONSTANT MIXING LENGTH BASED ON LAI. THE MODELLED PROFILES IN (C) AND (D) USE THE SIMULATED  $\beta$  AND  $dLAI$ . THE CANOPY LAD PROFILES ARE THE SAME AS SHOWN IN FIGURE 17. THAT IS, IN (A)  $\sigma^2 = 0.325$  IS HELD CONSTANT AND  $\mu = 0.00$  (RED), 0.233 (GREEN), 0.467 (BLUE), AND 0.700 (BLACK). IN (B)  $\mu = 0.70$  IS CONSTANT AND  $\sigma^2 = 0.325$  (BLACK – THE SAME CURVE AS IN (A)), 0.233 (BLUE), 0.142 (GREEN), AND 0.050 (RED). (C) AND (D) ARE THE SAME CURVES AS (A) AND (B) RESPECTIVELY.

It is anticipated that a model of sub-canopy flow and a parameterisation of the above-canopy flow will be developed from the results of these simulations.

### Flow through canopies with non-uniform terrain

Large eddy simulation (LES) is performed to study the flow characteristics of the atmospheric boundary layer over forested hills. The sparse and dense canopies are introduced in the hill structure and modelled by homogeneous LAD. A pressure-driven flow is established under neutrally stratified conditions to explore the effect of hill- and canopy-induced perturbations including velocity speed-up, separation, attachment and recirculation.



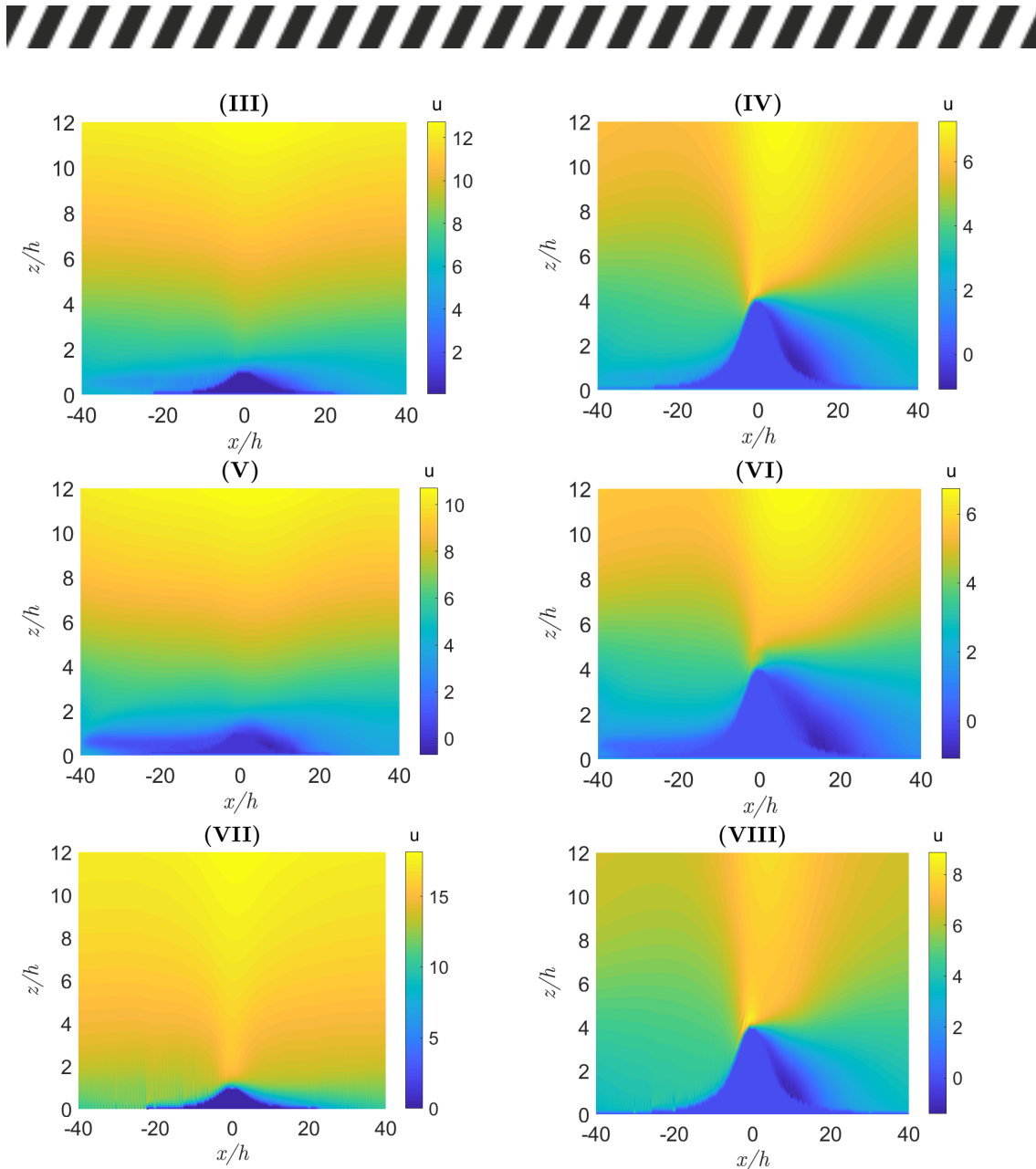


FIGURE 24: CONTOUR PLOT OF MEAN VELOCITY PROFILE WITH VARYING LAI DENSITIES AND HILL HEIGHTS AS FOLLOWS: (I) SPARSE CANOPY WITHOUT HILL; (II) DENSE CANOPY WITHOUT HILL; (III) SPARSE CANOPY WITH SHALLOW HILL; (IV) SPARSE CANOPY WITH HIGH HILL; (V) DENSE CANOPY WITH SHALLOW HILL; (VI) DENSE CANOPY WITH HIGH HILL; (VII) SHALLOW HILL WITHOUT CANOPY; AND (VIII) HIGH HILL WITHOUT CANOPY.

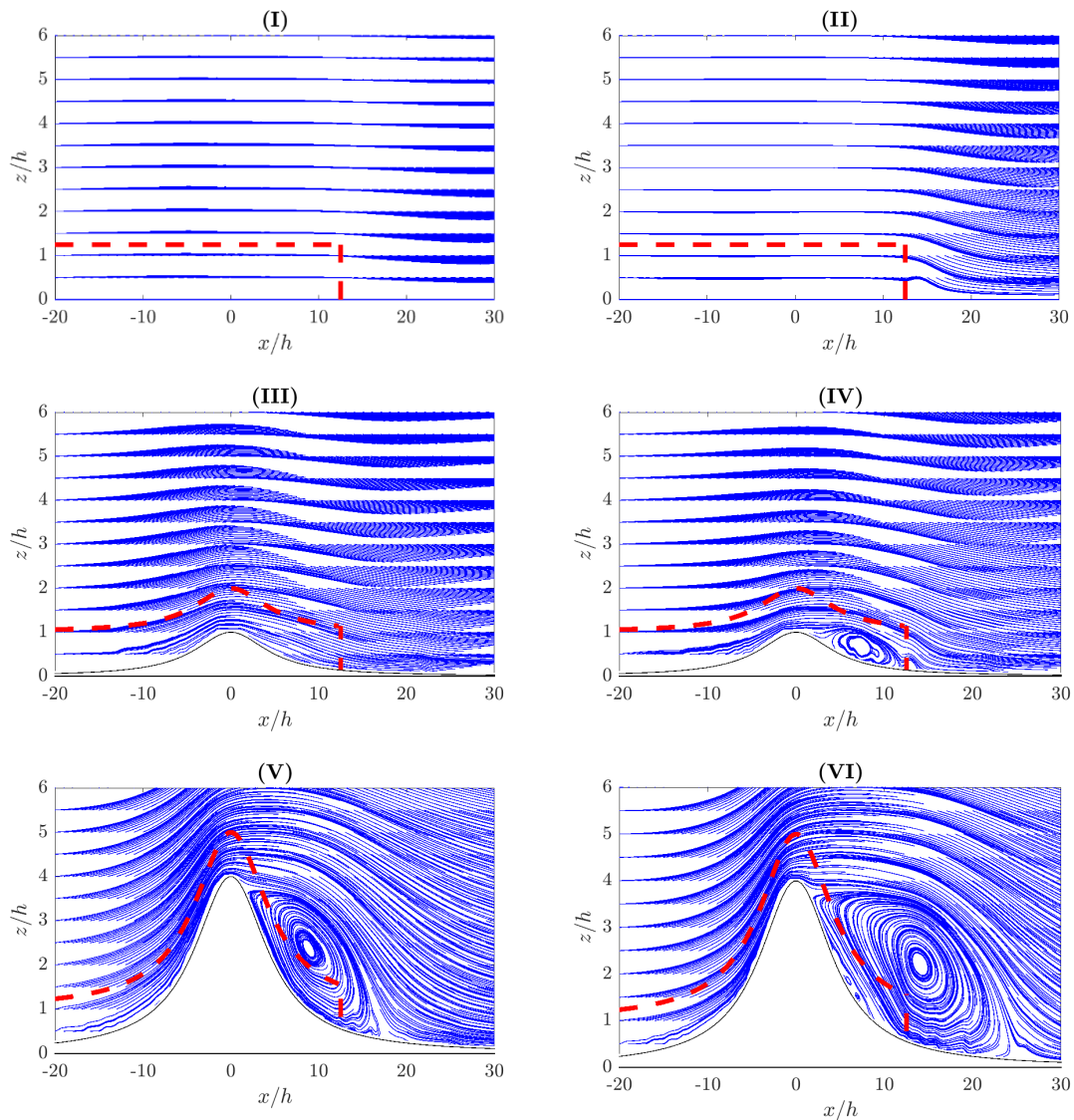
The contour plot of streamwise mean velocity is shown by colour shading for each case in Figure 24, which shows the variation of flow characteristics with respect to vegetation densities and hill steepness. The first two cases (I and II) are simulated with sparse and dense canopies respectively without a hill structure, and clearly show canopy sub-layer (deep blue) followed by inner, middle and outer canopy layers; these are qualitatively similar to the schematic diagrams of Patton and Katul [60]. The two sparse canopy cases, III and IV, with the inclusion of a shallow and high hill respectively, show significant differences in mean velocity profiles. The velocity difference is due to the hill-induced perturbation.

Moreover, the mean velocity at the top of the high hill is increasing. Higher velocity is observed above the high hill compared with the shallow hill. The lee side of the high hill clearly shows extended regions of lower velocity, where recirculation or separation can occur. For the dense canopy cases (V and VI), there are similar effects for the shallow and high hill cases, with further enhancement of velocity and the expansion of separation regions in the lee side



of the high hill. Cases VII and VIII are set up with only the hill structure without vegetation: the velocity results show a different flow. The effect of the hill-induced flow structure (Cases VII and VIII) is clearly pronounced compared to the cases without a hill structure (see Cases I and II).

The streamlines of mean velocity are shown in Figure 25, which show distinctive features for both LAI densities and size of the hill structure. The streamlines of the first two cases are based on sparse and dense vegetation respectively over flat ground, and clearly show some effect of flow distortion on the canopy edges in the sparse case. However, the dense canopy case shows more distortion than the sparse case. The modification of flow structure is more noticeable with sparse and dense canopy cases with inclusion of shallow and high hill structures respectively (Cases III–VI). The recirculation, flow separation and attachment are very clear in these cases except for the sparse case with a shallow hill, which does not show recirculation. Recirculation is also found in the high hill case without canopy (Case VIII), although the shallow hill case does not show any recirculation, which is similar to the sparse canopy with shallow hill case.



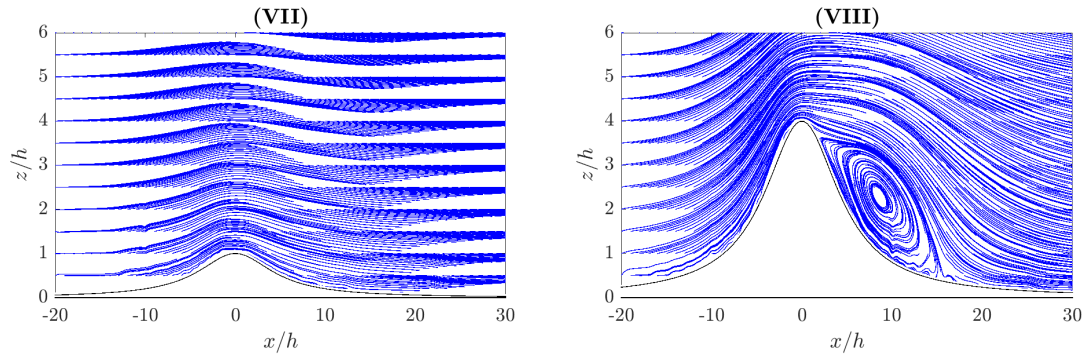


FIGURE 25: STREAMLINES HIGHLIGHTING RECIRCULATION VORTICES SUPERIMPOSED WITH FIRST MOMENT OF STREAMWISE VELOCITY. THE RED DOTTED LINE SHOWS THE CANOPY TOP OUTLINE. (I) SPARSE CANOPY WITHOUT HILL; (II) DENSE CANOPY WITHOUT HILL; (III) SPARSE CANOPY WITH SHALLOW HILL; (IV) SPARSE CANOPY WITH HIGH HILL; (V) DENSE CANOPY WITH SHALLOW HILL; (VI) DENSE CANOPY WITH HIGH HILL; (VII) SHALLOW HILL WITHOUT CANOPY; AND (VIII) HIGH HILL WITHOUT CANOPY.



## GRASS AND FOREST FIRE MODELLING

### BACKGROUND

Fire propagation studies are important to estimate ROS and the science behind ROS dependence on various topographical, weather and fuel factors, such as wind speed, atmospheric conditions, fuel type, fuel height, density, moisture content and slope of terrain. Considering fuel type, almost 70% of Australia is covered by grassland. Similarly, grassland covers a significant landmass in wildland-prone countries. There have been a considerable number of experimental studies to develop ROS models as a function of weather (wind speed, temperature, humidity) and fuel (mass, moisture content, curing) parameters. In the last decade and a half, physics-based modelling of grassfire propagation has received momentum.

From our Stage 1 (2014–2016) study, Moinuddin *et al.* [2] using WFDS presented domain and grid-converged results of grassfire propagation on a 100 x 100-m plot validated against Australian grassland experiment C064 of Cheney *et al.* [86]. Such rigorous numerical studies are rare as pointed out by Cruz *et al.* [87], who credited Moinuddin *et al.* for overcoming the issue of grid size dependence in physics-based modelling. In Figure 26, the simulated ROS of the head fire as a function of  $U_{10}$  values is presented (see details in [2]) and compared with operational models while the experimental observations obtained by Cheney *et al.* [86] are shown in the background.

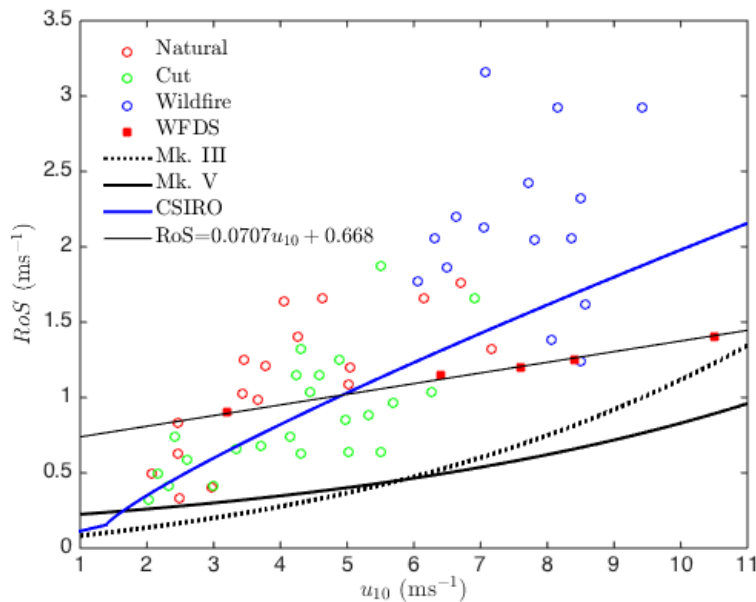


FIGURE 26: RATE OF SPREAD VS 10-M OPEN WIND SPEED FOR A SIMULATED GRASSLAND, COMPARED WITH OPERATIONAL MODELS AND EXPERIMENTAL RESULTS OBTAINED BY CHENEY *ET AL.* [86] IN THE BACKGROUND.

It was our intention to compare simulated ROS with experimental observations in order to judge the faithfulness to reality of the physics-based models, and to compare physics-based modelling of ROS with predictions of ROS from operational models with the same parameters. The experimental grass fires of Cheney *et al.* [86] were conducted under a range of fuel and ambient weather conditions. ‘Natural’ grass refers to undisturbed or ungrazed pasture land, ‘cut’ grass to mowed (and likely removed) or grazed pasture lands including crop

stubble, and 'wildfire' refers to a set of 20 major grassland fires in south-eastern Australian from 1965 to 1990. The CSIRO model is derived from this experimental dataset, whereas the two McArthur models, MK3 and MK5, are derived from a dataset of lower wind speed range. The CSIRO model [88] is therefore expected to be a good fit for this dataset.

The WFDS simulations predict significantly higher ROS at 3 m/s wind speed than the CSIRO and McArthur MK3 and MK5 models; however, the simulated ROS is realistic when compared with the experimental fires of Cheney *et al.* [86]. At the higher limit of wind speed, above  $U_{10}$  of 6 m/s, the WFDS simulation predicts a significantly lower ROS than the CSIRO model, but higher than both McArthur models. The discrepancy at higher velocities may be due to the effect of fireline size, which was not investigated here. The experimental observations are ROS from wildland fires rather than experimental fires, where the fireline size is not controlled.

Moinuddin *et al.* [2] showed that when driving wind velocity is kept constant and the grass height is varied (keeping the bulk density constant), the ROS initially increases as the grass height is increased (wind-driven mode) and then, with a further increase in grass height, fire size increases and flames becomes vertical. The propagation enters plume-driven mode and with increased grass height, the fire becomes larger and more vertical. In this mode, the ROS decreases with increased grass height. However, the dependence of ROS on grass height is a matter of debate. Anecdotal evidence from fire agencies suggests that if the grass height is higher, the ROS of the head fire is larger. Recent experiments conducted in Victoria, Australia [89], suggest that ROS does not depend on grass height. Observations from gamba grass fires in the Northern Territory of Australia reported by fire agencies suggest that there may be some dependence of ROS on grass height (S. Heemstra, pers. comm. 2016). It is important to note several points about these observations. First, the fuel types and conditions that led to these anecdotal observations are quite varied. Second, invasive species like gamba often grow to a much greater height than the native grasslands of south-eastern Australia, and therefore height is much more likely to influence fire behaviour as the tall or high grass may act like a forest canopy.

### Effect of relative humidity on grassfire propagation

Relative humidity of air is considered to have a significant effect on the ROS of grassfire propagation. Sharples *et al.* [90] in their simple index model propose using only temperature, wind speed and relative humidity to predict Fire Danger Index (FDI). The argument is one of model parsimony. That is, many of the other empirical models use too many parameters, and parameters that may be deduced from other models and may have only small effects on the predicted FDI. Ambient temperature ( $T$ ), relative humidity ( $RH$ ) and curing ( $c$ ) are a proxy for fuel moisture. For Grassfire Fire Danger Index (GFDI) MK-III and MK-V [91], fuel moisture content ( $MC$ ) is determined as:

$$MC = \frac{97.7 + 4.06RH}{T + 6} - 0.00854RH + \frac{3000}{C} - 30 \quad (10)$$

In this stage of the project (2017-2020), we aimed to investigate the effect of relative humidity and fuel moisture content on the ROS.

## Grassfire propagation on sloping terrain

Grasslands are often found on terrains with slope. This topographic feature can increase or decrease the rate of fire spread depending on whether the fire encounters a slope upward or downward. For slope, McArthur [14, 92] proposed a rule of thumb that for every 10° of positive slope, the rate of fire spread approximately doubles, or it halves with every 10° of negative slope. Noble *et al.* [91] presented a set of equations for McArthur's grassland fire danger meter as well as for slope correction factors. This correction factor is incorporated in Australian Standard AS3959 [93] as the following equations:

$$R_{slope} \quad (11)$$

$$= R e^{(0.069 slope)} \quad \text{when fires burning uphill (effective downslope)}$$

$$R_{slope} \quad (12)$$

$$= R e^{(-0.069 slope)} \quad \text{when fires burning downhill (effective upslope)}$$

$R$  is the forward ROS (km/h),  $R_{slope}$  is  $R$  corrected for slope and slope is the effective slope in degrees. The correction (Eqns (11), (12)) is considered valid up to  $\pm 20^\circ$  slope [92]. Sharples [14, 92] pointed out that McArthur might not have advocated the use of Eqn (11), which may have been adopted out of a combination of loose reasoning and convenience. Sullivan *et al.* [94] examined fire spread on negative slopes based on several laboratory experiments and showed that significant under-prediction can occur using Eqn (11). For a slope of  $-20^\circ$ , underprediction was by a factor of three. Sullivan *et al.* argued that the value of  $R$  for the negative slope situation should never be less than 60% that of the zero-slope condition. They also questioned the basis for McArthur's rule of thumb as it is only described as the result of 'experimental fire studies' in [14] and showed that for upslope, it significantly over-estimated  $R_{slope}$  compared with the US operational model BEHAVE (based on Rothermel [85]).

Dold and Zinoviev [95] carried out simple mathematical modelling and experimental-based studies (laboratory scale for straw and field scale for forest) to determine under which conditions a fire plume attaches to a surface for line fire ignition. The laboratory scale experiments showed that fire plume attachment occurred when the fire was on a  $30^\circ$  and  $35^\circ$  upslope. Fire plume attachment was also observed when a field-scale test of forest fire was conducted  $23^\circ$  upslope. All tests were carried out under mild or negligible wind conditions. Sharples [92] conducted two-dimensional physics-based modelling of convective plumes (in a tunnel setting) to identify the angle at which fire plume attachment occurs and found that for slopes  $\geq 26^\circ$ , such behaviour occurs.

Dold and Zinoviev [95] also showed that a fire spreading upslope causes the tilting and lengthening of flames, which directly induces an increase in the ROS. This supports that the increase in  $R$  is due to the increase in radiative and convective heat transfer as the flames get closer to the fuel.

However, Burrows [96] found that his experimental results on uniform jarrah litter fuels under zero wind conditions roughly matched Eqns (11), (12) in the range of  $\pm 15^\circ$ . Weise and Biging [97] found the opposite in their laboratory experiments using a tilting wind tunnel (in the range of  $\pm 30\%$  slope). Their fuel beds were



composed of vertical paper birch (*Betula papyrifera*) sticks and a shallow layer (<0.5 cm) of evenly distributed coarse aspen (*Populus tremuloides*) excelsior (wood wool). They found that the agreement between their observed  $R$  and that predicted by the McArthur model was poor, but good with Rothermel's [85]. Dupuy [98] also conducted a set of laboratory experiments using pine needles as a fuel bed with a range of  $\pm 30^\circ$  slope, with different fuel loads and two different species. Dupuy found that  $R$  varied both in relation to fuel load and species, especially in steep upslope cases. It was also observed that, when slope and fuel load exceeded certain limits, upslope fires were unsteady, and their flames were three-dimensional (3D).

Dupuy and Maréchal [99] studied the effect of slope in increasing the radiant heat flux load and using convective heat flux to pre-heat forest litter ahead of the fire front in lab-scale conditions. They studied fire propagation on slopes of  $0^\circ$ ,  $10^\circ$ ,  $20^\circ$  and  $30^\circ$ . They found that radiative heat transfer dominated the heat transfer mechanism up to  $20^\circ$ ; however, close to the fire line, convective heating was also significant. They also found that between  $20^\circ$  and  $30^\circ$ ,  $R$  increased by  $2.5\times$  owing to a significant increase in convective heating, when there was no increase of radiative heating.

From the above, it appears that the notion of obtaining quasi-equilibrium ROS for flat surface as a function of wind and then adding a slope correction may not be accurate. Empirical models are computationally cheap to implement and require only few parameters, which makes them user-friendly. However, these models are only truly valid in the range of conditions in which these were developed (often in benign conditions) and are highly dependent on the conditions in which the source data was obtained for model development. Most of the experimental studies found in the literature are at laboratory scale. Furthermore, the effect of slope on ROS, especially the fire plume attachment, is not well understood and operational (empirical) models may not be inclusive of many physical behaviours involved.

Therefore, in this stage of the project (2017–2020), we used rigorous physics-based modelling to investigate the effect of upslope on grassfire behaviour. First, we ensure the result is domain-independent and the atmospheric boundary layer is properly established before a fireline is ignited. We then seek to answer:

- What effect does slope have on  $R$  and how does that compare with operational models used in Australia?
- What are the underlying physical mechanisms that govern changes in  $R$  as the slope increases?
- What are the physical and parametric observations as the slope increases?

### Physics-based simulations of flow and fire development downstream of a canopy

Although there is debate on whether climate change or forest management is the more important contributing factor, the economic, ecological and health consequences of large wildfires are huge [100]. Climate change and weather patterns occur at a global scale and over a long period of time, resulting in protracted periods of drought, fuel dryness and atmospheric conditions conducive to large fires, whereas fire agencies can often manage forest growth



or fuel abundance in local or regional settings, especially in WUIs or near transitions from forest to grassland. Therefore, it is important to study the effect of forest structure on surface fires as a potential trigger to fires transitioning to intense and fast-moving crown fires.

Also, as seen in many dramatic fire events, crown fires, generally characterised by a high-intensity and therefore strong convective plume, also contribute to significantly increase the generation rate of firebrands. Owing to the mechanical action of the strong convective plume observed under these conditions, these firebrands can be transported over long distances (a few kilometres) and can ignite numerous secondary fires ahead of the main fire front. This mode of propagation is considered the major source of fire hazard in the WUI. Because clearings or a fuel breaks contribute to reducing fire intensity, they also constitute a means of reducing firebrand generation, which justifies interest in studying such configurations. This study sought to evaluate the impact of the presence of a canopy upstream of a grassfire, especially the modifications of local wind conditions before and inside a clearing or fuel break. Knowledge of this kind forms a major element of improving safety conditions for forest managers and firefighters in charge of firefighting or prescribed burning operations in such configurations. Another aim was to study the behaviour of fire under realistic turbulent flow conditions, i.e. flow resulting from the interaction between an atmospheric boundary layer and the surrounding canopy.

Earlier in this report, it was shown that we are able to define the geometry of a tree in physics-based modelling. This enables researchers to estimate drag coefficients, and as a result, numerically predict the velocity profiles of wind through some types of vegetation. As mentioned earlier, there have been experimental and numerical studies to understand sub-canopy wind behaviour [15, 49, 53, 101-103], both deep within a canopy and near canopy edges. Cassiani *et al.* [49] explored the flow characteristics of the downstream edge region in detail and found that for dense canopies, a mean recirculation region was established similar to flow over a backward-facing step. Far from the canopy, the flow can become similar to an open-field wind profile. However, studies of fire propagation through forest canopies or downstream of the edges of a forest canopy are rare – the only known study is Sutherland *et al.* [104]. Without such studies, it is difficult to quantify the actual effect of the presence of forest canopy on the ROS. Experimental studies of this effect involving fire are often prohibitively difficult owing to safety concerns, expense and uncontrolled interaction of multiple physical and chemical phenomena. However, this configuration is particularly interesting from a practical point of view, because it can be encountered quite frequently during prescribed burning operations.

In this study, FIRESTAR3D is used. The objectives of this part of the study are (1) to study the flow redevelopment downstream of a tree canopy; (2) to characterise the ROS and the fire intensity of an idealised surface fire downstream of a canopy; and (3) to quantify the effect of the canopy on the ROS and the fire intensity.

### **Fire transitioning from the forest floor to the canopy**

As canopy fire can be very fast-moving and emit firebrands in large numbers, it is important to explore the extension of previous studies of grassfires to tree and forest canopy fire. In this study, we first studied a single tree burning quantitatively, following Mell *et al.* [28]. Then we semi-quantitatively studied a forest floor fire

transitioning to a crown fire and the forward advancing behaviour of the crown fire.

## RESEARCH APPROACH

### Modelling with WFDS


In the WFDS simulations reported here, the Boundary Fuel (BF) model is adopted. The BF model is designed to simulate surface fuels such as grasslands [28]. The burnable material is considered to be a thin layer at the bottom boundary. The BF model uses a separate vertical computational grid for the fuel bed. This grid has a sufficiently high spatial resolution to capture the vertical radiant heat transfer. The horizontal grid is the same as the gas phase and the accuracy of convective heat transfer is heavily influenced by the gas-phase grid resolution. The assumptions leading to the BF model are most consistent with large fires for which the majority of the heat release (and, therefore, radiant emission) occurs above the fuel bed (resulting in predominantly vertical radiant heat transfer in the thermally degrading fuel bed). Fuels such as tall grasses exert drag forces on the prevailing wind. The BF model accounts for fuel drag by an aerodynamic drag force of the form:

$$F_{D,i} = -C_D \alpha u_i u_i \quad (13)$$

where  $C_D$  and  $\alpha$  are parameters estimated by considering each blade of grass as a cylinder,  $u$  is the mean velocity in the longitudinal direction and  $i$  represents each of the three coordinates.

The alternative model provided in WFDS is the Fuel Element (FE) model. In the FE model, the fuel is represented by individual particles located near and above the ground. Although this model is slightly more faithful to reality, it requires a prohibitively fine grid (i.e. too computationally demanding) to capture the physical processes in the fuel bed. In this model, the extinction length ( $\delta_R$ ) characterising the absorption of radiation by vegetation, which is the governing length scale in the vegetation fuel bed [105], needs to be resolved.  $\delta_R$  can be obtained from  $4/(\text{packing ratio} \times \text{surface-to-volume ratio})$ , and packing ratio can be obtained from vegetation load, height and element density [106]. To resolve the fuel bed in the FE model, the grid size within the fuel bed needs to be lower than  $\delta_R$ , and Mell *et al.* [28] suggested grid size be one-third of  $\delta_R$ . This condition cannot be met using the FE model while also having a sufficiently large domain given currently available computational resources and numerical approaches. When the fuel bed cannot be appropriately resolved, the BF model is the alternative, despite losing part of the ability to calculate the physics of flow inside the fuel bed [105]. As the vertical grid resolution is determined by  $\delta_R$  constraints, the BF model is typically less computationally demanding than the FE model owing to the coarser gas-phase grid (Mell *et al.* [28]). For more information on the precise formulation of each of these models, see Mell *et al.* [28, 29] and Perez-Ramirez *et al.* [106].

Owing to computational restrictions, while assessing AS3959, we had to make some compromises. AS3959 assumes a straight-line fire of width 100 m, that is, the fire is assumed to behave like a two-dimensional line fire. However, to reduce computational demand, a fire width of 20 m is used for our study. Linn *et al.* [107] demonstrated that this width is adequate for quasi-two-dimensional simulations,



and note that the ROS of a straight-line fire is significantly greater than the ROS of a naturally curved fire. It is important to note that the fire is still three-dimensional, although it is similar at every location in the span-wise direction. This approach was adopted for the present simulations because the standard assumes a straight-line fire. In reality, a perfectly straight-line fire is unlikely, as fire fronts often propagate in an elliptical shape. As such, the distance from the fire front to a structure, and therefore the radiative heat load, would vary as a function of position along the curved fire line.

### Modelling with FIRESTAR3D

FIRESTAR is another three-dimensional physics-based model with an LES-based turbulence module. It emerged from a two-dimensional model [108] and evolved into a three-dimensional one [109]. FIRESTAR3D is based on a multi-phase formulation and solves the conservation equations of the coupled system formed by the vegetation and the surrounding gaseous medium. The model takes into account vegetation degradation processes (drying, pyrolysis and combustion), the interaction between the atmospheric boundary layer and vegetation (aerodynamic drag, heat transfer by convection and radiation, and mass transfer), and transport in the gaseous phase (convection, turbulence and combustion).

The  $HRR$  (representing fire size) is given by Eqn (14), where  $\omega_{vap}$ ,  $\omega_{pyr}$ ,  $\omega_{char}$ ,  $\omega_{CO}$  and  $\omega_{soot}$  are respectively the total mass rates of water evaporation, pyrolysis, char combustion, combustion of CO in the gas mixture, and soot combustion, and  $\Delta H_{vap}$ ,  $\Delta H_{pyr}$ ,  $\Delta H_{char}$ ,  $\Delta H_{CO}$  and  $\Delta H_{soot}$  are the corresponding specific heats. Note that  $\Delta H_{char}$  is not constant, as it depends on the proportion of CO to CO<sub>2</sub> produced during charcoal combustion [110]; it varies from 9 MJ/kg for incomplete combustion to 30 MJ/kg for complete combustion.

$$HRR = -\omega_{vap} \cdot \Delta H_{vap} - \omega_{pyr} \cdot \Delta H_{pyr} + \omega_{char} \cdot \Delta H_{char} + \omega_{CO} \cdot \Delta H_{CO} + \omega_{soot} \cdot \Delta H_{soot} \quad (14)$$

### Forest fire burning

For the tree burning simulations, two different sets of experiments of Douglas firs burning conducted at NIST are considered [29] [40]. During these experiments, trees were mounted on custom stands and allowed to dry. Trees were ignited using a circular natural gas burner with a specific heat release rate of 30 kW. The mass of the sample tree was measured, and the mass loss rate calculated taking into consideration the moisture content of the samples. In [29], 2.6-m trees were separated into two groups with average moisture content by mass of 14 % and 49 %. In [40], a 2.6-m tree was dried to an average moisture content of 10% before being burned in no-wind conditions. Further, firebrands were collected by placing water-filled pans at strategic locations in a series of scoping experiments [40].

FDS and WFDS models have two ways of modelling vegetative fuels, namely: (i) the FE model for vegetation that occupies a specified volume such as trees (for example, Douglas firs are modelled as cones [29]), and (ii) the BF model for surface fuels such as grasslands [2]. With the FE model, trees can be modelled with various shapes: cone, frustum, cylinder and rectangle. In the FE model, there is no distinction between the solid-phase and gas-phase grid. The grid resolution



is the same for both phases. The fuel distribution within the tree (i.e. the leaves and twigs) is modelled as a cloud of burnable particles with the specified properties. While the BF model is the same in WFDS and FDS, the FE model is slightly different in FDS. The BF model is discussed in the *Grassfire Modelling* section above.

At first, a Douglas Fir tree crown is approximated as being cone-shaped with four different sizes of particles in both models. We use two thermal degradation sub-models to simulate the tree burning of [29] – WFDS' linear pyrolysis model and FDS' simplified Arrhenius model. Both models have the same fluid flow, turbulence, continuity, pressure, energy, radiative heat transfer and combustion models. They also simulate the fuel distribution in a similar, but not identical, manner. The main difference is in the thermal degradation sub-model, which is discussed in the next section. After replicating the experiments of Douglas fir burning using two models, we model fire behaviour with the WFDS linear model in a forest of Douglas firs sitting on a grassland – a hypothetical scenario that can be thought of as a plantation. The behaviours include transition from surface fire to crown fire, forward advance of both crown fire and surface fire, etc.

## FINDINGS

A physics-based model capable of both fuel–fire and fire–atmosphere interaction is an important tool for understanding wildland and wildland–urban interface fire behaviour outside the scope of empirical and semi-empirical models. We conducted a pioneering study [2] with the new WFDS version (FDS version 6 compatible) to investigate some interesting features of dynamic fire behaviours such as the effects of driving velocity and grass height on ROS as well as fire propagation mode (wind-driven vs plume-driven). Some comparison was made against empirical and semi-empirical models.

### Grassfire propagation over sloping terrain

A comprehensive study on grassfire behaviour on different slopes and wind velocities was conducted. This study also compared ROS from different empirical and semi-empirical models together with new findings based on sloping terrains.

Isochrones of fire progressions as a function of time are presented in Figure 27 at wind velocities of 12.5, 6 and 3 m/s. Owing to space constraints, only three cases are presented for each of the velocities. In these simulations, the fire contours are defined as the region on the boundary where the temperature of the vegetation is at or above the pyrolysis temperature of 400 K. Pyrolysis fronts are plotted at different times after ignition and when the flame propagates to the end of the burnable plot.

It is evident that as the slope angle increases, the pyrolysis front becomes wider and reaches the end of the burnable grass plot much earlier compared with cases with lower slope angles. With 12.5 m/s, the pyrolysis front travel times obtained are 66, 60, 54, 48, 45, 42 and 39 s for upslope angles 0°, 5°, 10°, 15°, 20°, 25° and 30°, respectively, whereas the pyrolysis front is found to be moving more slowly with increase in downslope slope angles. For 5°, 10°, 15°, 20°, 25° and 30° downslope angles, the pyrolysis front travel times are 70, 76, 80, 88, 97 and 98 s, respectively. As the downslope angle increases, the pyrolysis front becomes thinner; however, the decrease is not significantly higher with increase in slope





angle as observed with upslope cases. For the same slope angle, as the driving wind velocity increases, the pyrolysis front travels more quickly and reaches the end of burnable plot earlier. For downslope cases with lower wind velocities (especially 3 m/s), as the downslope angle increases, the fire front is observed to be moving very slowly. This lower driving wind velocity may not be sufficient to drive the fire front as it moves on steep downslopes such as 20° and 30°. This is also the case for 30° downslopes at 6 m/s driving velocity. Other reasons may be fuel physical parameters such as fuel height, fuel load and thermophysical properties, which could be investigated separately in future studies.

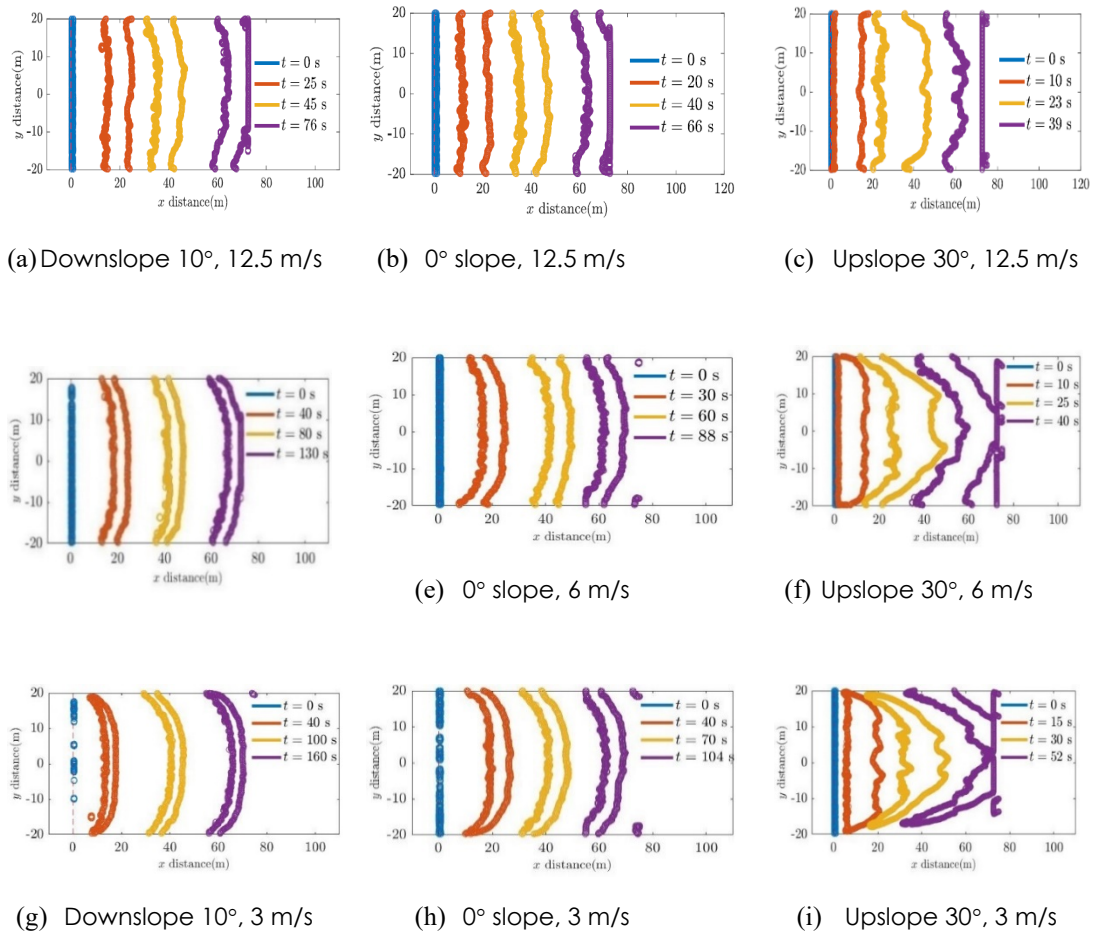


FIGURE 27: PROGRESSION OF ISOCHRONES FOR WIND VELOCITIES OF 12.5, 6 AND 3 M/S.

The pyrolysis width (also known as head fire width) as a function of time is presented in Figure 28(a) for the driving wind velocity of 12.5 m/s. For the upslope cases, pyrolysis width increases as the fire front progress from the ignition line, then it plateaus (i.e. reaches a quasi-steady state) except for a few high upslope cases e.g. 30° at 6 m/s, and finally decreases. Generally, as the upslope angle increases, the width of the plateau decreases, and the magnitude of the pyrolysis width increases. The reverse scenario is found with the downslope cases, where the width of the plateau increases and its magnitude decreases as the downslope angle increases. Pyrolysis width values are much higher for upslope cases compared with downslope cases.

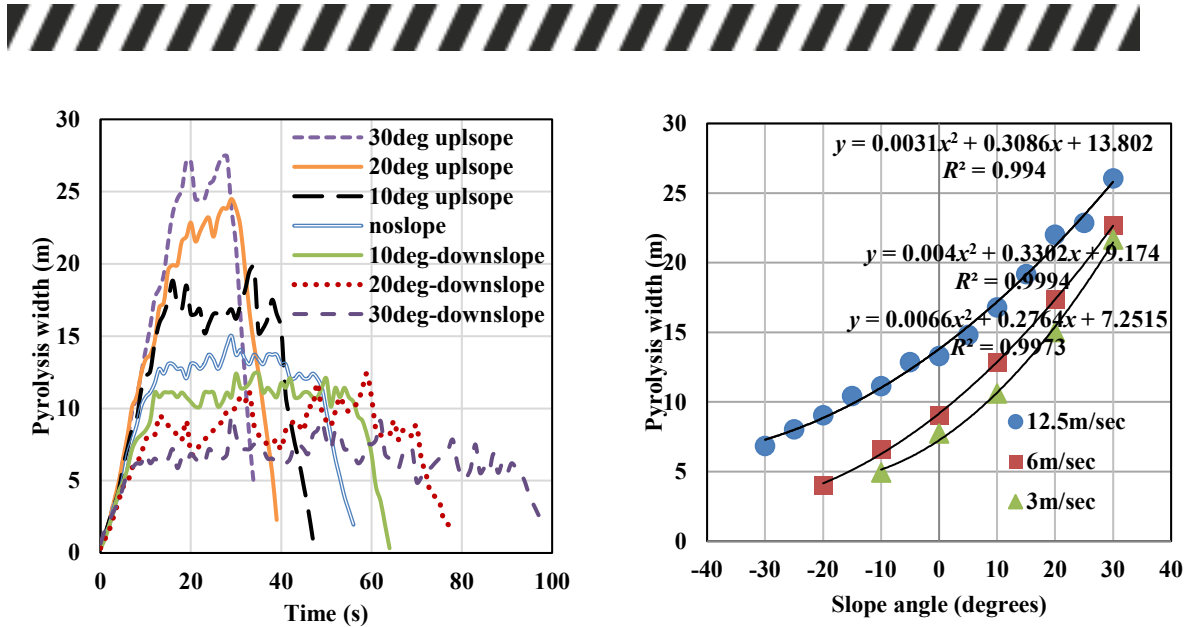


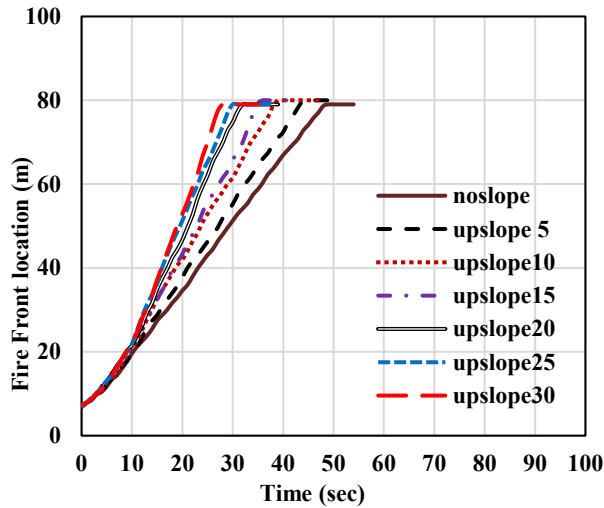
FIGURE 28: PYROLYSIS WIDTH FOR UPSLOPE AND DOWNSLOPE CASES. (A) PYROLYSIS WIDTH AS A FUNCTION OF TIME AT 12.5 M/S WIND VELOCITY. (B) QUASI-STEADY PYROLYSIS WIDTH VS SLOPE ANGLES AT 12.5, 6 AND 3 M/S WIND VELOCITIES.

For a given slope angle, the pyrolysis width increases as the wind velocity increases. At lower wind velocities, 6 and 3 m/s, as the downslope angle increases, the pyrolysis width decreases. Figure 28(b) represents quasi-steady pyrolysis width versus slope angle for all cases, at 12.5, 6 and 3m/s wind velocities.

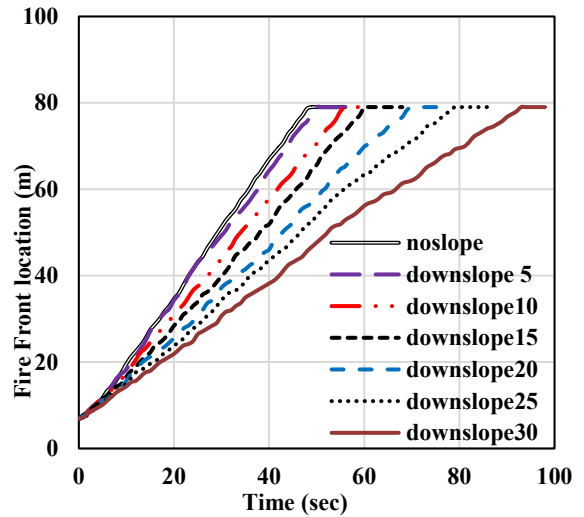
The width values are extracted approximately 15 to 35 s from the start of ignition for upslopes and approximately 12 to 60 s from start of ignition for downslopes. These values are approximate for 25° and 30° upslope cases as the fire front reaches the end of fire plot much more quickly for these cases and reaches peak values much earlier. Hence, for higher upslope cases, a perfectly steady pyrolysis width condition is not attained at any given time. The pyrolysis width increases by approximately 25–30% for every 10° upslope increase, and decreases with increase in downslope angles. As mentioned earlier, for lower wind velocities, fire did not propagate for higher downslopes and hence –30° at 6 m/s, –30° and –20° at 3 m/s are not included in the slope angle–pyrolysis width plot. The pyrolysis width–slope angle trend shows a second-order polynomial relation for all three wind velocities.

For a given slope angle, the pyrolysis width increases with driving wind velocity. For upslope cases, for higher wind velocity, the head fire width increases by approximately 20–28%. For downslopes, the decrease in pyrolysis width with velocity is significantly higher than that observed with upslope cases.

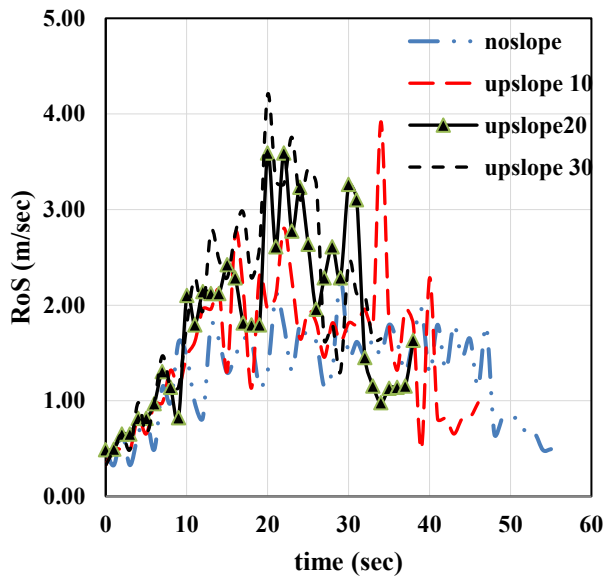
The fire front location is determined by the boundary centreline temperature as the fire moves through the grass regions. The temporal fire front locations at 12.5 m/s are shown in Figure 29(a) and Figure 29(b) for upslopes and downslopes, respectively. The fire front is found to be moving faster with increasing upslope angles. At a given time, the fire front location for the 30° upslope case is farther by approximately 45% than that of the no-slope situation. As shown in Figure 29(b), for downslope cases, the fire front is found to be moving faster with a decrease in the downslope angle. The greater the downslope angle, the smaller the distance the fire front travels in a given time. At a given time, the fire front location for the 30° downslope case travels approximately 55% less than that of no-slope situation.



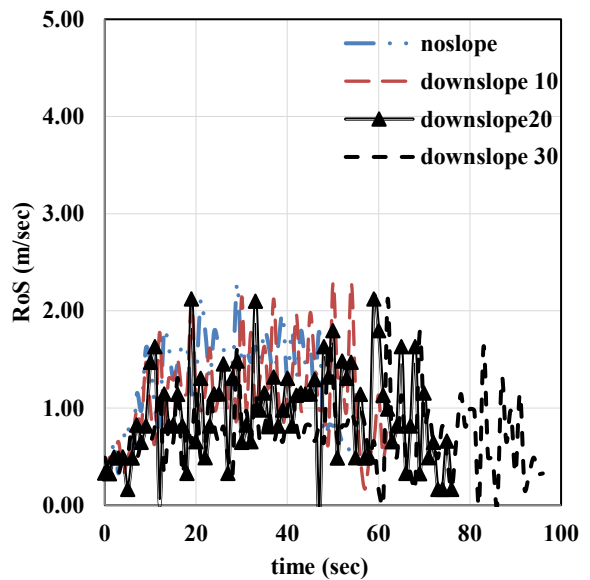
(a) Firefront locations – upslope



(b) Firefront locations – downslope



(c) Dynamic ROS – upslope



(d) Dynamic ROS – downslope

FIGURE 29: FIRE FRONT LOCATIONS AND DYNAMIC ROS AT WIND VELOCITY OF 12.5 M/S: (A) FIRE FRONT LOCATIONS VS TIME, UPSLOPE; (B) FIRE FRONT LOCATIONS VS TIME, DOWNSLOPE; (C) DYNAMIC ROS VS TIME, UPSLOPE; (D) DYNAMIC ROS VS TIME, DOWNSLOPE.

Although the focus of this study is to compare quasi-steady fire behaviour with that from operational models, we also attempted to analyse dynamic fire behaviour. Sutherland *et al.* [3] demonstrated that dynamic fire behaviour exists, and presented ROS as a function of time by differentiating the fire front location data. We used the same analysis technique to derive dynamic ROS for all slope cases. These ROS values as a function of time are plotted in Figure 29(c) and Figure 29(d), at a driving wind velocity of 12.5 m/s, for upslopes and downslopes, respectively. The plots show spiking up and down in ROS values as the fire front moves, and the highest spike is observed for 30° upslope. The fluctuations in dynamic ROS values for downslope cases are not as significant.

Figure 30 represents ROS comparisons for all slope cases at all three wind velocities. The quasi-steady ROS values for each of the slope cases are calculated from the fire front location when steady state conditions are reached. The least-squares approximation method is applied to develop ROS–slope angle correlations with a linear fit to the plots as shown in Figure 29(a, b). Note that steady states are not achieved for higher downslope angles at lower wind



velocities and hence  $-30^\circ$  at 6 m/s,  $-30^\circ$  and  $-20^\circ$  at 3 m/s are not included in the ROS–slope angle correlation plots. The slope of each linear fit represents quasi-steady ROS for each case. For all cases, for the quasi-steady region, the  $R^2$  value is found to be  $\sim 0.99$ , indicating that the quasi-steady ROS values are captured accurately from a linear curve. The slope (ROS) values obtained from the linear fit equations are plotted against degrees of slope in Figure 30(a–d). The dynamic ROS are plotted with maximum and minimum bounds in Figure 30(b–d), along with quasi-steady ROS values. The dynamic ROS values (maximum, averaged and minimum) extracted from the plots in Figure 29(c) and (d), for 12.5 m/s are presented in Figure 30(b). Similar analysis techniques are used to derive dynamic ROS values for the 6 and 3 m/s velocity cases and are presented in Figure 30(c) and (d), respectively. The dynamic averaged ROS values are found to be closer to quasi-steady ROS values for all three velocity cases.

Figure 30(a) represents the quasi-steady ROS vs wind velocity correlation of this study at  $0^\circ$  slope or flat terrain, for 12.5, 6 and 3 m/s, along with empirically derived ROS values at  $0^\circ$  slope. From Figure 30(a), it can be seen that the quasi-steady ROS values for flat terrain obtained from this study are comparable with the WFDS simulations of Moinuddin *et al.* [2]. The minor difference is due to the use of synthetic eddy methodology (SEM) and a different ignition protocol. The ROS values of MK3 and MK5 are derived from a set of equations presented by Noble *et al.* [91]. In the plot, empirically derived ROS values from the CSIRO [88], original Rothermel and modified Rothermel models [97] are also presented. These empirical formulas are derived from experimental observations conducted under a range of fuel parameters and ambient weather conditions. Some were developed from wind tunnel data or based on spot fires. Furthermore, our fires are fundamentally dynamics as shown in Figure 30(c) and (d). Overall, the geometry, scale of the fire, various boundary conditions were different from our simulations and despite these, the results are not too different.

The empirically derived ROS values from the above-mentioned operational models (except CSIRO as no slope factor is available for it and MK3 are MK5 are slope-corrected) are also presented in Figure 30(b–d), along with ROS values obtained from the WFDS simulations in this study. From Figure 30(b), it can be seen that the 'quasi-steady' and 'dynamic averaged' ROS values obtained from this study are closer to the 'slope-corrected' MK5 values for the upslope angles  $0^\circ$  to  $+10^\circ$ . Above  $+10^\circ$ , MK5 values match better with 'dynamic maximum' ROS values. The 'quasi-steady' and 'dynamic averaged' ROS values above  $+10^\circ$  slope fit between original and modified Rothermel models – more closely to the modified one for higher upslope angles. The upslope ROS values with 'slope-corrected' MK3 are found to be significantly higher than the 'quasi-steady' and 'dynamic averaged' ROS values obtained from the present study. However, between  $+5^\circ$  and  $+15^\circ$ , better matching is obtained with dynamic maximum ROS values. On the other hand, 'quasi-steady' and 'dynamic averaged' ROS values for downslopes are closer to MK3 values for slope angles for up to  $-5^\circ$ . From  $-10^\circ$  to  $-30^\circ$ , the 'quasi-steady', 'dynamic averaged' and 'dynamic maximum' ROS values are found to be higher than both MK5 and MK3 slope-corrected models and the difference widens as the downslope angle increases. This decrease as the slope angle decreases is much lower than the operational correlations. However, the 'dynamic minimum' ROS values in this slope range ( $-10^\circ$  to  $-30^\circ$ ) are closer to both MK5 and MK3 slope-corrected model values. Rothermel

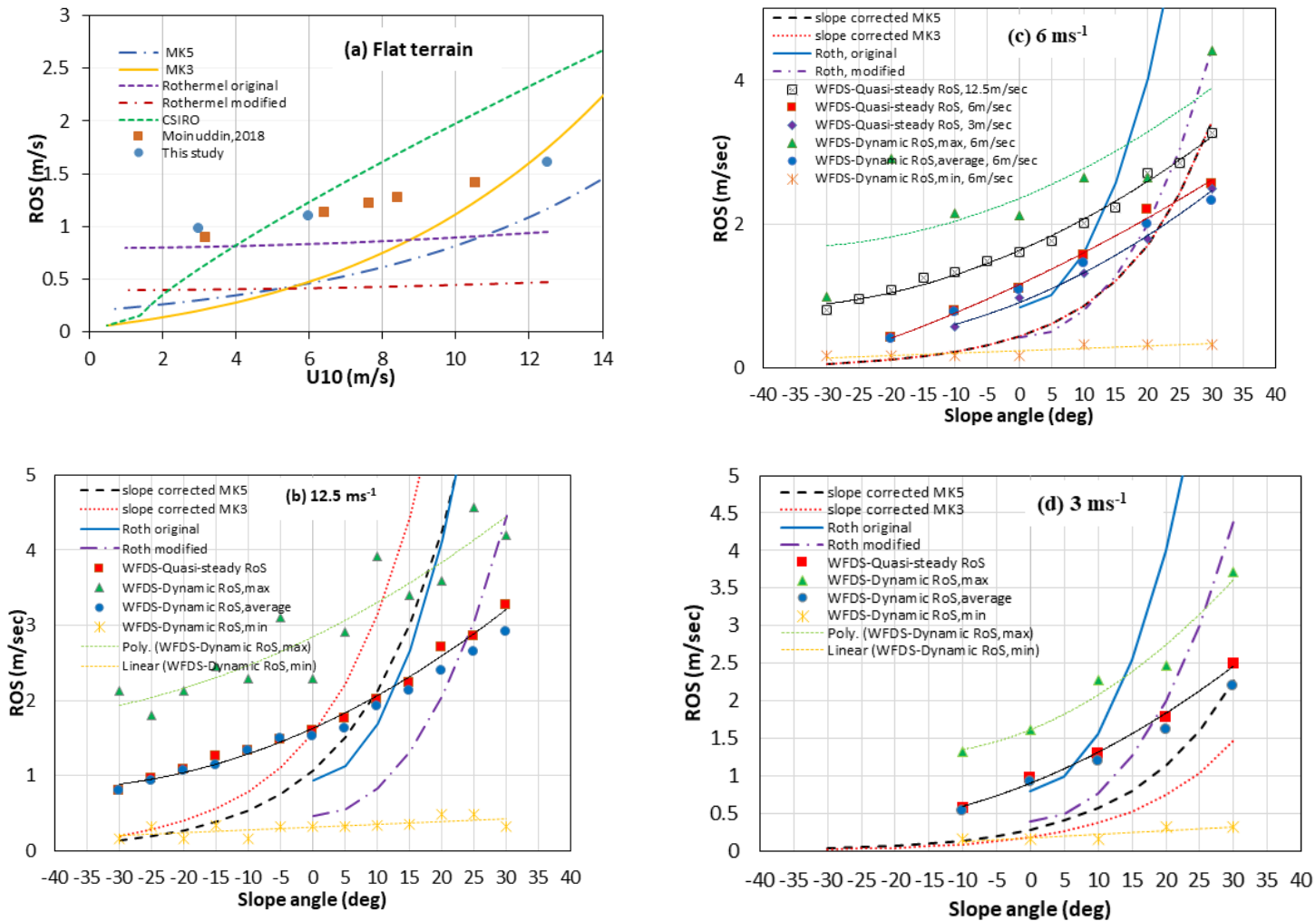


FIGURE 30: RATE OF SPREAD–SLOPE ANGLE CORRELATIONS: (A) ROS VS WIND VELOCITIES AT 0° SLOPE CASES (FLAT TERRAIN); (B) ROS VS SLOPE ANGLE AT 12.5 M/S; (C) ROS VS SLOPE ANGLE AT 6 M/S ALONG WITH 12.5 AND 3 M/S; (D) ROS VS SLOPE ANGLE AT 3 M/S.



models were developed for upslope fire spread [102] and hence the ROS for downslope cases are not compared with Rothermel models.

Overall, empirical values lie in between 'dynamic minimum' and 'dynamic maximum' ROS values except at  $\geq 15^\circ$  where 'dynamic maximum' values are closer to empirical values and different numerical ROS values are closer to different empirical model values at different slope angles. Essentially, the differences are attributable to the fundamentally dynamic nature of grassfire propagation and challenges related to capturing these dynamisms in experimental studies. The value of quasi-steady ROS for  $-20^\circ$  is found to be  $\sim 30\%$  less than that of the zero-slope condition. These results are consistent with the study of Sullivan *et al.* [94] who argued that the value of ROS for negative slope situations should never be less than 60% that of the zero-slope condition. Figure 30(c) shows that the 'quasi-steady' and 'dynamic averaged' ROS values obtained from the present study at 6 m/s are higher than 'slope-corrected' MK3 and MK5 values for slope angles up to  $20^\circ$  and lower for  $30^\circ$ . For downslopes, 'dynamic minimum' values are closer to these two empirical models. The ROS values for 'no-slope' MK3 and MK5 look identical, as shown in Figure 30(a) for 6 m/s and hence the 'slope-corrected' MK3 and MK5 values also do. The 'quasi-steady' and 'dynamic averaged' ROS values from this study for upslope angles up to  $10^\circ$  are higher than both original and modified Rothermel models and above  $10^\circ$ , the values roughly lie between original and modified Rothermel models.

Figure 30(d) shows that the 'quasi-steady' and 'dynamic averaged' ROS values for 3 m/s obtained from this study are higher than 'slope-corrected' MK3 and MK5 values, but 'dynamic minimum' values are closer to MK3 in the range of  $-10^\circ$  to  $+20^\circ$  slope. The 'quasi-steady' and 'dynamic averaged' ROS values are lower than original Rothermel for all upslope angles, but close on flat ground, and higher than modified Rothermel up to the slope angle  $15^\circ$ . Modified Rothermel values are closer to 'dynamic maximum' values at  $+20^\circ$  and  $+30^\circ$  slope. Other than for the higher original Rothermel value at 6 m/s for  $+30^\circ$  and 3 m/s for  $\geq +20^\circ$ , all empirical values roughly lie between 'dynamic minimum' and 'dynamic maximum' ROS values, reinforcing that the fundamentally dynamic nature of grassfire propagation is the primary source of the differences.

From Figure 30(b), (c) and (d), a second-order polynomial relationship is observed between quasi-steady ROS and slope angles for all three velocity cases. It is to be noted that the relationship for 3 m/s can also be developed as exponential. It is likely that as the driving wind velocity decreases, the relationship becomes exponential. As most experimental studies are conducted with no or very low wind speed, researchers often report exponential relationships. The slope factors in operational correlations are exponential, and are likely derived from very-low-velocity laboratory slope studies. However, with significant driving velocity and the dynamic nature of fire propagation, the trend between quasi-steady ROS and slope angles fits a second-order polynomial relationship more closely, as shown in Figure 30(b–d) for all three wind velocities. Comparing the three velocity cases, for corresponding slopes, we present the quasi-steady ROS values for 12.5 and 3 m/s along with 6 m/s in Figure 30(c): it is evident that for a given slope angle, ROS values with lower wind velocities are lower; however, the difference narrows between 3 and 6 m/s as the slope angle increases. We found that for upslopes ( $\geq +20^\circ$ ), quasi-steady ROS values from WFDS are closer to the modified Rothermel model than to the Australian operational correlations, which



may be due to the multiplicative nature of Australian operational correlations compared with the Rothermel models' additive nature. We also observed second-order polynomial relationships between 'dynamic maximum' ROS values and slope angles for all three velocity cases. However, for 'dynamic minimum', the relationships are linear.

### Grassfire propagation downstream of a forest canopy

The behaviour of a grassland fire propagating downstream of a forest canopy was simulated numerically using the fully physics-based wildfire model FIRESTAR3D. This configuration reproduces quite accurately the situation encountered when a wildfire spreads from a forest to an open grassland, as can be the case at a fuel break or a clearing, or during a prescribed burning operation.

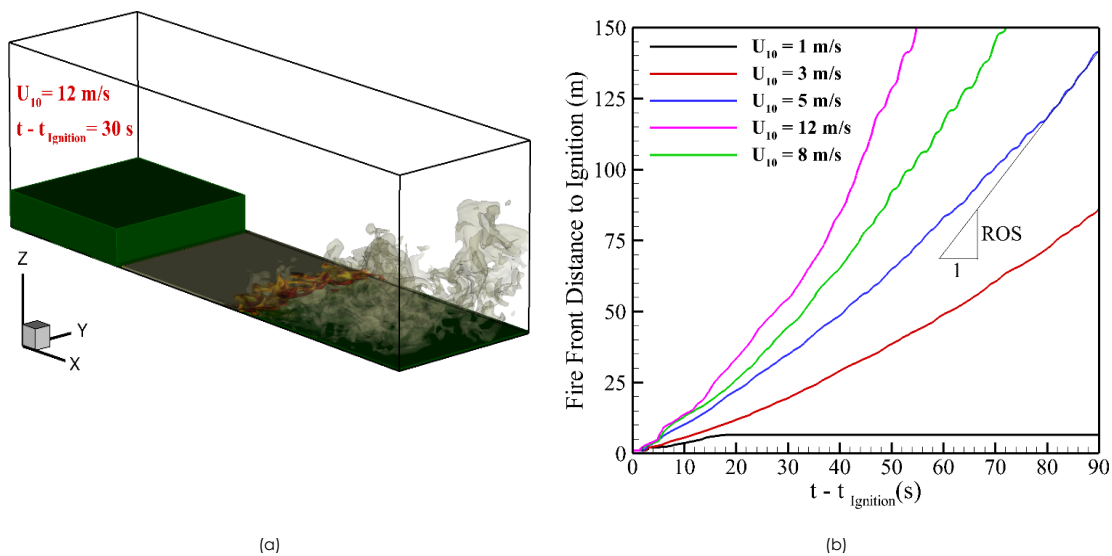


FIGURE 31: (A) 3D VIEWS OF GRASSLAND FIRE SPREAD DOWNSTREAM OF A CANOPY OBTAINED FOR  $U_{10} = 12 \text{ m/s}$ , 30 S AFTER IGNITION. (B) TIME EVOLUTION OF THE AVERAGE POSITION OF THE FIRE FRONT AT THE GRASSLAND SURFACE OBTAINED FOR DIFFERENT WIND SPEEDS. THE ROS IS THE SLOPE OF THE CURVE AT STEADY FIRE PROPAGATION. T REPRESENTS TIME.

The study was divided into two phases. The first phase consisted of generating an ABL/canopy turbulent flow above a pine forest (10 m high, 200 m long) using periodic boundary conditions along the streamwise direction. LESs were carried out for a sufficiently long time to achieve quasi-fully developed turbulence. The second phase consisted of simulating the propagation of a surface fire through a grassland, bordered upstream by a forest section (having the same characteristics used for the first step), while imposing the turbulent flow obtained from the first step as a dynamic inlet condition to the domain. The simulations were carried out for 10-m open wind speeds between 1 and 12 m/s; these values allowed the simulations to cover the two regimes of propagation of surfaces fires, namely plume-dominated and wind-driven fires.

A representative visual fire propagation is shown in Figure 31(a), in isosurfaces of soot value illustrative of the flame for  $U_{10} = 12 \text{ m/s}$ , also showing the configuration of the scenario.

The front location (average of the pyrolysis front position in the y-direction at the grassland surface) is shown in Figure 31(b) as a function of time. The  $U_{10} = 1 \text{ m/s}$  case extinguishes approximately 15 m downstream of the ignition location. The wind velocity at flame height is very low and is likely insufficient to sustain a propagating fire in this particular fuel bed. All other cases propagate to the end



of the domain in an approximately quasi-equilibrium manner, as indicated by the approximately linear behaviour of frontal location with time. All of the average frontal positions as a function of time shown in Figure 31 (b) are slightly non-linear, indicating that the fires are slowly accelerating.

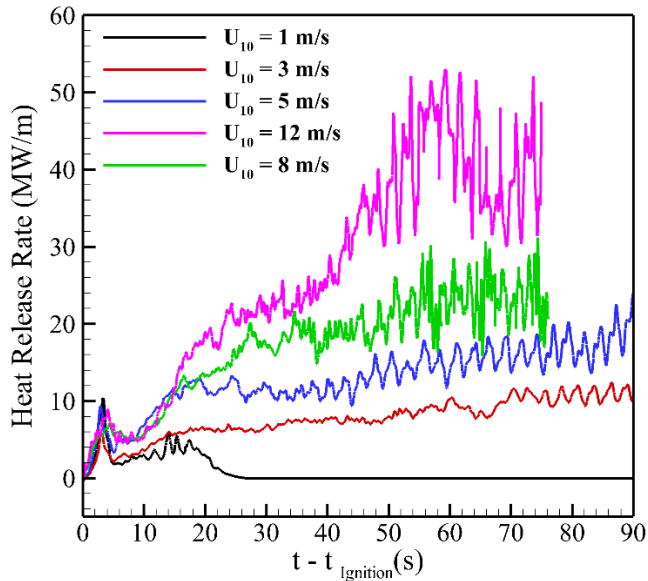


FIGURE 32: TIME EVOLUTION THE TOTAL HEAT RELEASE RATE PER UNIT LENGTH OF THE FIRE OBTAINED FOR DIFFERENT WIND SPEEDS.

The fireline intensity, shown in Figure 32, per unit of fire line length (i.e. the domain width), was estimated from the total heat release rate (HRR) and the domain width. All fires follow roughly similar trends with a spike in intensity at ignition. The  $U_{10} = 1$  m/s case shows a brief period (between approximately 10 and 20 s) of quasi-equilibrium intensity, consistent with the period of linear growth in frontal location (Figure 31), before the intensity decays to zero as the fire extinguishes. The other cases grow towards a quasi-equilibrium intensity; however, with the exception of the  $U_{10} = 12$  m/s case, the intensity still grows very slowly throughout the simulation. The  $U_{10} = 3, 5, 8$  m/s cases tend towards intensities of 8, 14, 20 MW/m respectively. The amplitude of the variance in intensity also increases with time. The 12 m/s case behaves differently; the intensity peaks at around 60 s before decaying and re-intensifying between 60 and 80 s. This is suggestive of surge–stall behaviour [95], which is consistent with the step-like changes in the frontal location that emerge approximately 50 s after ignition. The variation of the intensity also increases with wind speed across all cases. The  $U_{10} = 10$  m/s case also exhibits step-like behaviour in the frontal location, and some regular bursting in the intensity occurs at 55, 65, and 75 s after ignition. However, further investigation is required to completely characterise the fire behaviour over this regime.

The average quasi-equilibrium ROS was determined from the gradient of the most linear section of the fire location as a function of time [55]. The average ROS and intensities of the fires in open grassland (without the canopy) and downstream of the canopy are compared in Figure 33. Firstly, the open  $U_{10} = 1$  m/s case does not extinguish, suggesting that the sheltered wind speed downstream of the canopy is insufficient to sustain the fire when a canopy is present. The canopy does reduce the average ROS; however, the effect is minor. The largest difference, of approximately 15%, occurs in the  $U_{10} = 8$  m/s case (Figure 33(a)).



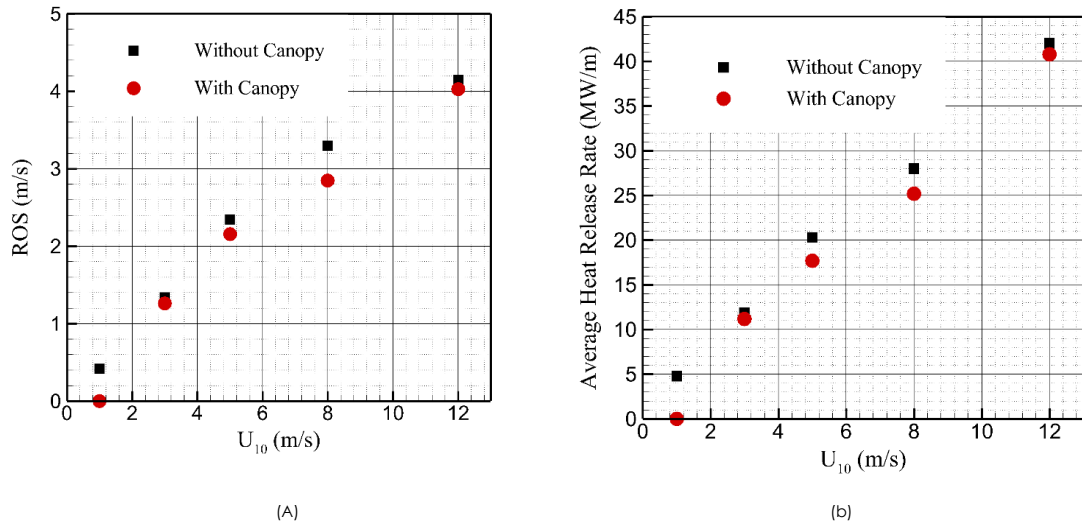


FIGURE 33: (A) RATES OF FIRE SPREAD OBTAINED AT STEADY STATE FOR DIFFERENT WIND SPEEDS IN THE PRESENCE OF A CANOPY COMPARED WITH THOSE OBTAINED FOR THE SAME SIMULATION CONDITIONS BUT WITHOUT A CANOPY. (B) AVERAGE HEAT RELEASE RATES OBTAINED AT STEADY STATE FOR DIFFERENT WIND SPEEDS IN THE PRESENCE OF A CANOPY COMPARED WITH THOSE OBTAINED FOR THE SAME SIMULATION CONDITIONS BUT WITHOUT A CANOPY.

The average intensity is also systematically lower downstream of a canopy than in the open by approximately 10% (Figure 33(b)). On the other hand, the average ROS and fire intensity obtained at steady state of fire spread are in agreement with experimental data [56] and with predictions of other numerical studies [57, 58] and empirical models [59, 60].

To quantify the implications of these differences, the average distances between fire fronts in the open and canopy cases are shown in Figure 34. To illustrate the differences, Figure 34(a) compares the frontal locations of the open (no canopy) and canopy cases with  $U_{10} = 3$  and 12 m/s. The fires in open grassland travel significantly further, approximately 50 m for  $t > 30$  s in the  $U_{10} = 12$  m/s case, ahead of the fires where a canopy is present. The distance systematically increases with wind speed, as shown in Figure 34(b), although the rate of growth decreases with increasing wind speed. In the  $U_{10} = 12$  m/s case, frontal locations differ by 52 m.

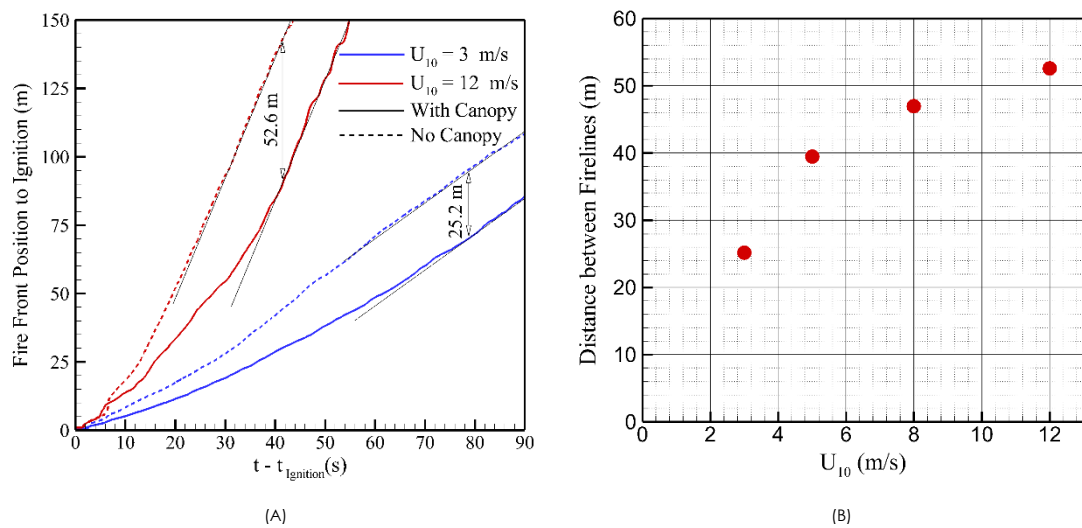


FIGURE 34: (A) TIME EVOLUTION OF THE AVERAGE POSITION OF THE FIRE FRONT AT THE GRASSLAND SURFACE OBTAINED FOR  $U_{10} = 3$  AND 12 M/S IN THE CASE OF FIRE SPREAD DOWNSTREAM OF A CANOPY, COMPARED WITH THE CASE OF FIRE SPREAD OBTAINED FOR THE SAME SIMULATION CONDITIONS BUT WITHOUT A CANOPY. (B) DISTANCE BETWEEN THE FIRE POSITION OBTAINED AT STEADY STATE WITH AND WITHOUT A CANOPY UPSTREAM FROM THE GRASSLAND FOR ALL CASES EXCEPT THE  $U_{10} = 1$  M/S CASE.

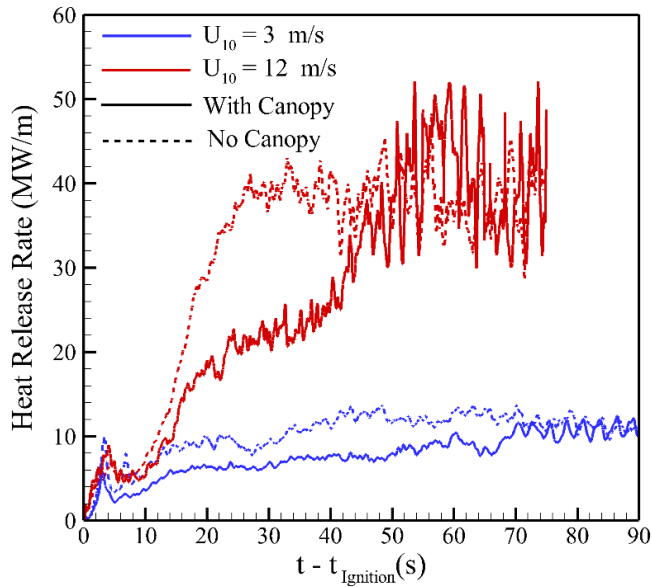


FIGURE 35: TIME EVOLUTION THE HEAT RELEASE RATE OBTAINED FROM EQUATION FOR  $U_{10} = 3$  AND 12 M/S IN THE CASE OF FIRE SPREAD DOWNSTREAM OF A CANOPY, COMPARED WITH THE CASE OF FIRE SPREAD OBTAINED FOR THE SAME SIMULATION CONDITIONS WITHOUT A CANOPY.

The intensity development shown in Figure 35 exhibits a similar delay. The  $U_{10} = 3$  m/s case recovers to the open intensity approximately 70 s after ignition, and the  $U_{10} = 12$  m/s case recovers approximately 50 s after ignition. The critical point between the two parts of the curve (sharp at the beginning and flatter at the end) seems to occur at  $U_{10} = 8$  m/s, which corresponds also to the beginning of the fully wind-driven regime for fire propagating through the canopy-free region. In fact, it is for this value of wind speed that the Byram convective number reaches a value nearly equal to 11 ( $>10$ , i.e. the beginning of a fully wind-driven fire regime). In analysing the fire intensity history in Figure 32 and considering the sudden increase of fluctuations highlighted for  $U_{10} = 8$  and 12 m/s, compared with the results obtained for lower values of wind speed, we concluded that for safety reasons, prescribed burning would be more suitable (in this configuration) for wind speed at least smaller than 5 m/s.

Because the fires downstream of a canopy recover to the open ROS and intensity after a maximum of approximately 50 m, the use of modified fire spread models in the wake of a canopy may be unnecessary. However, the recovery distance will likely depend on canopy height and LAI, which were constant throughout these simulations. Therefore, a more extensive parameter space investigation is required for some operationally useful criteria for fire redevelopment can be quantified.

### Effect of relative humidity on grassfire propagation

Moinuddin *et al.* [2] investigated two modes of fire propagation: wind-driven and buoyancy-driven outlined by Apte *et al.* [111]. They found that for the kind of grass modelled, based on Froude Number ( $Fr$ ), fire becomes buoyancy-driven when grass height increases from 0.175 to 0.21 m and above with temperature and relative humidity (RH) set to 32°C and 40%. To understand the role of RH in grassfire propagation and in switching propagation mode, two sets of grassfire simulations were conducted: one with 0.21-m grass and the other with 0.175-m grass. If the ambient temperature is kept constant, fuel moisture is directly correlated with RH (Eqn (10)). Therefore, in this study, fuel moisture (and RH) was varied by keeping the air temperature constant at 32°C. The driving velocity ( $U_{10}$ )

was also kept constant at 6 m/s. The RH range was 10% to 100% corresponding to a fuel moisture range of 3.55% to 12.5%.

Apte *et al.* [111] proposed using  $Fr$  as shown in Eqn (15) to distinguish two modes of fire propagation. Moinuddin *et al.* [2] used the same methodology.

$$Fr = \frac{U_{10}}{(gHRR/(\rho C_p T_s))^{1/3}} \tag{15}$$

Here,  $U_{10}$  is the velocity above 10 m, HRR is in kW,  $c_p$  in  $\text{kJ kg}^{-1} \text{K}^{-1}$  and  $T_s$  is the surface temperature, taken as 450 K. The other parameters used to compute  $Fr$  are the acceleration due to gravity  $g = 9.8 \text{ m/s}$  and density  $\rho = 1.2 \text{ kg/m}^3$ .

From the 0.21-m and 0.175-m-high grassfire simulations, HRR values are presented in Figure 36(a) and Figure 36(b), respectively. Ignition occurs at 504 s. It can be observed that when the grass height is constant, with the reduction of RH, the HRR (hence fire intensity) increases. To calculate  $Fr$  values, HRR values are averaged between 540 and 595 s for 0.21 m high grass cases and between 545 and 605 s for 0.175 m high grass cases. In these time periods, the HRR (hence the intensity) is quasi-steady.

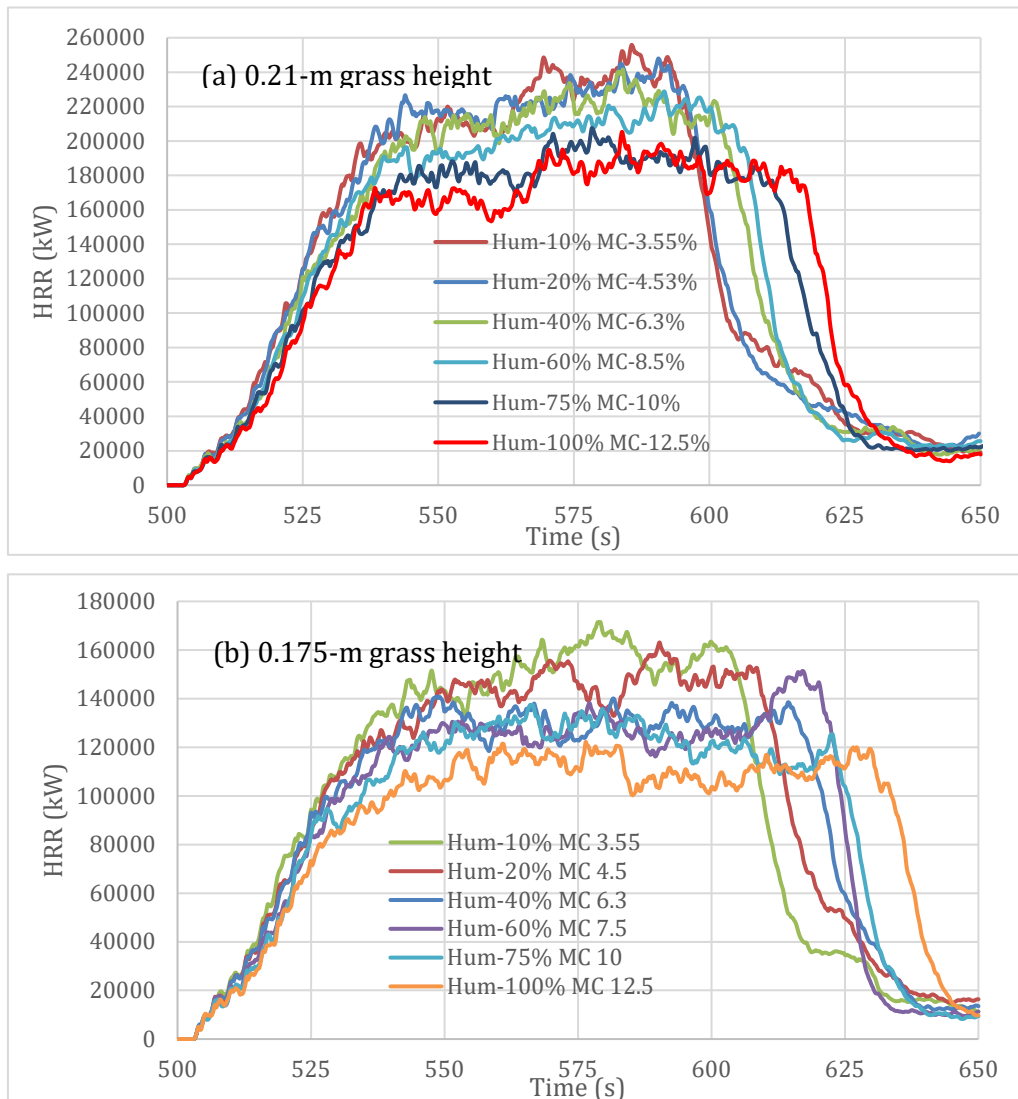


FIGURE 36: HRR FROM GRASSFIRE SIMULATIONS; IGNITION OCCURS AT 504 S.

$Fr$  values calculated using Eqn (15) for all cases are presented in Figure 37. Because of different wind and boundary conditions used in this study (synthetic eddy model for inlet and some surface roughness to rapidly promote wind turbulence), the threshold value is set as 0.39. For 0.175-m grass, fire propagation remains in wind-driven mode with the change of RH. However, for 0.21-m grass, with high RH (>40%),  $Fr$  values rise above the threshold line. This indicates transition from buoyancy-driven to wind-driven mode is due to decreased HRR (Figure 36(a)). An important finding of this study is that RH can contribute to different modes of propagation. However, comparing the data in Figure 37, it appears that while RH can lead to a change in propagation mode, a greater factor appears to be the grass height (fuel load).

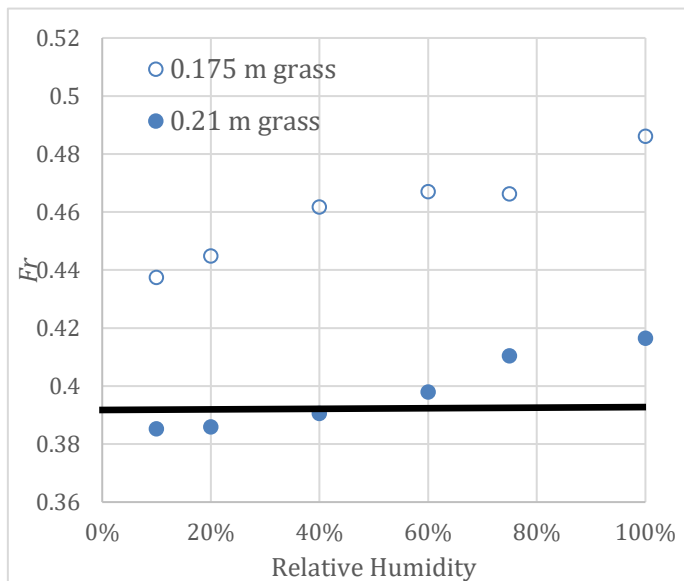


FIGURE 37:  $Fr$  VS RH FOR ALL SIMULATION CASES. THE BLACK LINE REPRESENTS THE THRESHOLD BETWEEN WIND-DRIVEN AND BUOYANCY-DRIVEN MODE; ABOVE THIS IS WIND-DRIVEN PROPAGATION.

### Forest fire burning simulation

The simulations show that in the given configuration with the assigned thermo-physical and flammability properties, surface fire to forest crown fire does occur. In Figure 38, the surface and crown fronts as a function of time are presented with the total HRR of the fire. Surface fires have a well-defined frontal location: the contour of boundary temperature at the surface where pyrolysis will commence. Crown fires do not have such a well-defined frontal location, and so integrated HRR data is used to determine the fire front location. The HRR data is taken along the domain centreline  $xz$ -plane. The HRR data is first integrated in the vertical direction for all  $z$ . The instantaneous flame front is defined to be located at the  $x$ -location where 90% of the total HRR is obtained. Quasi-equilibrium ROS may be determined from a least-squares regression fit of a straight line to the frontal locations. Here, the red line is the least-squares regression fit to the surface fire behaviour and the blue line is the fit to the crown fire data.

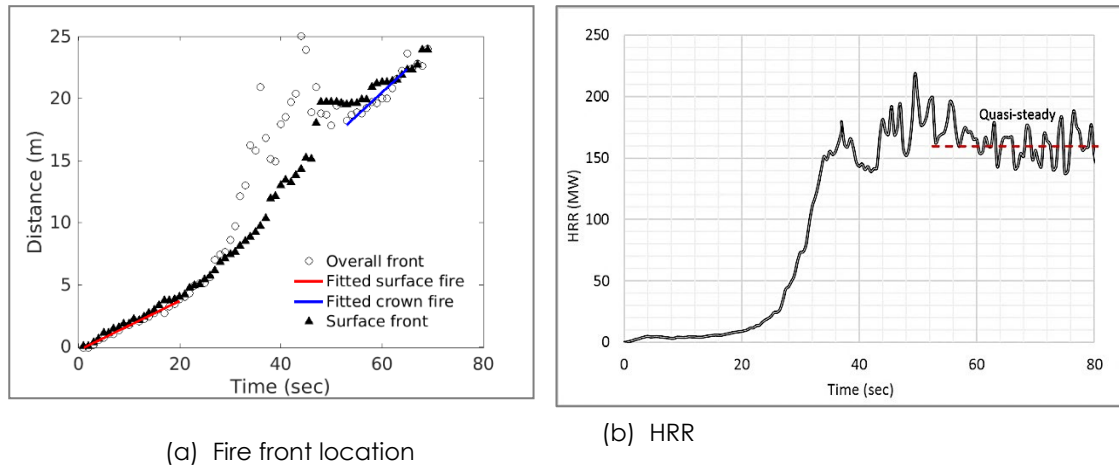


FIGURE 38: FINDING THE QUASI-STEADY RATE OF SPREAD OF A CROWN FIRE.

Surface fire alone is observed before ~30 s, with a transition from surface to crown fire occurring between 30 and 50 s. The total HRR achieves a quasi-steady state approximately 53 s after ignition. Throughout the fire propagation, the surface fire travels under the crown fire at about the same rate. The surface fire therefore supplies energy to maintain the fire in the tree crowns. This is referred to as a supported crown fire [112]. The isosurfaces of HRR at 200 kW/m<sup>3</sup>, seen in Figure 39, show the surface fire apparently transitions up into the crown before it transitions back from the crown to the surface. However, it is difficult to distinguish independent surface fire burning and crown fire burning from isosurfaces of HRR. Many features are qualitatively in agreement with other crown fire studies (e.g. experiments of [113]). Therefore, one can be confident that crown fire simulations are possible with the physics-based model.

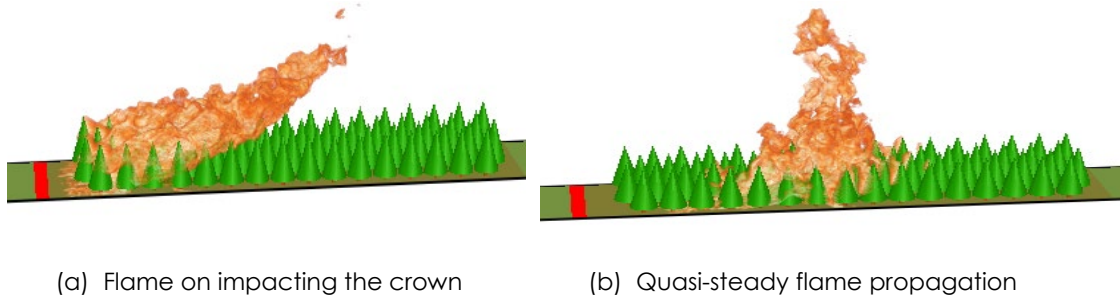


FIGURE 39: VISUAL REPRESENTATION FLAME PROPAGATION.

By changing the properties and configuration of the fuel material, simulation of native Australian vegetation can be attempted. In the future, similar simulations will lead to greater understanding of the transition of surface fires to crown fires. With further refinement, simulations could be used to construct threshold models of crown fire transition.



## KEY MILESTONES

### SUB-CANOPY WIND PROFILE MODELLING

- Modelled flow through canopy for both homogeneous and heterogeneous canopies and laid foundation for developing mathematical models for heterogeneous canopies
- Modelled flow through canopy over forested hills under neutral conditions
- Implemented dynamic Wind Reduction Factor in an operational model

### FIREBRAND MODELLING

- Built two firebrand generators for tracking idealised firebrands
- Implemented drag models in the physics-based model to account for different-shaped firebrands
- Validated FDS simulations against experimental data (both non-burning and burning)
- Estimated firebrand generation from a single fir tree burning through inverse modelling

### TREE AND GRASSFIRE MODELLING

- Modelled a grid-converged ROS in grassfire propagation and validated it with experimental data and existing literature
- Investigated ROS in sloping terrain using grassfire model
- Analysed effects of grass height, moisture content on ROS
- Modelled grassfire propagation downstream of a forest canopy
- Simulated surface-to-forest crown fire transition with combination of grassfire and tree burning models



## UTILISATION AND IMPACT

### BACKGROUND

#### Dynamic Wind Reduction Factor (WRF) in an operational model

The behaviour of fire is primarily governed by the wind flow and fuel at the affected locality. In the case of a forest fire, tree canopies play an important role by reducing the wind velocity when it passes through the forest. Fire behaviour analysts use empirical rules of thumb to select a fixed WRF for a specific fuel type for operational fire prediction models. Table 5 represents the WRF used for the McArthur model [14] with PhoenixRapidfire [114] by the Rural Fire Services (RFS), NSW, Australia.

TABLE 5: WIND REDUCTION FACTOR (WRF) GUIDE

Wind Reduction Factor	Vegetation type
1	Herbfield
1.2	Grassland, sedgeland
1.5	Heathland, mallee woodland
2	Tall shrubland (>1.5 m)
2.5	Eucalypt woodland (>6 m)
<b>3</b>	<b>*Open eucalypt forest (standard McArthur forest)</b>
3.5	Shrubby open forest
4 to 5	Damp forest with shrubs, karri
4 to 6	Wet eucalypt forest, mature plantation
5 to 9	Rainforest

\* Note that the present study is based on open Eucalyptus forest only

For a dynamic fire passing through a variable canopy (in height and density), the relationship between the wind speed and ROS appears more complicated than can be described by a constant value, as illustrated by Moon *et al.* [15] and Sutherland *et al.* [115]. Although research on complicated fire–canopy interactions is ongoing, we have improved an operational model for fire propagation applying dynamic WRF [116]. This is the main utilisation of this group’s research.

#### WUI and AS3959

A recent study in the US [117] showed that there has been a significant increase in the WUI, number of WUI houses, and people living in the WUI from 1990 to 2010. Wildfire attack mechanisms at the WUI can be classified into direct flame contact, radiant heat, firebrand attack or a combination of these [17, 118]. Australian Standard 3959 [17, 119] was developed to specify the necessary design for structures located in bushfire-prone areas (BPAs) or the WUI. The intention of AS3959 was to improve the resilience of buildings against bushfire attack (radiant heat, direct flame contact, burning embers, or a combination of



these) to mitigate the risk of bushfire through better adaptability of structures situated in the WUI. While the topic of this utilisation is limited to AS3959, the US standard developed by the National Fire Protection Association (NFPA), NFPA 1144 [120] uses a similar model to prescribe design requirements for structures in the WUI areas of the USA.

There are several drawbacks of AS3959 that have previously been reported [121]. AS3959 is based upon an empirical model for radiation heat load upon the structure. The level of radiant heat flux is used as the basis for the range of bushfire attack levels in AS3959 [119]. Vegetation type, up- or downslope, distance from the site to classified vegetation and Fire Danger Index (FDI, the numerical explanation of the severity of bushfire) are taken into account when determining the Building Attack Level (BAL) [93, 119]. We aimed to assess this empirical model using a physics-based model, FDS. In the first phase, we modelled radiative and convective heat flux from an incoming grassfire to a structure.

Another limitation of AS3959 is the lack of quantified ember loading during a fire event. According to AS3959–2009 and 2018 [93, 119], the firebrand risk in the WUI increases (qualitatively) with the BAL thresholds. Embers are the leading cause of house loss; in the Canberra 2003 fires, 229 houses were destroyed in the suburb of Duffy of which 106 were ignited by embers alone [10]. AS 3959 provides only a small amount of guidance about ember attack increasing with fire danger. Firebrands can ignite barks, leaves, twigs and nuts originating from burning vegetation. Firebrand generation and transport vary mainly by vegetation type, fuel load, humidity (RH), temperature and wind conditions. Spot fires can occur once firebrands land on a fuel bed or combustible part of a structure. Fire intensity, moisture content, characteristics of vegetation and wind velocity determine the firebrands tearing off from vegetation while their size, shape and wind conditions can affect spotting distance [122, 123].

The physics-based FDS model can introduce Lagrangian particles that can be used to represent firebrands. The model consists of Lagrangian particle tracking schemes to resolve firebrand transportation, size and mass distribution, momentum and energy transfer to and from particles of complex objects that cannot be solved on a numerical grid [124]. In pp. 21–24, we present an inverse analysis to obtain the firebrand generation number, initial velocity and direction. For utilisation, Pyrosim software [125] was then used to design a house with proper architectural features. We aimed to investigate firebrands landing on a designed house as well as heat flux under various driving wind velocities. The goal of this phase was to quantify firebrand and heat flux on the designed structure with an aim to improve AS3959.

## IMPLEMENTATION

### Dynamic Wind Reduction Factor (WRF) in an operational model

To apply a dynamic WRF in an operational wildfire prediction model, we implemented a mathematical model that calculates the WRF from leaf area density (LAD) data. We prepared raster maps of leaf area index (LAI) to provide inputs to SPARK, an operational wildfire simulation framework developed by CSIRO Data61, to get LAD for our model to calculate WRF. Further, we applied actual canopy height of the vegetation at various locations to derive LAD to calculate WRF.





Figure 13 shows that the sub-canopy wind profile simulated by FDS is close to the Harman–Finnigan mathematical model [16], which is an ordinary differential equation. Therefore, for simplicity, the Harman–Finnigan model was implemented in SPARK. This is a three-layer model for flow within and above a uniformly distributed tree canopy:

1. Sub-canopy – the Inoue Model [82] is used for sub-canopy flow within the canopy
2. Shear layer across the top of and immediately above the canopy – the Raupach Model [126] is used, and
3. Displaced log-layer above the canopy.

The LAI of a forest canopy and prevalent wind velocity are two parameters of this model. Taking these two parameters into consideration, we first obtain sub-canopy wind profiles (as shown in Figure 40) using the Harman–Finnigan model [16]. We then calculate the WRF by taking the ratio of open wind speed 10 m above the ground ( $U_{10}$ ) and sub-canopy wind velocity at various height ( $u(z)$ ) as shown in Equation (16).

$$WRF = \frac{U_{10}}{u(z)} \tag{16}$$

In our preliminary study, we generated WRF (as shown in Figure 40(a)) from synthetic data to model the varying wind velocity. Figure 40(b) and (c) show the profile of sub-canopy wind and open wind, respectively, based on the Harman–Finnigan model.

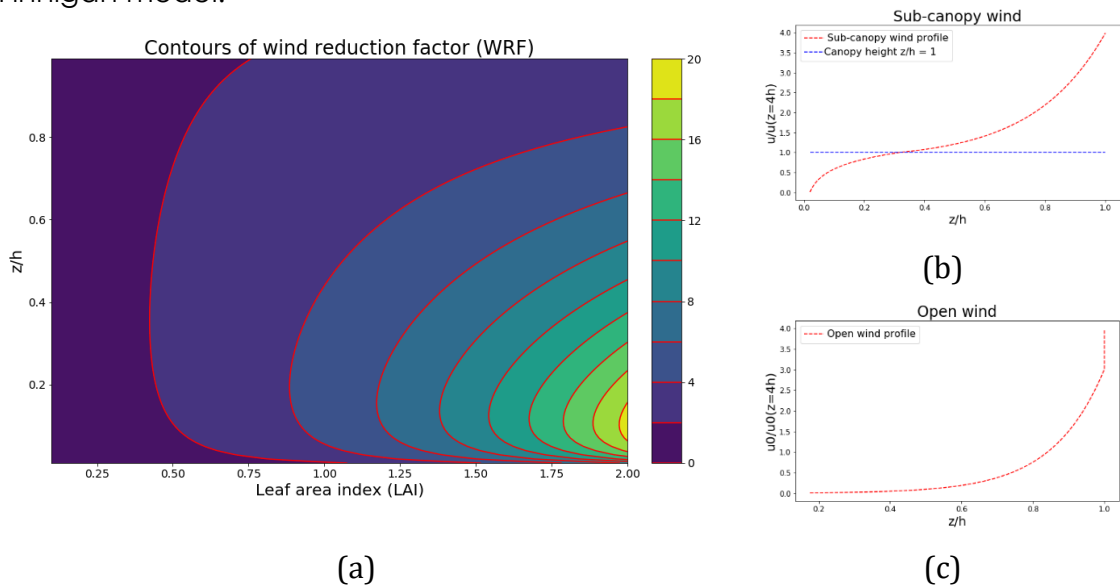


FIGURE 40: PROFILES FOR CALCULATING WRF. (A) A MAP OF WRF DERIVED FROM SYNTHETIC DATA USING THE HARMAN–FINNIGAN MODEL; (B) AND (C) ARE THE PROFILE OF SUB-CANOPY WIND AND OPEN WIND, RESPECTIVELY, BASED ON THE MODEL.

We then implemented Figure 40(a) into CSIRO Data61's operational platform, SPARK. The wind reduction factor was calculated within SPARK. The LAI is relatively easily available from *Landscape Data Visualiser* [127]. We prepared raster maps of LAI to feed into SPARK (an example is shown in Figure 41). To validate the use of WRF, we ran our model with dynamic WRF on six different cases. We calculated the dynamic WRF based on the recorded LAI of the year



previous to the incidents of the respective cases, and extracted LAI of the affected areas bounded by the longitudes and latitudes of those regions.

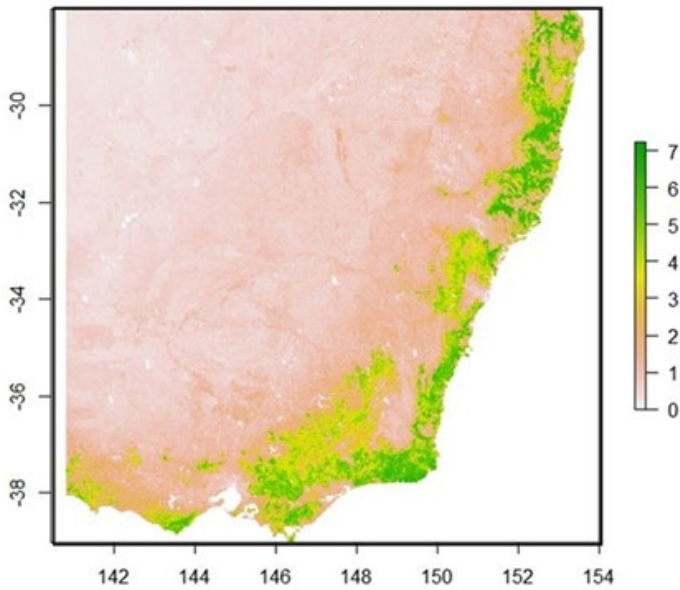


FIGURE 41: RASTER MAPS OF LEAF AREA INDEX: LAI MAP OF NEW SOUTH WALES, AUSTRALIAN CAPITAL TERRITORY, AND VICTORIA BASED ON 2012 LANDSCAPE VISUALISATION DATA [127].

Then, we downloaded Australian vegetation height data from the *Vegetation Height for Australia (Simard)* dataset [128]. We prepared raster maps of the vegetation height data to obtain canopy heights of the regions of the incidents. A visual representation of the canopy height data is shown in Figure 42, depicting canopy height over Australia ranges from 0 to 40 m and mainland Australia has the shortest canopies.

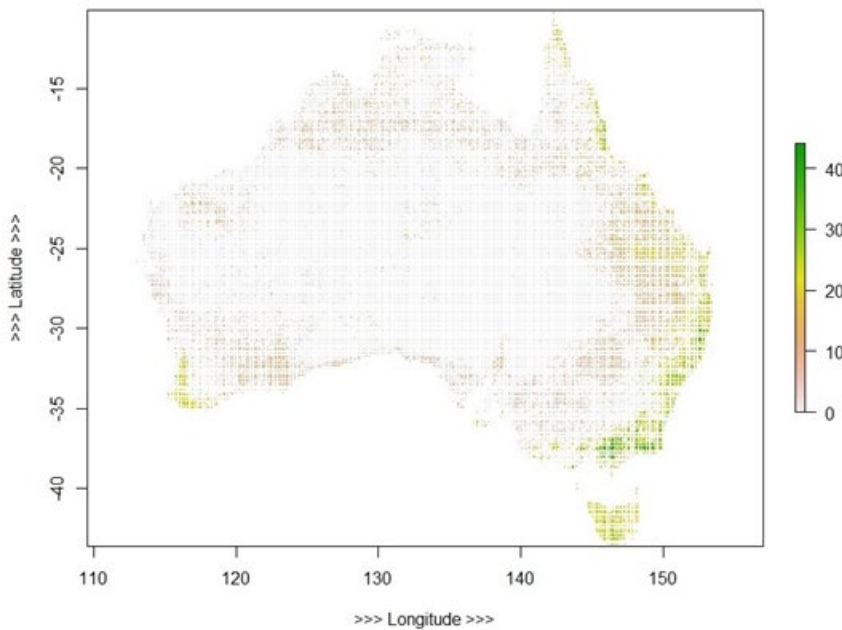


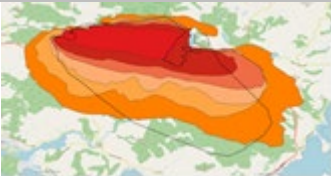
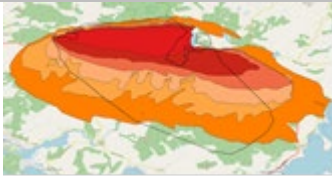
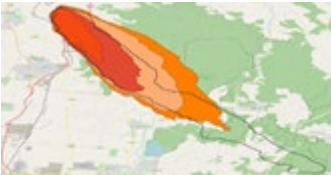
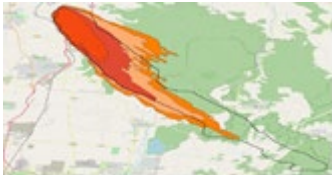
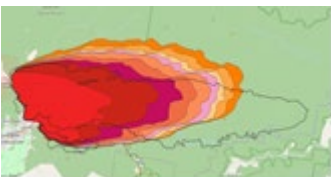
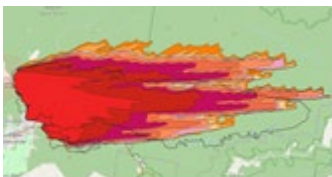
FIGURE 42: CANOPY HEIGHT MAP OF AUSTRALIA BASED ON VEGETATION HEIGHT FOR AUSTRALIA (SIMARD) [128]. VEGETATION HEIGHT WAS MEASURED USING A SATELLITE-BASED LIGHT DETECTION AND RANGING (LIDAR) SYSTEM BETWEEN 20 MAY AND 23 JUNE 2005. AUSTRALIAN DATA WAS GENERATED USING A REGRESSION TREE APPROACH TO MODEL CANOPY HEIGHT. THE SIMULATION WAS RUN AT 1-KM SPATIAL RESOLUTION WITH A VERTICAL ROOT-MEAN-SQUARE ERROR OF 4.4 M.



### Case studies apprising implementation

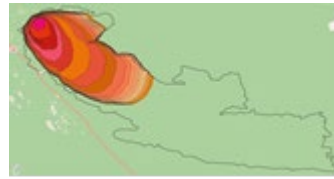
To validate the effectiveness of dynamic WRF, we ran our model on the following six cases:

- **Forcett 2013, Tas.** The ignition caused by a campfire started at 14:00 on 3 January 2013 and remained active until 18 January 2013. This fire burned 23,960 ha with a perimeter of 310 km [129].
- **Kilmore East 2009, Vic.** Ignition time: approximately 11:45 am on 7 February; cause: powerline spark. The fire was fanned by extreme northwesterly winds, and travelled 50 km southeast in a narrow fire front.
- **Linksview 2013, NSW.** The fire began in Springwood on 17 October and spread to Winmalee and Yellow Rock, destroying 185 homes. Burned area: 118,000 ha.
- **Lithgow 2013, NSW.** The State Mine fire started as a minor fire on 16 October 2013 near a Defence Force training base at Marrangaroo, and travelled up to 25 km on 17 October. The fire burnt out more than 55,000 ha between Lithgow and Bilpin.
- **Mount Cooke 2003, WA.** On a warm, dry day in January 2003, a lightning strike sparked a wildfire that burnt through more than 18,000 ha over 3 days, making it one of the largest wildfires ever recorded in the northern jarrah forest [130].
- **Pickering Brook 2005, WA.** Wildfire burnt 27,700 ha of jarrah (*Eucalyptus marginata*) forest in the Pickering Brook area of the Perth Hills during January 2005 [131].

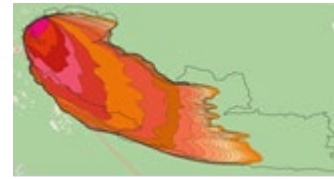
• Case	Base SPARK	SPARK with Dynamic WRF
Forcett 2013, Tas		
	(a1)	(b1)
Kilmore East 2009, Vic		
	(a2)	(b2)
Lithgow 2013, NSW		
	(a3)	(b3)



Mount Cooke  
2003, WA



(a4)



(b4)

FIGURE 43: FOUR CASES WITH GOOD AGREEMENT WITH OUR PREDICTIONS. THE SET A1, A2, A3 AND A4 REPRESENTS THE OUTCOMES OF BASE SPARK BEFORE APPLYING OUR DYNAMIC WRF MODEL. THE SET B1, B2, B3 AND B4 REPRESENTS THE OUTCOMES OF SPARK AFTER APPLYING OUR DYNAMIC WRF MODEL. THE GREY LINES REPRESENT THE ACTUAL RECORDED FIRE PERIMETER.

The common metric of sub-canopy wind speed is the 'mid-flame' wind speed; however, the existing approach for estimating mid-flame speed has significant shortcomings [132]. We are unsure what the actual flame height was during these fires. Therefore, we ran a set of simulations for each case by varying the mid-flame height. The sub-canopy height is not an input of the model; it varies with the input value of canopy thickness (H), also known as vegetation height. To determine the appropriate mid-flame height (h), we ran 50 variants of each case with h values from 1% to 50% of H by increments of 1%. A 50% limit was considered as we are considering sub-canopy flames, i.e. flames do not rise above the canopy top. For the majority of the cases, we observed that h values close to 50% produced better simulation outcomes. Therefore, the results presented in Figure 43, Figure 44, and Figure 45 are based on  $h = 50\% H$ .

The extent of the Mount Cooke, Kilmore and Lithgow fire progressions are better predicted than the Base SPARK simulation (see Figure 43). Base SPARK refers to SPARK without implementation of dynamic WRF. The Mt Cooke fire results show a massive improvement. The extent of the Forcett and Pickering Brook fires (see Figures 43–44) appears to be in agreement when static (Base SPARK) and dynamic WRF is used. Perhaps the vegetation type is a eucalyptus forest, similarly to the conditions where the McArthur model was derived, because it implies that the WRF is not changing much from the default value of 3.

The Linksview fire is poorly predicted with both Base SPARK and SPARK with the dynamic WRF (Figure 44). This suggests that there are other factors, such as wind speed and direction, that may be poorly estimated and affecting the predictions.

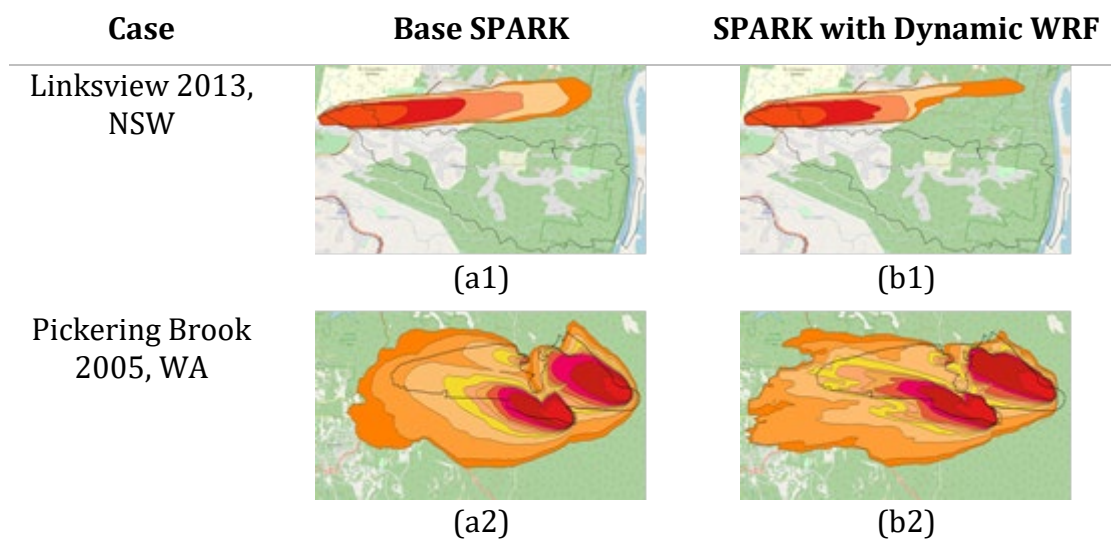


FIGURE 44: TWO CASES EXHIBITING POOR PREDICTIONS. THE SET A1 AND A2 REPRESENTS THE OUTCOMES OF BASE SPARK BEFORE APPLYING OUR DYNAMIC WRF MODEL. THE SET B1 AND B2 REPRESENTS THE OUTCOMES OF SPARK AFTER APPLYING OUR DYNAMIC WRF MODEL. THE GREY LINES REPRESENT THE ACTUAL RECORDED FIRE PERIMETER.



Based on actual fireline data, we prepared comparative spread rate (in terms of area burned) results, shown in Figure 45. In the case of the Kilmore, Lithgow, and Forcett fires, the simulated fires are moving faster than the actual fire. In the Kilmore and Lithgow fires, ROS is faster in Base SPARK that SPARK with dynamic WRF; however, for the Forcett fire, ROS is faster in SPARK with dynamic WRF that in Base SPARK.

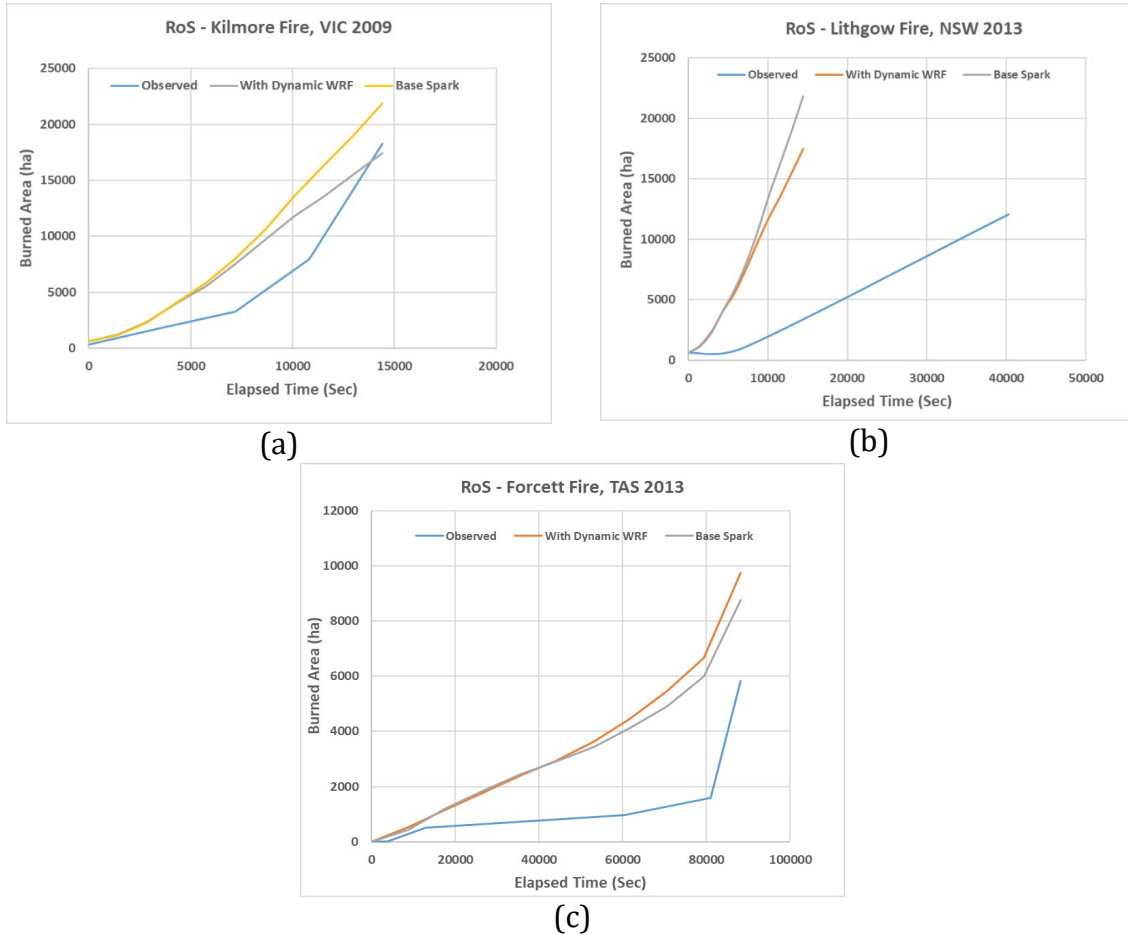


FIGURE 45: COMPARISON OF FIRE ROS BETWEEN SIMULATED FIRES AND THE ACTUAL OBSERVED FIRE LINES FOR KILMORE, LITHGOW AND FORCETT FIRES.

## Output Title: Dynamic WRF for wildfire spread prediction

### Output description

Application of dynamic WRF in predicting fire rate of spread will help fire management authorities to analyse the behaviour of fire more accurately before allocating resources to mitigate the fire. We have completed our initial studies and developed a software module to implement the dynamic WRF in the operational model SPARK. Similar modules can be developed and implemented in other operational models such as Phoenix and Australis.

### Extent of use

- Better WRF calculation will provide better ROS predictions.
- This tool is easy to use. Fire behaviour analysts will be able to use it for better resource allocation planning; they can also get upfront information about WRF if they want to use static WRF.



- In future, this application can be improved with realistic LAD data facilitated by lidar data or sources that calculate LAD profiles in Australia.

#### Utilisation potential

- Accurate calculation of WRF as well as ROS is vital for fire agencies to monitor fire spread in a real fire event.
- Knowing the spread with confidence will help better management strategies and fire suppression.

#### Utilisation impact

- Will help save lives and properties.
- Allows improved utilisation of software to monitor a real wildfire event.
- Can be helpful in association with existing tools.

#### Utilisation and impact evidence

- Using actual case studies, we have demonstrated that dynamic WRF can better predict the extent of fire progression.

### Assessing AS3959 and field-scale firebrand modelling

#### Heat load on structure

With expertise gained in grass and forest fire simulations with physics-based models (WFDS, FDS and FIRESTAR3D), simulations were performed following the criteria outlined in the building standard AS3959 [119]. The case simulation, published in *Frontiers in Mechanical Engineering* [133], was designed to replicate the AS3959 grassland (tussock moorland) fire as closely as computationally feasible. That is, a straight-line fire approaching a small cuboid structure was simulated and the radiative heat flux at the front face of the structure was analysed as a function of distance from the fire front to the structure (Figure 46). The AS3959 standard is based upon the radiative heat flux received at the structure. The Standard sets several Bushfire Attack Levels (BALs); the BAL is the radiative heat flux permitted if the fire is at specific distance from the structure. Owing to computational constraints, the width of the simulated fire is 20 m instead of the 100 m outlined in the Standard.

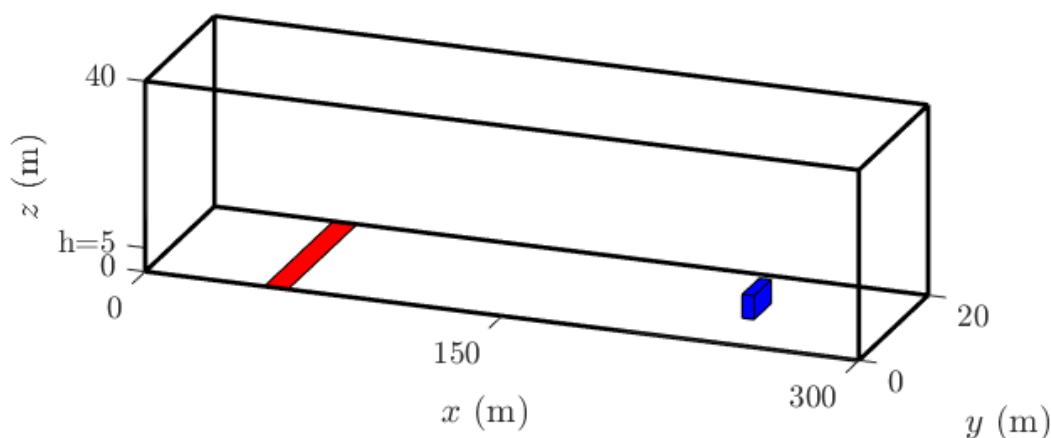


FIGURE 46: THE SIMULATION DOMAIN SHOWING THE LINE IGNITION SOURCE (RED) AND THE HOUSE STRUCTURE (BLUE).



The heat load simulated following AS3959 as closely as possible is compared with the AS3959 BAL predictions. The radiative and convective heat fluxes received on all surfaces of the structure as a function of fire front distance from the structure are shown in Figure 47. Because the fire location moves over time, the distance between the fire and the structure changes in time, and as AS3959 quantifies BAL in terms of distance and different fire parameters lead to different ROS, these plots are made with respect to fire distance, rather than time.

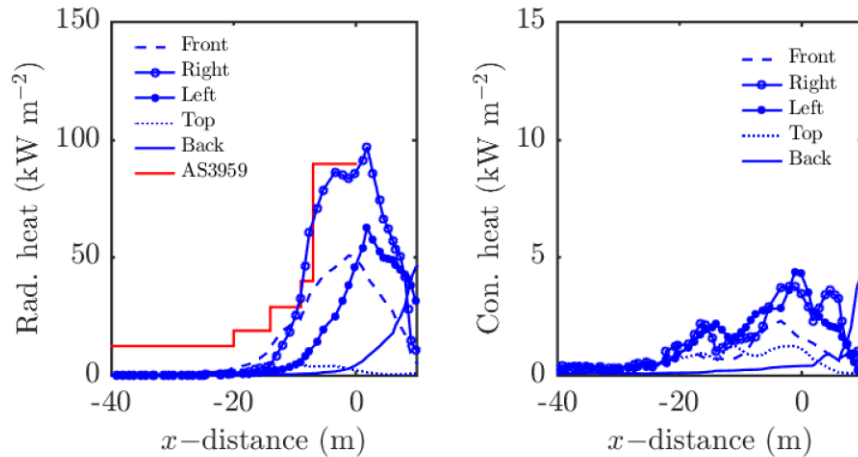


FIGURE 47: RADIATIVE (LEFT), AND CONVECTIVE (RIGHT) HEAT ON THE STRUCTURE FOR THE BASE CASE. THE DISTANCE IS MEASURED TO THE CENTRE OF THE PYROLYSIS REGION.

The heat flux on the front surface increases most quickly as the flame makes contact with the structure. The heat flux on the rear surface increases after the fire has passed the structure. The heat fluxes on the left and right sides both increase at the same distance (approximately  $-10$  m) but the peak radiative heat load on the left-hand side is much greater than on the right-hand side and on the front. The asymmetry is likely due to a complicated wake behind the structure that leads to intensification of the fire on one side. While this phenomenon is interesting, a full investigation is beyond the scope of the present study. Furthermore, the peak of radiant heat flux when the fire is in direct contact with the structure is not important because the structure will likely ignite. The radiant heat flux at the top of the structure is minimal because the top surface is flat and not exposed to the flame.

The convective heat flux on the structure is approximately an order of magnitude less than the corresponding radiative heat flux on the structure and therefore negligible in terms of BAL in this case. However, this does not imply that the convective heat load on the structure is always negligible nor that the increased wind load due to the convective plume can be neglected.

The total heat flux, that is the sum of radiant and convective heat fluxes, and radiation heat flux on the front face are shown in Figure 48 to show the relative contribution of convective heat load. The simulated heat flux follows the same trends as the BAL model; however, BAL-12.5 and BAL-19 are apparently excessive. That is, the Standard predicts heat flux far greater (2 to more than 10 times) than the simulated heat flux. The BAL-29 and BAL-40 regions agree with the simulation results. Recall that the simulated fire is one fifth the width of the fire modeled in AS3959. The radiant heat load can be expected to increase with increasing fire width. Therefore, while the simulation results may apparently support the model in the Standard, the simulated heat flux from a 100-m wide

fire will likely exceed the Standard. Although this discrepancy could be severe, the Standard could be revised fairly easily. The BAL regions are fairly narrow, so the regions could be made wider to accommodate larger anticipated heat fluxes.

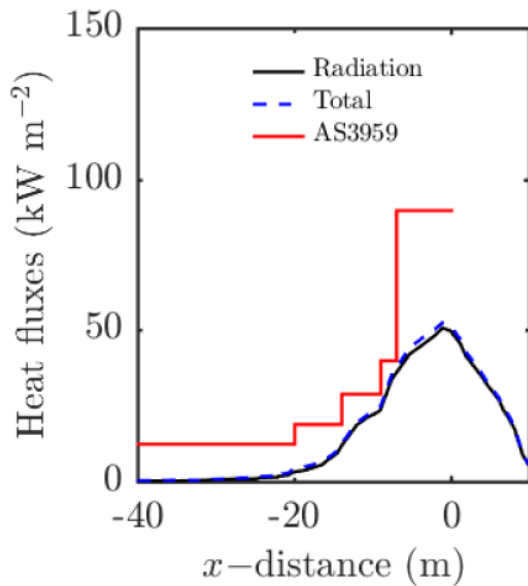


FIGURE 48: COMPARISON OF MODELLED HEAT LOAD WITH AS3959 DATA.

Similar studies can be conducted for all fuel classes and FDIs given in AS3959 with a 100-m wide flame front. We could also conduct risk mapping from multiple fire fronts, on sloping terrain, etc.

#### Firebrand modelling at forest edges

This field-scale simulation seeks to demonstrate the potential to develop a statistical model of the transport of ember particles across realistic forest edges for operational use. Such a model will inform scientifically sound forecasts of ember risk from bushfires. Improved forecasts will mitigate the potential risks posed by embers to human lives and properties on the WUI.

We simulate the transport of ember particles away from a modelled fire within a forest canopy. The particles are tracked across the forest edge and the distributions of embers on the ground are characterised by mean and variances in the  $x$  and  $y$  directions. Different ember shapes are simulated to understand how ember shape affects the spotting distance and lateral dispersion of embers. The computational domain used in this study is shown in Figure 49(a). The simulation domain is 1000 m long, 160 m wide and 80 m high. The forest canopy starts at  $x = 250$  m, and is 250 m long, 160 m wide and 17 m high. It is modelled as a region of aerodynamic drag, where the drag force varies with the leaf area density (LAD) profile [19]. We used the LAD profile of the open woodland forest category measured by Moon *et al.* [15] as presented in Figure 49(b).



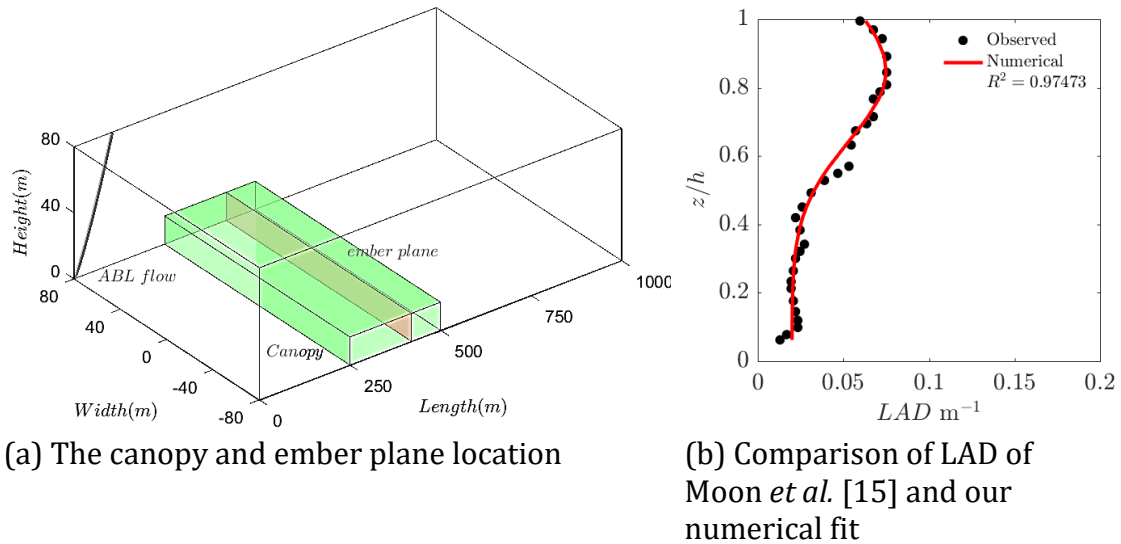


FIGURE 49: COMPUTATIONAL DOMAIN WITH CANOPY AND EMBER PLANE LOCATION AND LAD PROFILE.

An ember generation plane is defined at 170 m inside the canopy, highlighted in red in Figure 49(a). A stationary fire is modelled at the base of the ember generation plane by a region of specified fire intensity at 4714.6 kW/m. The intensity of fire is determined from the data provided for dry sclerophyll eucalyptus by Cruz *et al.* [18]. Two shapes of ember particles of density 225 kg/m<sup>3</sup> are ejected from the ember plane: (a) square disc, and (b) cylindrical.

The simulated wind field is allowed to develop to a statistically steady state for a simulated time of 1 hour, before particles are injected. Once the background flow is steady, 1000 ember particles of each shape and size are injected on the ember plane.

The ember distributions for the embers originating in the crown section of the forest canopy are presented in Figure 50 for the cylindrical and square examples. The lateral dispersion of ember particles is computed as the signed difference between the final and initial y locations of the particle, so the mean distance in the y direction (lateral dispersion) is zero. The bivariate probability distribution function (pdf) of cylindrical embers is estimated from the histogram of final ember location normalised so that the volume under the surface is one. The pdf of embers shows only the first impact location on the ground; bouncing of ember particles is not considered.

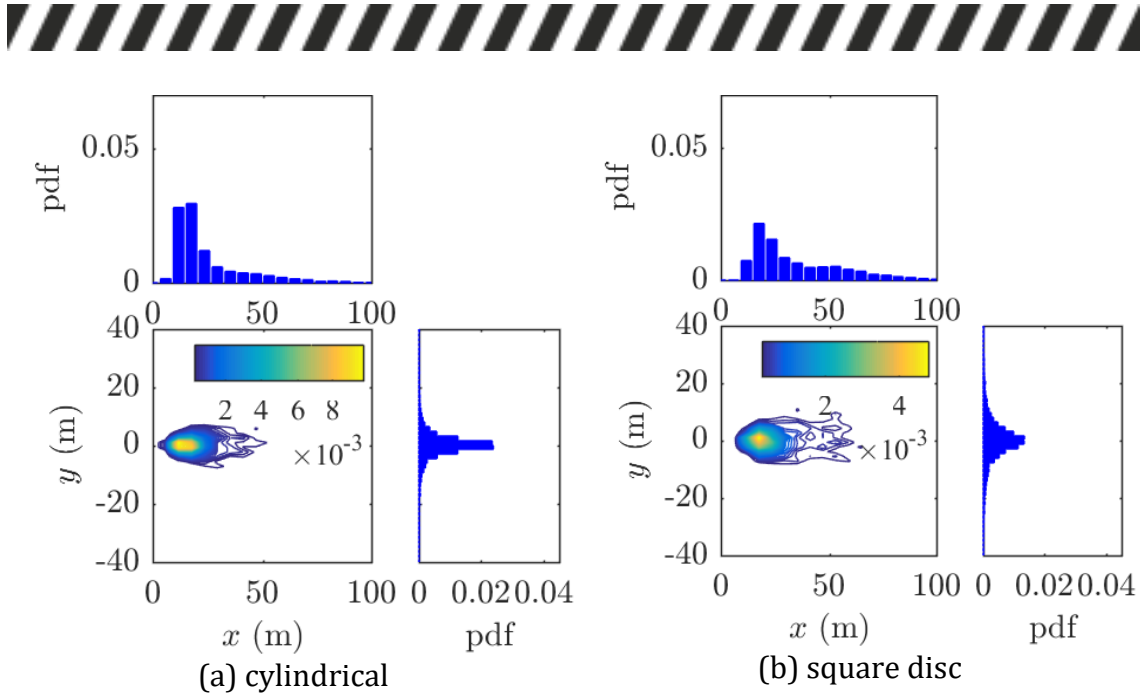


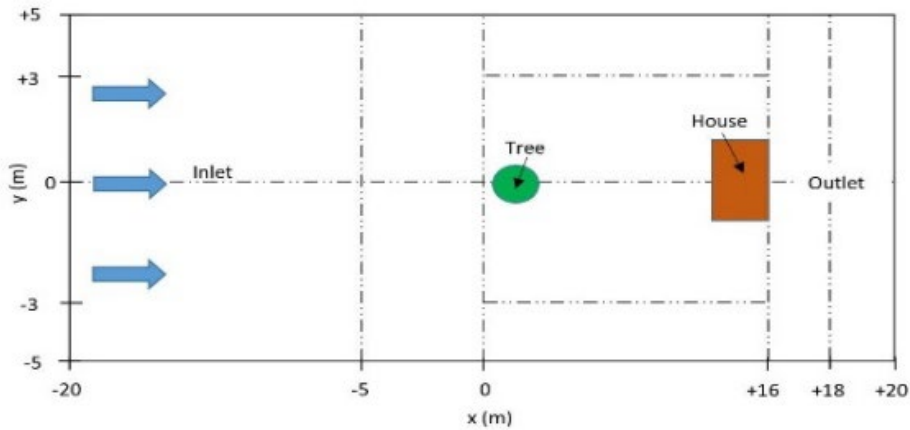
FIGURE 50: SPATIAL DISTRIBUTION FOR CYLINDRICAL AND SQUARE DISC EMBER PARTICLES AT INITIAL TEMPERATURE OF 41.1°C (PDF: PROBABILITY DISTRIBUTION FUNCTION).

The marginal pdfs in the  $x$  and  $y$  directions are computed by summing the bivariate pdf in the  $y$  and  $x$  directions respectively. The contours of the bivariate pdf, the  $x$  and  $y$  marginal distributions of cylindrical embers are shown in Figure 50(a) and for the square disc particles ( $32 \times 2$  mm) in Figure 50(b). The observations show that cylindrical ember particles are more concentrated compared with square disc ember particles, as can be seen from the colour scale. The distributions of embers in the  $x$  direction are observed to be qualitatively similar with the field study in Project Vesta for short-range embers [134].

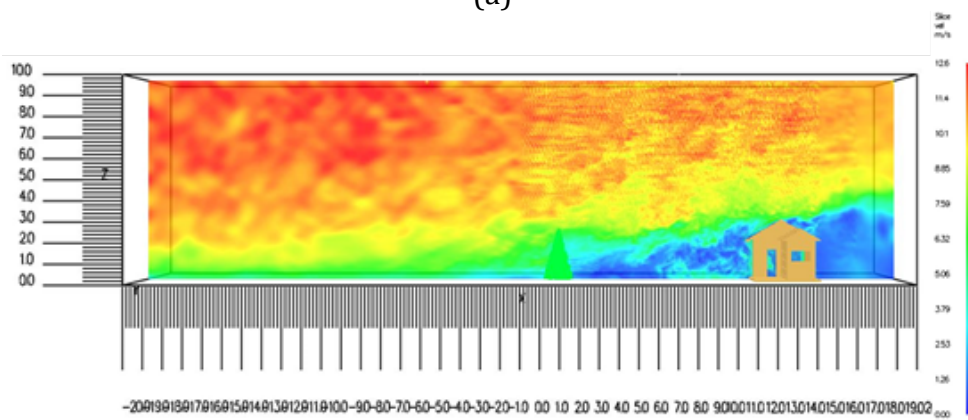
#### Mapping firebrand flux and heat load on structures in the context of AS3959

Besides use in statistical model development for firebrand landing distribution, we also aimed to map firebrand flux and heat load on structures. It should be noted that in AS3959-2009 [93], a radiation heat flux threshold is prescribed, but no quantification is given in terms of firebrand flux. The mapping the firebrands and heat flux on structures is essential to determine wildfire risks and prepare strategic plans to mitigate the hazard.

We have commenced physics-based simulations of heat flux and firebrands landing on a designed house, initially with firebrand transport from a single tree towards a simulated house. The input number, direction and velocities of firebrands are taken from an inverse analysis of a firebrand distribution experiment from a single tree burning conducted at NIST [40]. The house is designed with proper architectural features such as walls, doors, windows and roof using Pyrosim software. Wind fields of  $U_{10} = 3, 6$  and  $12.5$  m/s are added to examine firebrands landing on the house. A plan view of the scenario is presented in Figure 51(a) and a graphical representation of wind flow with  $12.5$  m/s wind velocity and associated eddies are shown in Figure 51(b).



(a)



(b)

FIGURE 51: (A) PLAN VIEW OF THE SIMULATION DOMAIN. THE AREA (16 × 6 × 10 M) WITH THE BURNING TREE AND FIREBRAND TRANSPORT HAS FINEST GRID RESOLUTION OF 50 MM. (B) GRAPHICAL REPRESENTATION OF THE DOMAIN IN SMOKEVIEW WITH 12.5 M/S WIND VELOCITY AND EDDIES INTRODUCED BY SYNTHETIC EDDY METHODOLOGY (SEM) [135].

However, in this simulation, no firebrand has reached the house. This is because of the low height of the tree (2.6 m) and insufficient fire-induced buoyancy to lift the firebrands high enough to be transported by the wind field. The peak radiant heat flux obtained in different strategic locations (numbered 1 to 9) of the house at different driving wind velocities is computed and presented in Figure 52(a). The maximum radiant heat flux is observed at the centre of the front wall (2), which is the closest point to the burning tree. The minimum radiant heat flux is observed at the corner by the door (4), which is not exposed much compared with other locations.

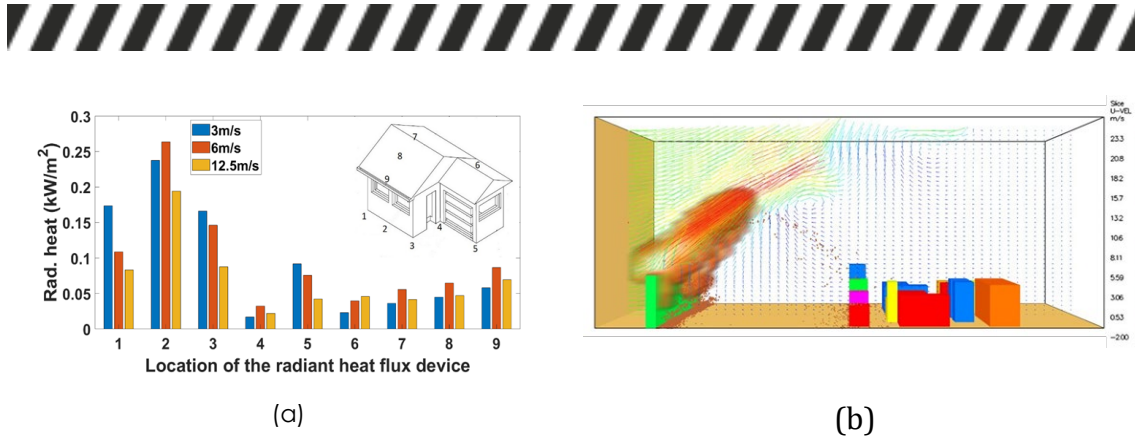


FIGURE 52: (A) LOCATION SPECIFIED PEAK RADIANT HEAT FLUXES OBTAINED BY THE HEAT FLUX DEVICES IN FDS FOR 3, 6 AND 12.5 M/S WIND VELOCITIES. (B). A SMOKEVIEW REPRESENTATION OF FIREBRANDS LANDING ON STRUCTURES MODELLED IN FDS. FIREBRANDS ARE RELEASED 5 M HEIGHT ABOVE THE GROUND AND TRANSPORTED BY A 13 M/S WIND FIELD AND FIRE-INDUCED BUOYANCY [136].

Figure 52 (b) is an illustration of firebrands landing on structures modelled in FDS with a wind field of 13 m/s, canopy height of 5 m and fire intensity of 18,640 kW/m, which are higher than in Figure 51. It can be seen that a number of firebrand particles are landing on the structures under the influence of the wind field, fire buoyancy and elevation of the firebrand ejection.

Firebrand landing and heat flux on structures are currently being examined further with clusters of vegetation – forests, scrub, and mallee/mulga – under different fire danger indices (FDI) and atmospheric conditions as per AS3959 [119] and with previous detailed studies [41] within this research group. FDIs of 50, 80 and 100 are being used as these numerical values cover the top range of jurisdictional and regional fire danger indices from very high to extreme bushfire conditions in Australia [93, 137].

### Extent of use and utilisation potential

It has been demonstrated that physics-based simulations can be used to study short-range ember transport from a fire at the field scale. Future utilisation work will investigate the landing distribution of embers emanating from various forest classes and types listed in AS3959 and will lead to operational models for short-range ember transport.

The hazard quantification of firebrands and heat fluxes (both convective and radiative) is a key parameter for risk assessment in the WUI. We hope that such quantification through physics-based modelling will assist in improving the existing AS3959 standard as well as promoting performance-based building designs in bushfire-prone areas to better counter wildfire risk. Further utilisation includes developing an engineering model based on evaluating the effect of high volumes of firebrands landing on structures [138-140] and their ignition propensity.



## CONCLUSION

### SUMMARY

Fire spread across fuel types is a complex area of research involving wildland fire spread, intensity of fire, plume formation, spot fires, and complex turbulent wind flow in flat and sloping terrains. Understanding accurate ROS is a difficult task as the science behind this involves many physical processes, such as combustion of solid fuels, wind flow, moisture content and vegetation types. Those physical processes cover a vast number of disciplines in science and engineering, such as combustion chemistry, fluid dynamics, thermodynamics and the statistics of random particle transport. Two physics-based models, FDS and WFDS, were developed by NIST based on those branches of engineering without compromising the physics itself in the form of empirical characterisation. Victoria University is applying these fully physics-based modelling (FDS and WFDS as well as FireSTAR3D developed by Aix-Marseille University, France) approaches and experimental studies to address the science behind complex fire spread. This physics-based modelling approach is gradually being explored in North America and Europe for ROS prediction and analysis of complex fire at various scales.

Flow through forest canopies is one of the complex modelling areas that we have made significant advances in by implementing a canopy drag model in FDS source code [141]. We found that the simple sub-canopy wind model of the Harman-Finnigan model gives a similar wind profile to that obtained through LES modelling using FDS. We went on to implement the Harman-Finnigan model to generate a dynamic wind reduction factor (WRF) in the operational model SPARK. Using six real-fire case studies, we have demonstrated that a dynamic WRF generally provides better fire propagation predictions than a fixed WRF. We also conducted LESs of wind flow through horizontally and vertically heterogeneous canopies. These simulations show interesting flow features that can be parameterised for operational models with further intensive studies. These flow characteristics not only affect fire propagation but can also affect firebrand transport. The sub-canopy wind flow study was further extended for flow in canopy-covered hills. In terms of utilisation, this is the area where maximum progress has been made.

Two firebrand generators were designed and constructed at Victoria University and we conducted idealised firebrand landing experiments for different firebrand sizes and shapes. These experimental results were used to validate a Lagrangian particle-based FDS model and satisfactory validation was obtained. Firebrand modelling is critically important to improve our understanding of ember transportation. We then carried out a set of simulations on how embers disperse at the field scale from a realistic forest edge, and conducted an inverse analysis to quantify firebrand generation from a single burning tree. This firebrand generation was used as a source term for modelling ember transportation from a tree towards a house. This work is ongoing.

Grassfire simulation has been the most successful area in terms of journal publications. The benchmark simulation of the grassfire model of Moinuddin *et al.* [2] was published in the *International Journal of Wildland Fire*, extending the previous work of Mell *et al.* [28] with inclusion of a grid-converged study, and comparing the results with the MK3 and MK5 versions of the MacArthur model and the CSIRO model. The study has been extended to assess the effects of grass



height, relative humidity of air, slope of the terrain and presence of forest canopy upstream of a grassland. We have also successfully modelled transition of surface fire to forest crown fire.

With the success of grassfire, tree fire, crown fire and firebrand transport modelling, we have commenced simulation of hazard mapping on structures in the WUI in terms of heat flux (radiative and convective) and firebrand flux. This is aimed at improving the existing AS3959 standard as well as promoting performance-based building designs.

As part of its CRC engagement, Victoria University in collaboration with other universities has achieved major breakthroughs in developing and using physics-based models. It has been demonstrated that physics-based models can be valuable tools in understanding fire spread across different fuel types and providing insight and improvement to operational models. Victoria University has developed state-of-the-art research expertise in bushfire research. All stakeholders, in particular fire agencies, can utilise this expertise for modernising their fire management activities.

## NEXT STEPS

We successfully completed the second phase of the project (2017–2020) covering many areas of research related to the project *Fire Spread Across Fuel Types*. We have commenced utilisation phase of some of our work, as explained in the *Utilisation* section. We want to include more areas for future utilisation targeting the needs of the end-users while continuing research on high-impact science. There are very few researchers around the world involved in bushfire research, especially in Australia. Here, we are one of few groups involved in physics-based simulation by investigating the science behind bushfire spread in different vegetation types, flow through homogeneous and heterogeneous forest canopies and firebrand generation and transportation. The BNHCRC decided to fund this research project because it recognised that Australia was lagging behind the rest of the world in physics-based modelling. We have built capacity in both experimental and simulation studies. Our expertise includes advanced computer programming, setting up realistic fire scenarios, modelling with fidelity, postprocessing of data and presenting results to a wide range of audiences. Physics-based modelling research can be expanded to many practical areas where the innovative outcomes would be valuable for saving lives and properties. Some prospective research areas are discussed below.

### Dynamic fire development

We are aiming to expand our studies on dynamic fire development to more complex cases involving fire on slopes, hilly terrains and canopy-covered hills, investigating merging fire behaviour, finding threshold conditions for transitioning from surface to crown fire, assessing the effectiveness of fuel breaks, simulating plumes in different atmospheric conditions, etc. Fire–atmospheric interaction is an important area of research to which we can contribute to a greater extent in the future. At the moment, we have carried out work on atmospheric stability cases with inclusion of canopy drag and heat sources. However, atmospheric stabilities have a greater role in plume formation, which trigger many extreme fires and natural hazards. An advanced physics-based plume model could provide insight into fire behaviour under such atmospheric conditions.



### Flow through forest canopy

We incorporated vegetation configuration to calculate WRF for Australian forest canopies for operational models. In this, we used LAI values to calculate WRF with idealised LAD profiles. In future, we want to include real LAD profiles, which will provide more accurate and realistic WRFs. In the physics-based simulation, we will expand our studies of heterogeneous canopy, forest clearing, upslope, downslope and hilly terrain situations.

### Firebrand module for operational model

The FDS validated firebrand sub-model can be used in many studies related to the transportation of firebrands in real-fire scenarios. We aim to conduct further studies on firebrand generation, transportation, landing distribution and spotting. This will lead to development of a statistical firebrand module for landing to be included in operational models such as SPARK. Through physics-based modelling, we will also be able to quantify the contribution of firebrand showers in the growth of a fire front through spotting and increment of the rate of spread.

### Risk management and AS3959

For vulnerability mapping of buildings and structures in the WUI, we aim to conduct firebrand modelling for different classes and types of forests to include firebrand flux in the quantification of bushfire attack levels (BALs). This will be accompanied by estimating heat flux from the fire front and the contribution of radiation and convective heat flux. We will be able to check whether the prescriptive limit given in AS3959 is valid. Overall, we wish to address the limitations of the existing BAL quantification with a realistic assessment of actual heat flux due to both radiation and firebrand heat flux. In terms of risk mitigation, water-based suppression systems can be very useful for individual building fires. FDS is capable of modelling fire suppression by sprinkler and water mist. Research could be conducted to test the efficacy of such suppression measures with various configurations in saving houses in WUI.

On a final note, we are collaborating with domestic and international research groups to expand the capability of physics-based simulation, which will provide more open-ended research and innovation opportunities in Australia. Our utilisation works backed up by science-based understanding and knowledge should be invaluable to operational management in mitigating bushfire events.



## PUBLICATIONS LIST

### PEER-REVIEWED JOURNAL ARTICLES

- 1 MacDonald, M., Chan, L., Chung, D., Hutchins, N. & Ooi, A. [Turbulent flow over transitionally rough surfaces with varying roughness densities](#). *Journal of Fluid Mechanics* 2016; 804: 130-161.
- 2 Wadhvani R., Sutherland D., Ooi, A., Moinuddin K. Verification of a Lagrangian particle model for short-range firebrand transport. *Fire Safety Journal* 2017; 91: 776-783.
- 3 Wadhvani R., Sutherland D., Moinuddin K. Kinetics of pyrolysis of litter materials from pine and eucalyptus forests. *J. Therm. Anal. Calorim.* 2017; 130: 2035-2046.
- 4 Moinuddin K., Sutherland D., Mell W. Simulation study of grass fire using a physics-based model: striving towards numerical rigour and the effect of grass height on the rate of spread. *Int. Journal of Wildland Fire* 2018; 27(12): 800–814.
- 5 Khan N., Sutherland D., Wadhvani R., Moinuddin K. Physics-based simulation of heat load on structures for improving construction standards for bushfire-prone areas, *Frontiers in Mechanical Engineering* 2019; 5: 35.
- 6 Moinuddin K., Sutherland D. Modelling of tree fires and fires transitioning from the forest floor to the canopy with a physics-based model. *Mathematics and Computers in Simulation* 2020; 175: 81–95.
- 7 Sutherland D., Sharples J., Moinuddin K. The effect of ignition protocol on grassfire development. *Int. Journal of Wildland Fire* 2020; 29(1): 70–80.
- 8 Gilbert A., Sutherland D., Frangieh N., Moinuddin K., Shamseddine I., Meradji S., Morvan D. Physics-based simulations of flow and fire development downstream of a canopy. *Atmosphere* 2020; 11(7): 683.

### CONFERENCE PAPERS

- 1 George, N., Ooi, A., Moinuddin, K.A.M., Thorpe, G., Marusic, I. and Chung, D. Direct numerical simulation of a turbulent line plume in a confined region, *Twentieth Australasian Fluid Mechanics Conference*, Perth, 5–8 December, 2016.
- 2 Sutherland D., Moinuddin K., Ooi A. *Large-eddy simulation of neutral atmospheric surface layer flow over heterogeneous tree canopies*. AFAC 2017 pp. 184-199. Bushfire and Natural Hazards CRC, September 2017.
- 3 Wadhvani R., Sutherland D., Moinuddin K. [Suitable pyrolysis model for physics-based bushfire simulation](#). *11<sup>th</sup> Asia-Pacific Conference on Combustion*. 2017 Sydney, Australia.
- 4 Dissanayake, A., Setunge, S., Venkatesan, S., Sutherland, D., Moinuddin, K. [Numerical assessment of composite bridges subjected to Wildland-Urban Interface \(WUI\) fires](#). *Proceedings of the Ninth International Conference on Bridge Maintenance, Safety and Management (IABMAS 2018)* pp. 1247–1255, Melbourne, August 2018.
- 5 Sutherland, D., Philip, J., Ooi, A. and Moinuddin, K.A.M. Simulations of surface fire propagating under a canopy: flame angle and intermittency. In *Advances in Forest Fire Research 2018*. Ed.: Viegas DX. pp. 1303–1307. Imprensa da Universidade de Coimbra, Portugal, 30 Nov 2018.
- 6 Roy, SS., Sutherland, D., Khan, N. and Moinuddin, K.A.M. A comparative study of wind fields generated by different inlet parameters and their effects on fire spread using Fire Dynamics Simulator. *21st Australasian Fluid Mechanics Conference*, Adelaide, Australia, Dec. 2018.
- 7 Sutherland, D., Philip, J., Ooi, A. and Moinuddin, K.A.M. Large eddy simulation of flow over streamwise heterogeneous canopies: quadrant analysis. *21st Australasian Fluid Mechanics Conference*, Adelaide, Australia, Dec 2018.
- 8 Sutherland, D., Wadhvani, R., Philip, J., Ooi, A. and Moinuddin, K.A.M. Simulations of the effect of canopy density profile on sub-canopy wind speed profiles. *AFAC Conference 2018*.
- 9 Moinuddin, K.A.M. and Sutherland, D., Physics based modelling of tree fires and fires transitioning from the forest floor to the canopy. In *Proceedings of the 22nd International Congress on Modelling and Simulation*, Hobart, Australia, Eds: Syme G, Hatton MacDonald D, Fulton B, Piantadosi J. pp 1138–1144. Modelling and Simulation Society of Australia and New Zealand (MSSANZ), 2017.
- 10 Wadhvani R., Sutherland D., Moinuddin K. *Simulated transport of short-range embers in an idealised bushfire*. *6<sup>th</sup> International Fire Behavior and Fuels Conference 2019*, Sydney, Australia.
- 11 Moinuddin, K. & Sutherland, D. Simulations of radiation heat flux on a structure from a fire in an idealised shrubland. *Bushfire and Natural Hazards CRC Research Day AFAC19 (2019)*.

### TECHNICAL REPORTS

- 1 Khan, N., Sutherland, D., Moinuddin, K. [Simulation of flows through canopies with varying atmospheric stability](#). Bushfire and Natural Hazard CRC Milestone Report 2020, Available at <https://www.bnhcrc.com.au/publications/biblio/bnh-6830>.
- 2 Khan, N., Sutherland, D., Moinuddin, K. Recirculation regions downstream of a canopy on a hill. Bushfire and Natural Hazard CRC Milestone Report 2020. Available at <https://www.bnhcrc.com.au/publications/biblio/bnh-6638>.
- 3 Khan, N., Sutherland, D., Philip, J., Ooi, A., Moinuddin, K. A preliminary report on simulation of flows through





- canopies with varying atmospheric stability. Bushfire and Natural Hazard CRC Milestone Report 2019. Available at <https://www.bnhcrc.com.au/publications/biblio/bnh-5477>.
- 4 Wickramashinghe, A., Khan, N., Moinuddin, K. Physics-based simulation of firebrand and heat flux on structures in the context of AS3959. Bushfire and Natural Hazard CRC Milestone Report 2020. Available at [https://www.bnhcrc.com.au/sites/default/files/managed/downloads/simulation\\_of\\_firebrand.pdf](https://www.bnhcrc.com.au/sites/default/files/managed/downloads/simulation_of_firebrand.pdf).
  - 5 Moinuddin, K., Khan, N., Sutherland, D. Effect of relative humidity on grassfire propagation, report 2020. Available at <https://www.bnhcrc.com.au/publications/biblio/bnh-6822>.
  - 6 [Rashid, M.](#), [Hilton, J.](#), [Khan, N.](#), [Sutherland, D.](#), [Moinuddin, K.](#) A report on WRF software development (preliminary), 2020. Available at <https://www.bnhcrc.com.au/publications/biblio/bnh-6642>.
  - 7 Moinuddin, K., Roy, S., Sutherland, D., Khan, N. Improvements to wind field generation in physics-based models to reduce spin-up time and to account for terrain, heated earth surface. Report 2018. Available at <https://www.bnhcrc.com.au/publications/biblio/bnh-4976>.
  - 8 [Sutherland, D.](#), [Wadhwani, R.](#), [Philip, J.](#), [Ooi, A.](#) & [Moinuddin, K.](#) Simulations of the effect of canopy density profile on sub-canopy wind speed profiles. (Bushfire and Natural Hazards CRC, 2018).
  - 9 [Sutherland, D.](#), [Philip, J.](#), [Ooi, A.](#) & [Moinuddin, K.](#) Literature review: modelling and simulation of flow over tree canopies. (Bushfire and Natural Hazards CRC, 2018).
  - 10 [Moinuddin, K.](#) & [Sutherland, D.](#) Numerical modelling of fires on forest floor and canopy fires. (Bushfire and Natural Hazards CRC, 2017).
  - 11 [Moinuddin, K.](#), [Sutherland, D.](#) & [Thorpe, G.](#) Fire spread prediction across fuel types: Annual Project Report 2015–2016. (Bushfire and Natural Hazards CRC, 2016).
  - 12 [Thorpe, G.](#) Fire spread prediction across fuel types: Annual project report 2014–2015. (Bushfire and Natural Hazards CRC, 2015).
  - 13 [Thorpe, G.](#) Fire Spread Across Fuel Types Annual Report 2014. (Bushfire and Natural Hazards CRC, 2014).



## TEAM MEMBERS

The project team leader is Professor Khalid Moinuddin at Victoria University. We have collaborators from the University of Melbourne, Melbourne; UNSW, Canberra; DATA61 CSIRO, Australia; Aix-Marseille University and University of Toulon, France. Details of team members and their present activities are given below.

### RESEARCH TEAM

Prof. Khalid Moinuddin, Victoria University

Dr Duncan Sutherland, UNSW, Canberra/Victoria University

Dr Nazmul Khan, Victoria University

Prof. Andrew Ooi, University of Melbourne

Dr Jimmy Philip, University of Melbourne

Dr Mahmood Rashid, Victoria University

### PHD STUDENTS

Ms Jasmine Innocent, Victoria University

Mr Matthew Kyng, Victoria University

Mr Amila Wickramasinghe, Victoria University

Dr Mahfuz Sarwar, Victoria University (completed)

Dr Michael MacDonald, University of Melbourne (completed)

Dr Rahul Wadhvani, Victoria University (completed)

Dr Niteesh George, University of Melbourne (completed)

### MASTERS BY RESEARCH STUDENTS

Ms Sesa Singha Roy, Victoria University (completed)

### END-USERS

Dr Simon Heemstra, Manager Community Planning, NSW Rural Fire Service

Dr Stuart Matthews, Senior Project Officer, NSW Rural Fire Service

Mr Andrew Stark, Deputy Chief Officer, Country Fire Service South Australia

Mr Lawrence McCoy, Senior Fire Behaviour Analyst, NSW Rural Fire Service

Mr Brad Davies, Senior Fire Behaviour Analyst, NSW Rural Fire Service

Mr Chris Wyborn, Senior Technical Officer, Fire Protection Association of Australia

Mr Mike Wouters, Senior Fire Ecologist, DENS, South Australia

Mr Jackson Parker, Senior Environmental Officer, DEFS, WA



Mr Paul Fletcher, Assistant Chief Fire Officer, SAMFS

Mr Andrew Sturgess, Fire behaviour analyst, Queensland Fire and Emergency Services

Mr Brian Levine, Fire Management Officer, Parks and Conservation Service, ACT

Mr Adam Leavesley, Fire Management Officer, Parks and Conservation Service, ACT



## REFERENCES

- 1 Cruz, M.G. and M.E. Alexander, *Uncertainty associated with model predictions of surface and crown fire rates of spread*. Environmental Modelling & Software, 2013. **47**: pp. 16–28.
- 2 Moinuddin, K.A.M., D. Sutherland, and R. Mell, *Simulation study of grass fire using a physics-based model: striving towards numerical rigour and the effect of grass height on the rate-of-spread*. International Journal of Wildland Fire, 2018. **27**(12): pp. 800–814.
- 3 Sutherland, D., J.J. Sharples, and K.A. Moinuddin, *The effect of ignition protocol on grassfire development*. International Journal of Wildland Fire, 2020. **29** (1): pp. 70–80.
- 4 Ronchi, E., S.M. Gwynne, G. Rein, R. Wadhvani, P. Intini, and A. Bergstedt, *e-Sanctuary: Open multi-physics framework for modelling wildfire urban evacuation*. 2017: Fire Protection Research Foundation Quincy, MA.
- 5 Werner, J. and S. Lyons. *The size of Australia's bushfire crisis captured in five big numbers*. ABC News, Retrieved August 2020. Available from: <https://www.abc.net.au/news/science/2020-03-05/bushfire-crisis-five-big-numbers/12007716>.
- 6 Green, M. *Australia's massive fires could become routine, climate scientists warn*, REUTERS, 2020; Available from: <https://www.reuters.com/article/us-climate-change-australia-report-idUSKBN1ZD06W>
- 7 Boer, M.M., V.R. de Dios, and R.A. Bradstock, *Unprecedented burn area of Australian mega forest fires*. Nature Climate Change, 2020. **10**(3): pp. 171–172.
- 8 Wikipedia. 2019–20 Australian bushfire season, 2020; Available from: [https://en.wikipedia.org/wiki/2019%E2%80%9320\\_Australian\\_bushfire\\_season](https://en.wikipedia.org/wiki/2019%E2%80%9320_Australian_bushfire_season).
- 9 McLeod, R., S. Pascoe, and B. Teague, *The 2009 Victorian Bushfires Royal Commission final report: summary*. Government Printer for the State of Victoria, 2010.
- 10 Bianchi, R. and Leonard, J., *Investigation of Bushfire Attack Mechanisms Resulting in House Loss in the ACT Bushfire 2003*, Bushfire Cooperative Research Centre (CRC) Report, 2005
- 11 Jolly, W.M., M.A. Cochrane, P.H. Freeborn, Z.A. Holden, T.J. Brown, G.J. Williamson, and D.M. Bowman, *Climate-induced variations in global wildfire danger from 1979 to 2013*. Nature communications, 2015. **6**: p. 7537.
- 12 Whittaker, J., K. Haynes, J. Handmer, and J. McLennan, *Community safety during the 2009 Australian 'Black Saturday' bushfires: an analysis of household preparedness and response*. International Journal of Wildland Fire, 2013. **22**(6): pp. 841–849.
- 13 Rothermel, R.C., *How to predict the spread and intensity of forest and range fires*. General Technical Report INT-143. 1983, Ogden, UT: US Department of Agriculture, Forest Service, Intermountain Forest and Range.
- 14 McArthur, A.G., *Fire behaviour in eucalypt forests*. 1967, Forestry and Timber Bureau, Australia.
- 15 Moon, K., T. Duff, and K. Tolhurst, *Sub-canopy forest winds: understanding wind profiles for fire behaviour simulation*. Fire Safety Journal, 2019. **105**: pp. 320–329.
- 16 Harman, I.N. and J.J. Finnigan, *A simple unified theory for flow in the canopy and roughness sublayer*. Boundary-Layer Meteorology, 2007. **123**(2): pp. 339–363.
- 17 AS3959 : *Construction of Buildings in Bushfire-prone Areas*, Standards Australia, 2009; Available from: <https://www.standards.org.au/>.
- 18 Cruz, M.G., J.S. Gould, M.E. Alexander, A.L. Sullivan, W.L. McCaw, and S. Mathews, *Guide to Rate of Fire Spread Models for Australian Vegetation*. 2015: CSIRO Land and Water Flagship, Canberra, ACT and AFAC, Melbourne, VIC.
- 19 Chong, D., K. Tolhurst, and T. Duff; *Incorporating vertical winds into PHOENIX RapidFire's ember dispersal model*, Tech. Rep. Bushfire CRC, Melbourne, 2012
- 20 Ellis, P.F., *The aerodynamic and combustion characteristics of eucalypt bark: a firebrand study*. PhD Dissertation, Australian National University, 2000
- 21 Ellis, P.F., *The likelihood of ignition of dry-eucalypt forest litter by firebrands*. International Journal of Wildland Fire, 2015. **24**(2): pp. 225–235.
- 22 Manzello, S.L. and S. Suzuki, *Experimentally simulating wind driven firebrand showers in Wildland–Urban Interface (WUI) fires: overview of the NIST firebrand generator (NIST Dragon) technology*. Procedia Engineering, 2013. **62**: pp. 91–102.
- 23 Tohid, A., N. Kaye, and W. Bridges, *Statistical description of firebrand size and shape distribution from coniferous trees for use in Metropolis Monte Carlo simulations of firebrand flight distance*. Fire Safety Journal, 2015. **77**: pp. 21–35.
- 24 Sullivan, A.L., *Wildland surface fire spread modelling, 1990–2007. 3: Simulation and mathematical analogue models*. International Journal of Wildland Fire, 2009. **18**(4): pp. 387–403.
- 25 Sullivan, A.L., *Wildland surface fire spread modelling, 1990–2007. 2: Empirical and quasi-empirical models*. International Journal of Wildland Fire, 2009. **18**(4): pp. 369–386.
- 26 Sullivan, A.L., *Wildland surface fire spread modelling, 1990–2007. 1: Physical and quasi-physical models*. International Journal of Wildland Fire, 2009. **18**(4): pp. 349–368.
- 27 McGrattan, K., R. McDermott, C. Weinschenk, K. Overholt, S. Hostikka, and J. Floyd; *Fire dynamics simulator (Sixth Edition) user's guide*, in *Special publication 1019*. 2015, National Institute of Standards and Technology: Gaithersburg, Maryland, USA. p. 280
- 28 Mell, W., M.A. Jenkins, J. Gould, and P. Cheney, *A physics-based approach to modelling grassland fires*. International Journal of Wildland Fire, 2007. **16**(1): pp. 1–22.
- 29 Mell, W., A. Maranghides, R. McDermott, and S.L. Manzello, *Numerical simulation and experiments of burning douglas fir trees*. Combustion and Flame, 2009. **156**(10): pp. 2023–2041.
- 30 Mahmud, H., K.A. Moinuddin, and G.R. Thorpe, *Study of water-mist behaviour in hot air induced by a room fire: Model development, validation and verification*. Fire and Materials, 2016. **40**(2): pp. 190–205.



- 31 Sikanen, T., J. Vaari, S. Hostikka, and A. Paaianen, *Modeling and simulation of high-pressure water mist systems*. Fire Technology, 2014. **50**(3): pp. 483–504.
- 32 Wadhvani, R., D. Sutherland, A. Ooi, K. Moinuddin, and G. Thorpe, *Verification of a Lagrangian particle model for short-range firebrand transport*. Fire Safety Journal, 2017. **91**: pp. 776–783.
- 33 McGrattan, K., R. McDermott, C. Weinschenk, K. Overholt, S. Hostikka, and J. Floyd; Fire Dynamics Simulator Technical Reference Guide Volume 1: Mathematical Model, in *Special Publication 1018-1*. 2015, National Institute of Standards and Technology: Gaithersburg, Maryland, USA. p. 145.
- 34 Haider, A. and O. Levenspiel, *Drag coefficient and terminal velocity of spherical and nonspherical particles*. Powder Technology, 1989. **58**(1): pp. 63–70.
- 35 Ganser, G.H., *A rational approach to drag prediction of spherical and nonspherical particles*. Powder Technology, 1993. **77**(2): pp. 143–152.
- 36 Hölzer, A. and M. Sommerfeld, *New simple correlation formula for the drag coefficient of non-spherical particles*. Powder Technology, 2008. **184**(3): pp. 361–365.
- 37 Bagheri, G. and C. Bonadonna, *On the drag of freely falling non-spherical particles*. Powder Technology, 2016. **301**: pp. 526–544.
- 38 Manzello, S.L., J.R. Shields, T.G. Cleary, A. Maranghides, W.E. Mell, J.C. Yang, Y. Hayashi, D. Nii, and T. Kurita, *On the development and characterization of a firebrand generator*. Fire Safety Journal, 2008. **43**(4): pp. 258–268.
- 39 Westerweel, J., *Fundamentals of digital particle image velocimetry*. Measurement Science and Technology, 1997. **8**(12): p. 1379.
- 40 Manzello, S.L., A. Maranghides, and W.E. Mell, *Firebrand generation from burning vegetation I*. International Journal of Wildland Fire, 2007. **16**(4): pp. 458–462.
- 41 Moinuddin, K. and D. Sutherland, *Modelling of tree fires and fires transitioning from the forest floor to the canopy with a physics-based model*. Mathematics and Computers in Simulation, 2020. **175**: pp. 81–95.
- 42 Deardorff, J.W., *A numerical study of three-dimensional turbulent channel flow at large Reynolds numbers*. J. Fluid Mech., 1970. **41**(2): pp. 453–480.
- 43 Pope, S.B., *Turbulent flows*. 2001, IOP Publishing.
- 44 Bou-Zeid, E., M.B. Parlange, and C. Meneveau, *On the parameterization of surface roughness at regional scales*. Journal of the Atmospheric Sciences, 2007. **64**(1): pp. 216–227.
- 45 Bou-Zeid, E., J. Overney, B.D. Rogers, and M.B. Parlange, *The effects of building representation and clustering in large-eddy simulations of flows in urban canopies*. Boundary-Layer Meteorology, 2009. **132**(3): pp. 415–436.
- 46 Porté-Agel, F., C. Meneveau, and M.B. Parlange, *A scale-dependent dynamic model for large-eddy simulation: application to a neutral atmospheric boundary layer*. Journal of Fluid Mechanics, 2000. **415**: pp. 261–284.
- 47 Mueller, E., W. Mell, and A. Simeoni, *Large eddy simulation of forest canopy flow for wildland fire modeling*. Canadian Journal of Forest Research, 2014. **44**(12): pp. 1534–1544.
- 48 Amiro, B., *Drag coefficients and turbulence spectra within three boreal forest canopies*. Boundary-Layer Meteorology, 1990. **52**(3): pp. 227–246.
- 49 Cassiani, M., G. Katul, and J. Albertson, *The effects of canopy leaf area index on airflow across forest edges: large-eddy simulation and analytical results*. Boundary-Layer Meteorology, 2008. **126**(3): pp. 433–460.
- 50 Rothmel, R.C., *A mathematical model for predicting fire spread in wildland fuels*. Res. Pap. INT-115. Ogden, UT: US Department of Agriculture, Intermountain Forest and Range Experiment Station. 40 pp., 1972. **115**.
- 51 Bou-Zeid, E., C. Meneveau, and M.B. Parlange *Large-eddy simulation of neutral atmospheric boundary layer flow over heterogeneous surfaces: Blending height and effective surface roughness*. Water Resources Research, 2004. **40**. DOI: <https://doi.org/10.1029/2003WR002475>.
- 52 Dupont, S. and Y. Brunet, *Influence of foliar density profile on canopy flow: a large-eddy simulation study*. Agricultural and Forest Meteorology, 2008. **148**(6-7): pp. 976–990.
- 53 Schlegel, F., J. Stiller, A. Bienert, H.-G. Maas, R. Queck, and C. Bernhofer, *Large-eddy simulation of inhomogeneous canopy flows using high-resolution terrestrial laser scanning data*. Boundary-Layer Meteorology, 2012. **142**(2): pp. 223–243.
- 54 Shaw, R.H. and U. Schumann, *Large-eddy simulation of turbulent flow above and within a forest*. Boundary-Layer Meteorology, 1992. **61**(1-2): pp. 47–64.
- 55 Dupont, S., Y. Brunet, and J. Finnigan, *Large-eddy simulation of turbulent flow over a forested hill: Validation and coherent structure identification*. Quarterly Journal of the Royal Meteorological Society, 2008. **134**(636): pp. 1911–1929.
- 56 Dwyer, M.J., E.G. Patton, and R.H. Shaw, *Turbulent kinetic energy budgets from a large-eddy simulation of airflow above and within a forest canopy*. Boundary-Layer Meteorology, 1997. **84**(1): pp. 23–43.
- 57 Watanabe, T., *Large-eddy simulation of coherent turbulence structures associated with scalar ramps over plant canopies*. Boundary-Layer Meteorology, 2004. **112**(2): pp. 307–341.
- 58 Su, H.-B. and R.H. Shaw, *Two-point correlation analysis of neutrally stratified flow within and above a forest from large-eddy simulation*. Boundary-Layer Meteorology, 2000. **94**(3): pp. 423–460.
- 59 Wilson, J.D. and T.K. Flesch, *Wind and remnant tree sway in forest cutblocks. III. A windflow model to diagnose spatial variation*. Agricultural and Forest Meteorology, 1999. **93**(4): pp. 259–282.
- 60 Patton, E.G. and G.G. Katul, *Turbulent Pressure and Velocity Perturbations Induced by Gentle Hills Covered with Sparse and Dense Canopies*. Boundary-Layer Meteorology, 2009. **133**(2): pp. 189–217.
- 61 Finnigan, J. and S. Belcher, *Flow over a hill covered with a plant canopy*. Quarterly Journal of the Royal Meteorological Society, 2004. **130**(596): pp. 1–29.
- 62 Poggi, D. and G.G. Katul, *Turbulent intensities and velocity spectra for bare and forested gentle hills: flume*



- experiments. *Boundary-Layer Meteorology*, 2008. **129**(1): pp. 25–46.
- 63 Kanani-Sühring, F. and S. Raasch, *Spatial variability of scalar concentrations and fluxes downstream of a clearing-to-forest transition: a large-eddy simulation study*. *Boundary-Layer Meteorology*, 2015. **155**(1): pp. 1–27.
- 64 Kanani-Sühring, F. and S. Raasch, *Enhanced scalar concentrations and fluxes in the lee of forest patches: A large-eddy simulation study*. *Boundary-Layer Meteorology*, 2017. **164**(1): pp. 1–17.
- 65 Wyngaard, J.C., *Turbulence in the Atmosphere*. 2010: Cambridge University Press.
- 66 Morvan, D., S. Meradji, and W. Mell, *Interaction between head fire and backfire in grasslands*. *Fire Safety Journal*, 2013. **58**: pp. 195–203.
- 67 Peterson, E.W. and J.P. Hennessey Jr, *On the use of power laws for estimates of wind power potential*. *Journal of Applied Meteorology*, 1978. **17**(3): pp. 390–394.
- 68 Kaimal, J.C. and J.J. Finnigan, *Atmospheric boundary layer flows: their structure and measurement*. 1994: Oxford University Press.
- 69 Hunt, J.C. and D.J. Carruthers, *Rapid distortion theory and the 'problems' of turbulence*. *Journal of Fluid Mechanics*, 1990. **212**: pp. 497–532.
- 70 Miller, C., M. Gibbons, K. Beatty, and A. Boissonnade, *Topographic speed-up effects and observed roof damage on Bermuda following Hurricane Fabian (2003)*. *Weather and Forecasting*, 2013. **28**(1): pp. 159–174.
- 71 Cook, N.J., *The designer's guide to wind loading of building structures*. Vol. 2: *Static structures*. Building Research Establishment Report, London: Butterworth, | c1990, 1990.
- 72 Jackson, P. and J. Hunt, *Turbulent wind flow over a low hill*. *Quarterly Journal of the Royal Meteorological Society*, 1975. **101**(430): pp. 929–955.
- 73 Bowen, A., *The prediction of mean wind speed above simple 2D hill shapes*. *Journal of Wind Engineering and Industrial Aerodynamics*, 1983. **15**(1–3): pp. 259–270.
- 74 Teunissen, H., *Wind-tunnel and full-scale comparisons of mean wind flow over an isolated low hill*. *Journal of Wind Engineering and Industrial Aerodynamics*, 1983. **15**(1-3): pp. 271–286.
- 75 Hunt, J., S. Leibovich, and K. Richards, *Turbulent shear flows over low hills*. *Quarterly Journal of the Royal Meteorological Society*, 1988. **114**(484): pp. 1435–1470.
- 76 Hewer, F., *Non-linear numerical model predictions of flow over an isolated hill of moderate slope*. *Boundary-Layer Meteorology*, 1998. **87**(3): pp. 381–408.
- 77 Wood, N. and P. Mason, *The pressure force induced by neutral, turbulent flow over hills*. *Quarterly Journal of the Royal Meteorological Society*, 1993. **119**(514): pp. 1233–1267.
- 78 Wood, N., *The onset of separation in neutral, turbulent flow over hills*. *Boundary-Layer Meteorology*, 1995. **76**(1-2): pp. 137–164.
- 79 Kim, H.-G. and V. Patel, *Test of turbulence models for wind flow over terrain with separation and recirculation*. *Boundary-Layer Meteorology*, 2000. **94**(1): pp. 5–21.
- 80 Carpenter, P. and N. Locke, *Investigation of wind speeds over multiple two-dimensional hills*. *Journal of Wind Engineering and Industrial Aerodynamics*, 1999. **83**(1-3): pp. 109–120.
- 81 Bou-Zeid, E., C. Meneveau, and M. Parlange, *A scale-dependent Lagrangian dynamic model for large eddy simulation of complex turbulent flows*. *Physics of Fluids*, 2005. **17**(2): p. 025105.
- 82 Inoue, E., *On the Turbulent Structure of Airflow within*. *Journal of the Meteorological Society of Japan*. Ser. II, 1963. **41**(6): pp. 317–326.
- 83 Amiro, B., *Comparison of turbulence statistics within three boreal forest canopies*. *Boundary-Layer Meteorology*, 1990. **51**(1-2): pp. 99–121.
- 84 Mason, P.J. and D. Thomson, *Large-eddy simulations of the neutral-static-stability planetary boundary layer*. *Quarterly Journal of the Royal Meteorological Society*, 1987. **113**(476): pp. 413–443.
- 85 Rothermel, R.C., *A mathematical model for predicting fire spread in wildland fuels*. Res. Pap.. 115. 1972: Ogden, UT: US Department of Agriculture, Intermountain Forest & Range Experiment Station, US Forest Service.
- 86 Cheney, N., J. Gould, and W. Catchpole, *The influence of fuel, weather and fire shape variables on fire-spread in grasslands*. *International Journal of Wildland Fire*, 1993. **3**(1): pp. 31–44.
- 87 Cruz, M.G., M.E. Alexander, and A.L. Sullivan, *A response to 'Clarifying the meaning of mantras in wildland fire behaviour modelling: reply to Cruz et al. (2017)'*. *International Journal of Wildland Fire*, 2018. **27**(11): pp. 776–780.
- 88 Cheney, N., J. Gould, and W.R. Catchpole, *Prediction of fire spread in grasslands*. *International Journal of Wildland Fire*, 1998. **8**(1): pp. 1–13.
- 89 Cruz, M., A. Sullivan, S. Kidnie, R. Hurley, and S. Nichols, *The effect of grass curing and fuel structure on fire behaviour: final report*, CSIRO, 2016
- 90 Sharples, J., R. McRae, R. Weber, and A.M. Gill, *A simple index for assessing fire danger rating*. *Environmental Modelling & Software*, 2009. **24**(6): pp. 764–774.
- 91 Noble, I., A. Gill, and G. Bary, *McArthur's fire-danger meters expressed as equations*. *Australian Journal of Ecology*, 1980. **5**(2): pp. 201–203.
- 92 Sharples, J.; *Risk Implications of Dynamic Fire Propagation*. Ginnindera Falls Association, 2017.
- 93 AS3959 : *Construction of Buildings in Bushfire-prone Areas*. Standards Australia : Sydney. 3rd Edition 2009.
- 94 Sullivan, A.L., J. Sharples, S. Matthews, and M.P. Plucinski, *A downslope fire spread correction factor based on landscape-scale fire behaviour*. *Environmental Modelling & Software*, 2014. **62**: pp. 153–163.
- 95 Dold, J. and A. Zinoviev, *Fire eruption through intensity and spread rate interaction mediated by flow attachment*. *Combustion Theory and Modelling*, 2009. **13**(5): pp. 763–793.
- 96 Burrows, N.D., *Experimental development of a fire management model for Jarrah (Eucalyptus marginata Donn ex Sm.) forest*. PhD Dissertation. 1994, Australian National University, Canberra, 1994



- 97 Weise, D.R. and G.S. Biging, *A qualitative comparison of fire spread models incorporating wind and slope effects*. *Forest Science*, 1997. **43**(2): pp. 170–180.
- 98 Dupuy, J.-L., *Slope and fuel load effects on fire behavior: laboratory experiments in pine needles fuel beds*. *International Journal of Wildland Fire*, 1995. **5**(3): pp. 153–164.
- 99 Dupuy, J.-L. and J. Maréchal, *Slope effect on laboratory fire spread: contribution of radiation and convection to fuel bed preheating*. *International Journal of Wildland Fire*, 2011. **20**(2): pp. 289–307.
- 100 Readfearn, G., *How effective is bushfire hazard reduction on Australia's fires?* *The Guardian*, 2020. Available from: <https://www.theguardian.com/australia-news/2020/jan/05/explainer-how-effective-is-bushfire-hazard-reduction-on-australias-fires>.
- 101 Bohrer, G., G.G. Katul, R.L. Walko, and R. Avissar, *Exploring the effects of microscale structural heterogeneity of forest canopies using large-eddy simulations*. *Boundary-Layer Meteorology*, 2009. **132**(3): pp. 351–382.
- 102 Dupont, S., J.-M. Bonnefond, M.R. Irvine, E. Lamaud, and Y. Brunet, *Long-distance edge effects in a pine forest with a deep and sparse trunk space: in situ and numerical experiments*. *Agricultural and Forest Meteorology*, 2011. **151**(3): pp. 328–344.
- 103 Dupont, S. and E.G. Patton, *Influence of stability and seasonal canopy changes on micrometeorology within and above an orchard canopy: The CHATS experiment*. *Agricultural and Forest Meteorology*, 2012. **157**: pp. 11–29.
- 104 Sutherland, D., J. Philip, A. Ooi, and K. Moinuddin, *Simulations of surface fire propagating under a canopy: flame angle and intermittency*. in *Advances in Forest Fire Research*, presented at VIII International Conference on Forest Fire Research 2018.
- 105 Morvan, D., *Physical phenomena and Length scales governing the behaviour of wildfires: a case for physical modelling*. *Fire technology*, 2011. **47**(2): pp. 437–460.
- 106 Perez-Ramirez, Y., W.E. Mell, P.-A. Santoni, J.-B. Tramon, and F. Bosseur, *Examination of WFDS in Modeling Spreading Fires in a Furniture Calorimeter*. *Fire Technology*, 2017. **53**(5): pp. 1795–1832.
- 107 Linn, R., J. Canfield, P. Cunningham, C. Edminster, J.-L. Dupuy, and F. Pimont, *Using periodic line fires to gain a new perspective on multi-dimensional aspects of forward fire spread*. *Agricultural and Forest Meteorology*, 2012. **157**: pp. 60–76.
- 108 Morvan, D. and J. Dupuy, *Modeling the propagation of a wildfire through a Mediterranean shrub using a multiphase formulation*. *Combustion and Flame*, 2004. **138**(3): pp. 199–210.
- 109 Frangieh, N., D. Morvan, S. Meradji, G. Accary, and O. Bessonov, *Numerical simulation of grassland fires behavior using an implicit physical multiphase model*. *Fire Safety Journal*, 2018. **102**: pp. 37–47.
- 110 Morvan, D., G. Accary, S. Meradji, N. Frangieh, and O. Bessonov, *A 3D physical model to study the behavior of vegetation fires at laboratory scale*. *Fire Safety Journal*, 2018. **101**: pp. 39–52.
- 111 Apte, V., R. Bilger, A. Green, and J. Quintiere, *Wind-aided turbulent flame spread and burning over large-scale horizontal PMMA surfaces*. *Combustion and Flame*, 1991. **85**(1–2): pp. 169–184.
- 112 Dupuy, J.-L. and D. Morvan, *Numerical study of a crown fire spreading toward a fuel break using a multiphase physical model*. *International Journal of Wildland Fire*, 2005. **14**(2): pp. 141–151.
- 113 Cruz, M.G., W.L. McCaw, W.R. Anderson, and J.S. Gould, *Fire behaviour modelling in semi-arid mallee-heath shrublands of southern Australia*. *Environmental Modelling & Software*, 2013. **40**: pp. 21–34.
- 114 Tolhurst, K., B. Shields, and D. Chong, *Phoenix: development and application of a bushfire risk management tool*. *The Australian Journal of Emergency Management*, 2008. **23**(4): p. 47.
- 115 Sutherland, D., J. Philip, A. Ooi, and K. Moinuddin, *Large Eddy Simulation of Flow Over Streamwise Heterogeneous Canopies: Quadrant Analysis*. *Proceedings of the 21st Australasian Fluid Mechanics Conference, AFMC 2018, Australian Fluid Mechanics Society*, 2018.
- 116 Rashid, M., J. Hilton, N. Khan, D. Sutherland, and K. Moinuddin, *A report on WRF software development (preliminary)*. 2020, Bushfire and Natural Hazard CRC, Melbourne, Australia.
- 117 Radeloff, V.C., D.P. Helmers, H.A. Kramer, M.H. Mockrin, P.M. Alexandre, A. Bar-Massada, V. Butsic, T.J. Hawbaker, S. Martinuzzi, and A.D. Syphard, *Rapid growth of the US wildland-urban interface raises wildfire risk*. *Proceedings of the National Academy of Sciences*, 2018. **115**(13): pp. 3314–3319.
- 118 Bryner, N., *Building Codes and Standards for New Construction*, in *Encyclopedia of Wildfires and Wildland-Urban Interface Fires*, S.L. Manzello, Editor. 2019, Springer: Cham. p. 978.
- 119 AS 3959-2018: *Construction of Buildings in Bushfire-Prone Areas*. 2018: Sydney, Australia
- 120 National Fire Protection Association, *NFPA 1144 Standard for reducing structure ignition hazards from wildland fire*. 2013.
- 121 Roberts, M., J. Sharples, and A. Rawlinson, *Incorporating ember attack in bushfire risk assessment: a case study of the Ginnindery region*. In *MODSIM2017 Proceedings – MSSANZ, Modelling and Simulation Society of Australia and New Zealand*. The 22nd International Congress on Modelling and Simulation (Hobart, TAS). 2017.
- 122 Manzello, S.L., A. Maranghides, J.R. Shields, W.E. Mell, Y. Hayashi, and D. Nii, *Mass and size distribution of firebrands generated from burning Korean pine (Pinus koraiensis) trees*. *Fire and Materials: An International Journal*, 2009. **33**(1): pp. 21–31.
- 123 Ellis, P., *The effect of the aerodynamic behaviour of flakes of jarrah and karri bark on their potential as firebrands*. *Journal of the Royal Society of Western Australia*, 2010. **93**: p. 21.
- 124 McGrattan, K., R. McDermott, S. Hostikka, J. Floyd, and M. Vanella. *Fire Dynamics Simulator Technical Reference Guide. Vol. 1: Mathematical Model*, Tech. Rep. 2019. NIST Special Publication 1018-1 US Department of Commerce.
- 125 Thunderhead Engineering, *Pyrosim User Manual*, 2014. Available from: <https://support.thunderheadeng.com/docs/pyrosim/2020-2/user-manual/>.
- 126 Raupach, M.R., *Drag and drag partition on rough surfaces*. *Boundary-Layer Meteorology*, 1992. **60**(4): pp. 375–395.



- 127 Landscape Data Visualiser, Water and Landscape Dynamics Group, ANU, Canberra, 2016; Available from: <https://maps.tern.org.au/#/>.
- 128 Simard, M., N. Pinto, J.B. Fisher, and A. Baccini, *Mapping forest canopy height globally with spaceborne lidar*. *Journal of Geophysical Research: Biogeosciences*, 2011. **116**(G4).
- 129 Marsden-Smedley, J., *Tasmanian Wildfires January–February 2013: Forcett–Dunalley, Repulse, Bicheno, Giblin River, Montumana, Molesworth and Gretna*. Report prepared for the Tasmania Fire Service. Bushfire Cooperative Research Centre, Melbourne, 2014.
- 130 Burrows, N.D., *Mt Cooke Wildfire January 2003: Monitoring impacts and recovery*. DBCA Library, Government of Western Australia, 2005.
- 131 Cheney, N., *Fire behaviour during the Pickering Brook wildfire, January 2005 (Perth Hills Fires 71–80)*. *Conservation Science Western Australia*, 2010. **7**(3): pp. 451–468.
- 132 Massman, W.J., J. Forthofer, and M.A. Finney, *An improved canopy wind model for predicting wind adjustment factors and wildland fire behavior*. *Canadian Journal of Forest Research*, 2017. **47**(5): pp. 594–603.
- 133 Khan, N., D. Sutherland, R. Wadhvani, and K. Moinuddin, *Physics-based simulation of heat load on structures for improving construction standards for bushfire prone areas*. *Frontiers in Mechanical Engineering*, 2019. **5**: p. 35.
- 134 Gould, J.S., W. McCaw, N. Cheney, P. Ellis, I. Knight, and A. Sullivan, *Project Vesta: fire in dry eucalypt forest: fuel structure, fuel dynamics and fire behaviour*. 2008: CSIRO Publishing.
- 135 Jarrin, N., S. Benhamadouche, D. Laurence, and R. Prosser, *A synthetic-eddy-method for generating inflow conditions for large-eddy simulations*. *International Journal of Heat and Fluid Flow*, 2006. **27**(4): pp. 585–593.
- 136 Wickramasinghe, A., N. Khan, and K. Moinuddin, *Physics-based simulation of firebrand and heat flux on structures in the context of AS3959*, Bushfire and Natural Hazard CRC, 2020; Available from: <https://www.bnhcrc.com.au/resources/poster/7709>.
- 137 Dowdy, A.J., G.A. Mills, K. Finkele, and W. de Groot, *Australian fire weather as represented by the McArthur Forest Fire Danger Index and the Canadian Forest Fire Weather Index*. Centre for Australian Weather and Climate Research, Melbourne, Australia, Tech. Rep, 2009.
- 138 Manzello, S.L., S. Suzuki, and Y. Hayashi, *Enabling the study of structure vulnerabilities to ignition from wind driven firebrand showers: A summary of experimental results*. *Fire Safety Journal*, 2012. **54**: pp. 181–196.
- 139 Manzello, S.L., T.G. Cleary, J.R. Shields, and J.C. Yang, *Ignition of mulch and grasses by firebrands in wildland–urban interface fires*. *International Journal of Wildland Fire*, 2006. **15**(3): pp. 427–431.
- 140 Manzello, S.L., J.R. Shields, J.C. Yang, Y. Hayashi, and D. Nii, *On the use of a firebrand generator to investigate the ignition of structures in wildland–urban interface (WUI) fires*. in *11th international conference on fire science and engineering (INTERFLAM)*. 2007.
- 141 Sutherland, D., K. Moinuddin, and A. Ooi, *Large-eddy simulation of neutral atmospheric surface layer flow over heterogeneous tree canopies*. in *Research Forum 2017: proceedings from the Research Forum at the Bushfire and Natural Hazards CRC and AFAC Conference, Sydney, Australia, 4–6 September 2017*. 2017. Bushfire and Natural Hazards CRC.